DESIGN OPTIMIZATION OF A METAL-ASSISTED BIOCHEMICAL SENSOR BASED ON NANO-SLOTS IN SILICON-ON-INSULATOR WAVEGUIDE
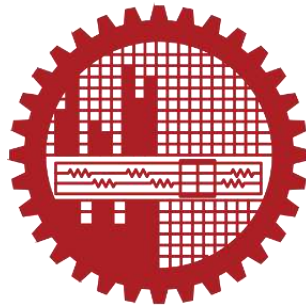
Mahdi Zulfikar

(Student no: 0416062252 F)

MASTER OF SCIENCE IN ELECTRICAL AND ELECTRONIC ENGINEERING

Department of Electrical and Electronic Engineering

Bangladesh University of Engineering and Technology

Dhaka, Bangladesh

March 2023

The thesis titled "DESIGN OPTIMIZATION OF A METAL-ASSISTED BIOCHEMICAL SENSOR BASED ON NANO-SLOTS IN SILICON-ON-INSULATOR WAVEGUIDE" submitted by Mahdi Zulfikar, Student no: 0416062252 F, Session: April 2016, has been accepted as satisfactorily in partial fulfilment of the requirements for the degree of MASTER OF SCIENCE IN ELECTRICAL AND ELECTRONIC ENGINEERING on 28 March 2023.

BOARD OF EXAMINERS

1. _____

   Dr. Md. Shah Alam   Chairman
   Professor   (Supervisor)
   Department of Electrical and Electronic Engineering
   Bangladesh University of Engineering and Technology
   Dhaka

2. _____

   Dr. Md. Aynal Haque   Member
   Professor and Head   (Ex-Officio)
   Department of Electrical and Electronic Engineering
   Bangladesh University of Engineering and Technology
   Dhaka

3. _____

   Dr. Mohammad Jahangir Alam   Member
   Professor
   Department of Electrical and Electronic Engineering
   Bangladesh University of Engineering and Technology
   Dhaka

4. _____

   Dr. A. K. M. Akther Hossain   Member
   Professor   (External)
   Department of Physics
   Bangladesh University of Engineering and Technology
   Dhaka

Declaration

This is hereby declared that the work titled "DESIGN OPTIMIZATION OF A METAL-ASSISTED BIOCHEMICAL SENSOR BASED ON NANO-SLOTS IN SILICON-ON-INSULATOR WAVEGUIDE" is the outcome of research carried out by me under the supervision of Dr. Md. Shah Alam, in the Department of Electrical and Electronic Engineering, Bangladesh University of Engineering and Technology, Dhaka 1000. It is also declared that this thesis or any part of it has not been submitted elsewhere for the award of any degree or diploma.

Mahdi Zulfikar (0416062252 F) _____

Date_____

Acknowledgment

I am deeply grateful to have had the opportunity to conduct this postgraduate thesis in the Department of Electrical and Electronic Engineering at the Bangladesh University of Engineering and Technology.

First and foremost, I express my sincere gratitude to Almighty for providing me with the knowledge and strength to complete this work.

I would like to extend my heartfelt appreciation to my supervisor, Dr. Md. Shah Alam and the head of the EEE department, for their invaluable guidance, insightful discussions, and unwavering support throughout the entire duration of this research. Dr. Alam's door was always open to me, and his expertise in modeling was instrumental in helping me overcome challenges and refine my simulations. I also thank him for his assistance in the writing, formatting, and editing of this thesis.

Last but not least, I owe a debt of gratitude to my parents, whose unwavering support and encouragement throughout my academic journey and research process have been indispensable. Without their love, motivation, and support, this accomplishment would not have been possible.

I also thank all of my colleagues and friends who have supported me during this journey.

Mahdi Zulfikar

Roll: 0416062252 F

Abstract

This research aimed to investigate the potential of slot waveguide technology for use in biochemical detection. The technology allows for the confinement of light in sub-wavelength scales and low refractive index regions, resulting in increased interaction with target molecules. The study focused on a cross-slot waveguide made of silicon and assisted by metallic silver, which achieved a polarization-independent confinement factor of 60% with an optimized dimension of $340\ nm$ of Ag width, $153\ nm$ of Si width, $257\ nm$ height, offering greater sensitivity for detecting specific target molecules in complex biological samples. In addition, the study explored a slot waveguide with silver nanoparticles that generated a strong enhancement factor of 2.87×10^{11}, an average electric field of $350\ V/m$, $32\ nm$ radius of the nanoparticles, $175\ nm$ and $150\ nm$ of Silicon height and width respectively, a separation distance of $2\ nm$ and $2000\ nm$ of wavelength, making it a promising design for analyzing samples in their natural and unaltered states.

The findings have significant implications for the design of biochemical sensors, as the use of slot waveguide technology can help overcome the limitations of traditional biosensors, such as low sensitivity and poor selectivity. The confinement of light in sub-wavelength scales and low refractive index regions results in improved sensitivity and excellent selectivity, enabling the detection of specific target molecules in complex biological samples. These results could lead to the development of new and improved biochemical sensors that could revolutionize disease diagnosis and environmental monitoring.

Table of Contents

List of Figures

Chapter 1

INTRODUCTION

1.1. Background

The journey begins with the guiding of light by refraction, the principle that makes fiber optics possible. It was first demonstrated by Daniel Colladon and Jacques Babinet in Paris in the early 1840s. John Tyndall included a demonstration of it in his public lectures in London, 12 years later [1]. In the 1930s, it was shown that one could transmit images through a bundle of unclad optical fibers. That same year, Harold Hopkins and Narinder Singh Kapany at Imperial College in London succeeded in making image-transmitting bundles with over 10,000 fibers and subsequently achieved image transmission through a 75 cm-long bundle that combined several thousand fibers [2]. Their article titled "A flexible fiberscope, using static scanning" was published in the journal Nature in 1954 [3]. In 1970, the goal of making single-mode fibers with an attenuation of less than 20dB/km was reached by scientists at Corning Glass Works. This was achieved through doping silica glass with titanium [2]. Optical fibers typically include a core surrounded by a transparent cladding material with a lower index of refraction. Light is kept in the core by the phenomenon of total internal reflection which causes the fiber to act as a waveguide.

The success of optical transmission was taken to a ne*w* eight by an accident in 2003. The slot-waveguide was born as an unexpected outcome of theoretical studies on metal-oxide-semiconductor (MOS) electro-optic modulation in high-confinement silicon photonic waveguides by Vilson Rosa de Almeida and Carlos Angulo Barrios at Cornell University. Theoretical analysis [4] and experimental demonstration [5], [6] of the first slot-waveguide implemented in the Si/SiO_2 material system at 1.55 μm operation wavelength were reported by Cornell researchers in 2004. The main noticing factor was the power density of the slot waveguide. In 2005, researchers at the Massachusetts Institute of Technology proposed to use multiple slot regions in the same guided-wave structure (multi-slot waveguide) to increase the optical field in the low-refractive-index regions [7]. The experimental demonstration of such multiple-slot waveguides in a horizontal configuration was first published in 2007 [8]. The power density in the slot is much higher than that in the high-index regions. Since wave

propagation is due to total internal reflection, there is no interference effect involved and the slot-structure exhibits very low wavelength sensitivity.

1.2. Literature Review

The enigma of light has fascinated humanity since the dawn of the universe. The mysterious wavelengths emitted by countless stars travel vast distances to illuminate our strikingly beautiful nights. In 300 BC, Euclid delved into the study of light, postulating that it traveled in straight lines and outlining the laws of reflection. He even pondered the mechanism of sight, questioning how one could see stars immediately upon opening their eyes at night without a beam of light emanating from the eye [2]. But the questions of the human inquisitive mind did not stop there. To explain the nature of light Sir Isaac Newton proposed the corpuscular theory of light. But this theory was not sufficient to explain the origin of beautiful colors. To unravel the puzzle, light was thought of as a combination of waves, similar to sound. The beauty of nature lies even deeper. James Clerk Maxwell discovered that self-propagating electromagnetic waves would travel through space at a constant speed, which happened to be equal to the previously measured speed of light leading to the realization that light was directly related to electricity and magnetism. Eventually, the modern theory of quantum mechanics came to picture light as (in some sense) both a particle and a wave, and (in another sense), as a phenomenon that is neither a particle nor a wave (which are macroscopic phenomena, such as baseballs or ocean waves). Instead, modern physics sees light as something that can be described sometimes with mathematics appropriate to one type of macroscopic metaphor (particles), and sometimes another macroscopic metaphor (water waves), but is something that cannot be fully imagined.

The electromagnetic theory of light is quite enough to explain many properties of light. One such property is total internal reflection. Total internal reflection is the phenomenon that occurs when a propagated wave strikes a medium boundary at an angle larger than a critical angle with respect to the normal to the surface. If the refractive index is lower on the other side of the boundary and the incident angle is greater than the critical angle, the wave cannot pass through and is entirely reflected. Using this property optical fiber was made. Another quite opposite interesting property is the discontinuity of the electric field (E-field) at high-refractive-index-contrast interfaces. The resulting E-field normal to the high-index-contrast

interfaces is enhanced and remains high across it. The power density in the low-index region is much higher than that in the high-index regions.

Since 2004, many researchers have exploited the last feature [3]–[18]. They have made various types of slot waveguides and ring resonators based on this property and stated various uses in practical scientific fields.

In this thesis, another property as well as the last property has been proposed. A metal barrier does not allow the electromagnetic waves to pass energy beyond the metal surface. Thus, it increases the power density even more in the low index region which allows better sensitivity and optimization. This thesis combines a cross-slot waveguide made of silicon and a barrier of metal silver around the core slots.

1.3.   Objective

The major objectives of this study are as follows*:*

- To design a multiple cross slot waveguide having metal (Ag) barrier for biochemical sensing application.
- To optimize optical confinement factor so that the design becomes polarization independent.
- To optimize the sensitivity of the biochemical sensor at dual polarization.

1.4.   Scope of the study

In this project, our focus is on the design and optimization of two multiple cross-slot waveguides for biochemical detection purposes. The first waveguide is composed of Silicon, with the assistance of a metal strip made of silver and is placed on a Silicon-di-Oxide (SiO_2) base. The entire structure will be submerged in a gaseous or liquid medium for detecting biochemical substances. The simulation and design of the system will be carried out using COMSOL Multiphysics, whereby varying dimensions and optical properties of the structure will be adjusted until the optimized solution is obtained, which is polarization independent for both TE and TM. The second waveguide will be an immersion waveguide made of silver nanoparticles and will be optimized for detecting biochemical substances as well. Finally, a

comparison will be made between the results obtained from both waveguides and contemporary research on slot waveguides to determine the efficacy of the design.

1.5.   Organization of the Thesis

The thesis consists of six chapters that are organized as follows:

Chapter 1 presents the study's background, providing a brief overview of the essential parameters and discussing past research related to the topic. It also outlines the study's objective, scope, and significance.

Chapter 2 details the methodology employed in the study, including a description of each step and the relevant theories.

Chapter 3 covers conventional waveguide structures and their simulation results.

Chapter 4 presents the proposed design of the study, analyzing the results and comparing them with established findings.

Chapter 5 explores the theory of Raman scattering in conjunction with simulation results for a waveguide with silver nanoparticles.

Finally, Chapter 6 summarizes the study's primary conclusions and offers suggestions for further research.

The list of references contains all sources cited throughout the thesis.

Chapter 2

THEORY AND METHODOLOGY

For most of the optical waveguides, light is confined in the core due to the higher index there. Therefore, light interaction with the sensing material in the cladding region is limited, leading to the low sensitivity of these devices. However, the unique feature of a slot waveguide, where light is guided in a low-index region, allows easy access of the sensing layer to the high-field region. Thus, the enhancement of light interaction in the sensing region can improve the sensitivity of the sensor. The guidance property in a slot waveguide is due to the continuity of the normal component of the electric flux density, which increases the normal component of the electric field, in the low index region. There are two possible types of slot waveguides, relating to their structural orientation, called vertical and horizontal slot waveguides. In a vertical slot, E_x the field is enhanced, which is the dominant component for the quasi-TE mode and normal to the vertical interfaces. Similarly, for a horizontal slot, the dominant E_y component of the quasi-TM mode increases inside the slot. It is possible to combine both horizontal and vertical slots. In a cross-slot waveguide both E_x and E_y fields are enhanced. In this study a cross-slot waveguide with a metal Ag barrier which increases both E_x and E_y fields due to the reflective nature of the metal surface are presented.

2.1. Slot Waveguide Structure

A slot waveguide is an optical waveguide that guides strongly confined light in a subwavelength scale low refractive index region by total internal reflection. A slot waveguide consists of two strips or slabs of high refractive index n_H materials separated by a subwavelength scale low refractive index n_S slot region and surrounded by low refractive index n_C cladding materials. Planar slot waveguides have been fabricated in different material systems such as Si/SiO_2 [9], [15]–[18] and Si_3N_4/SiO_2 [11], [13], [14], [19], [20]. Both vertical (slot plane is normal to the substrate plane) and horizontal (slot plane is parallel to the substrate plane) configurations have been implemented by using conventional micro and Nano-fabrication techniques. These processing tools include electron beam lithography, photolithography, chemical vapor deposition [usually low-pressure chemical vapor deposition

(LPCVD) or plasma enhanced chemical vapor deposition (PECVD)], thermal oxidation, reactive ion etching and focused ion beam. In vertical slot waveguides, the slot and strips widths are defined by electron or photo lithography and dry etching techniques whereas in horizontal slot-waveguides the slot and strips thicknesses are defined by a thin film deposition technique or thermal oxidation. Thin film deposition or oxidation provides better control of the layer's dimensions and smoother interfaces between the high index contrast materials than lithography and dry etching techniques. This makes horizontal slot waveguides less sensitive to scattering optical losses due to interface roughness than vertical configurations. Fabrication of a non-planar (fiber-based) slot-waveguide configuration has also been demonstrated by means of conventional micro-structured optical fiber technology [12].
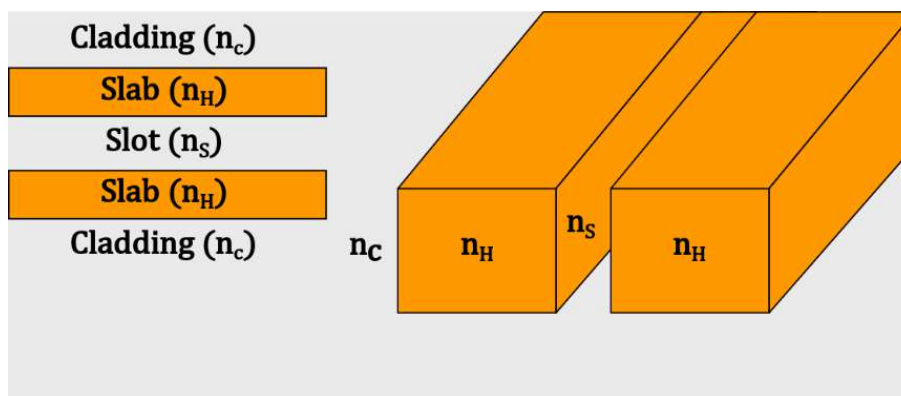
Figure 2.1: Schematic 2D & 3D slot-waveguide. Light propagates in the z-direction.

2.2.   Physics Behind the Slot Waveguide

A slot waveguide consists of two strips or slabs of high refractive index n_H materials separated by a subwavelength scale low refractive index n_S slot region and surrounded by low refractive index n_C cladding materials. The principle of operation of a slot-waveguide is based on the discontinuity of the electric field (E field) at high refractive index contrast interfaces. Maxwell's equations state that, to satisfy the continuity of the normal component of the electric displacement field D at an interface, the corresponding E field must undergo a discontinuity with higher amplitude in the low-refractive-index side. That is, at an interface between two regions of dielectric constants ε_S and ε_H, respectively:

$$D_S^N = D_H^N$$
$$\varepsilon_S E_S^N = \varepsilon_H E_H^N$$
$$n_S^2 E_S^N = n_H^2 E_H^N \tag{2.1}$$

Where the superscript N indicates the normal components of D and E vector fields. Thus, if $n_S \ll n_H$, then $E_S^N \gg E_H^N$.
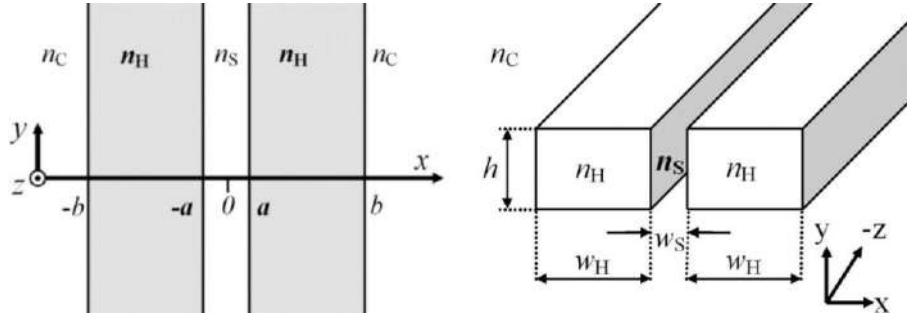
Figure 2.2: Schematic of slot-waveguide

The following equation describes the index profile of a symmetric slot waveguide:

$$n(x) = \begin{cases} n_S & |x| \leq a \\ n_H & a \leq |x| \leq b \\ n_C & |x| \geq b \end{cases} \tag{2.2}$$

where $2a$ is the thickness of the guiding layer (core), n_S is the index of refraction of the core, $(b - a)$ is the thickness and n_H is the index of refraction of the bounding media and n_C is the refractive index of the cladding material. To support waveguide modes in core, n_H must be greater than n_S, i.e., $n_H \gg n_S$. The problem at hand is finding these guided modes.

The electromagnetic treatment of such a problem is relatively easy because the medium is homogeneous in each segment of the dielectric structure. In addition, the solutions of Maxwell's equations in homogeneous media are simply plane waves. Thus, all we need to do is write the plane wave solutions for each segment and then match the boundary conditions at the interfaces to ensure the continuity of the wavefunction. We now consider the propagation of monochromatic radiation along the z axis. Maxwell's equation can be written in the phasor form considering time factor as $e^{j\omega t}$:

$$\nabla \times E = -j\omega\mu H \tag{2.3}$$

$$\nabla \times H = j\omega\epsilon E \tag{2.4}$$

Since the whole structure is homogeneous along the z axis, solutions to the wave equations can be taken as*:*

$$\begin{aligned} E &= E(x,y)exp[j(\omega t - \beta z)] \\ H &= H(x,y)exp[j(\omega t - \beta z)] \end{aligned} \tag{2.5}$$

Here β is the z component of the wavevectors and is known as the propagation constant to be determined from Maxwell's equations, $E(x, y)$ and $H(x, y)$ are wavefunctions of the guided modes. For a dielectric structure that consists of homogeneous and isotropic materials, the wave equation can be obtained by eliminating H:

$$\left(\frac{\partial^2}{\partial x^2} + \frac{\partial^2}{\partial y^2}\right) E(x, y) + [k_0^2 n^2 - \beta^2] E(x, y) = 0 \tag{2.6}$$

Here $k_0 = \frac{\omega}{c}$ is the wavenumber in vacuum. We will solve this equation separately in each segment of the structure and then match the tangential components of the field vectors at each interface. In addition to the continuity conditions at the interfaces, another important boundary condition for guided modes is that the field amplitudes be zero at infinity. Rigorously, the analytical solution for the transverse E field profile E_x of the fundamental TM eigenmode of the slab-based slot waveguide is:

$$E_x(x) = A \begin{cases} \dfrac{1}{n_S^2} \cosh(\gamma_S x) & |x| \leq a \\[2ex] \dfrac{1}{n_H^2} \cos(\gamma_S a) \cos(\kappa_H |x| - a) + \dfrac{\gamma_S}{n_S^2 \kappa_H} \sin(\kappa|x| - a) & a \leq |x| \leq b \\[2ex] \dfrac{1}{n_C^2} \left\{ \begin{aligned} &\cosh(\gamma_S a) \cos(\kappa_H b - a) \\ &+ \dfrac{n_H^2 \gamma_S}{n_S^2 \kappa_H} \sinh(\gamma_S a) \sin(\kappa_H b - a) \end{aligned} \right\} \exp(-\gamma_C |x| - b) & |x| \geq b \end{cases} \tag{2.7}$$

where κ_H is the transverse wave number in the high-index slabs, γ_C is the field decay coefficient in the cladding, γ_S is the field decay coefficient in the slot, and constant A is given by:

$$A = A_0 \frac{\sqrt{k_0^2 n_H^2 - \kappa_H^2}}{k_0} \tag{2.8}$$

Here A_0 is an arbitrary constant and $k_0 = \frac{2\pi}{\lambda_0}$ is the vacuum wave number. The transverse parameters κ_H, γ_C and γ_S simultaneously obey the relations $k_0^2 n_H^2 - \kappa_H^2 = k_0^2 n_C^2 + \gamma_C^2 = k_0^2 n_S^2 + \gamma_S^2 = \beta^2$, where β is the eigenmode propagation constant, which can be calculated by solving the transcendental characteristic equation:

$$\tan\{\kappa_H(b - a) - \Phi\} = \frac{n_H^2 \gamma_S}{n_S^2 \kappa_H} \tanh(\gamma_S a) \tag{2.9}$$

Here $\Phi = \tan^{-1} \frac{n_H^2 \gamma_C}{n_C^2 \kappa_H}$. The E field immediately inside the slot ($|x| = a^-$) is $\frac{n_H^2}{n_S^2}$ times higher than that immediately inside the high-index slabs ($|x| = a^+$). The ratio $\frac{n_H^2}{n_S^2}$ equals 6 for a $Si -$

SiO_2 interface and 12 for a $Si-air$ interface. When the width of the slot is much smaller than the characteristic decay length inside the slot ($a \ll \frac{1}{\gamma_S}$), the field remains high across the slot.
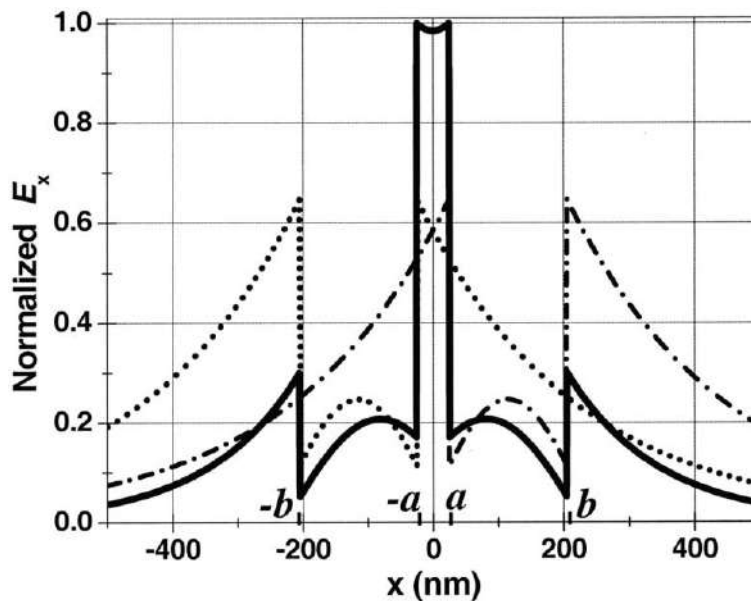
Figure 2.3: Normalized transverse E field (E_x) distribution of the fundamental TM eigenmode [4]

The electric field and magnetic field of confined modes are finite in the cladding regions. Although the power associated with the mode is propagating along the z direction, part of the electromagnetic field energy is propagating outside the guiding layer. Let Γ_S be the fraction of power flow through slot of the slot waveguide.

From definition, we have*:*

$$\Gamma_S = \frac{\iint_S Re(\boldsymbol{E} \times \boldsymbol{H}^*).\hat{\boldsymbol{z}}\,dxdy}{\iint_\infty Re(\boldsymbol{E} \times \boldsymbol{H}^*).\hat{\boldsymbol{z}}\,dxdy} \qquad (2.10)$$

Here E is the electric field, H is the magnetic field, $*$ denotes a complex conjugate, Re returns the real part of a complex number and $\iint_\Omega Re(\boldsymbol{E} \times \boldsymbol{H}^*).\hat{\boldsymbol{z}}\,dxdy$ is the power flow through a given area Ω.

Optical biochemical sensing [21]–[25]such as DNA sequencing by hybridization, antigen-antibody reactions study [26] or pollution concentration measurement in water are mainly based on immobilization of an ultra-thin layer of receptor molecules on the waveguide surface. Effective index, n_{eff} of the guided mode in a waveguide is affected by the change of molecular layer (which can be called sensing layer) thickness caused by the interaction between analyte and receptor molecules. The waveguide sensitivity, S, can be defined as*:*

$$S = \frac{\partial n_{eff}}{\partial \tau} \tag{2.11}$$

Here τ is the thickness of the sensing layer.
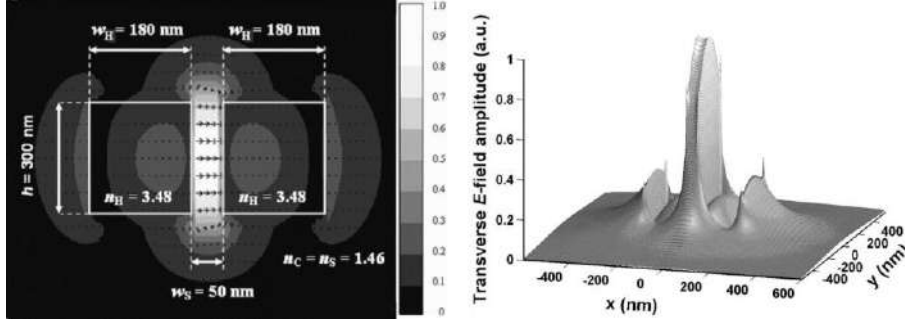
Figure 2.4: Contour 3D surface plot of the E-field amplitude. [4]

The change in n_{eff} , Δn_{eff} , produced by the change of the sensing layer thickness, $\Delta \tau$, can be related approximately by the light confined in sensing layer and there is a positive correlation between the Δn_{eff} and confinement factor in the sensing layer for the guided modes in a slot waveguide.

However, at the sharp boundary of Si there will be an electric field deformity. The deformity must be taken into account in a different manner. We will calculate the field strength at the vertex of a sharp edge [27].
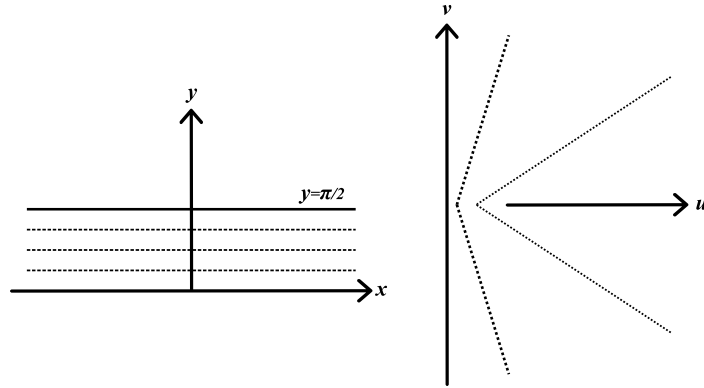
Figure 2.6: xy to uv plane transformation.

In Fig. 2.6, if $z = x + iy$ and $w = u + iv$, the transformation $w = k \cosh z$, where k is a constant, will transform a series of lines parallel to the x-axis, and in the z-plane, to a series of confocal hyperbolae in the w-plane. The line $y = \frac{1}{2}\pi$ in the z-plane is transformed into the line $u = 0$ in the w-plane; the line $y = 0$ is transformed to $v = 0$, but u only has values greater than a certain minimum. A physical picture of the transformation is to regard it as transforming

an infinite parallel-plate condenser, with plates at $y = 0$ and $y = \frac{1}{2}\pi$, into two perpendicular plates, separated by a gap, in the w-plane.

From eqn. (2.7)

$$u + iv = k \cosh x \cosh iy + k \sinh x \sinh iy \qquad (2.12)$$

But $\cosh iy = \cos y$ and $\sinh iy = i \sin y$, hence by separating real and imaginary parts.

$$u = k \cosh x \cos y$$

$$v = k \sinh x \sin y \qquad (2.13)$$

When the curves intersect the u-axis, $v = 0$ and since in general $y \neq 0$ this implies $k \sinh x = 0$

hence $x = 0$. Thus eqn. (2.13) gives:

$$u = k \cos y \qquad (2.14)$$

At the intersection of the hyperbola with the u-axis. Hence the distance l from the fixed plate to this point of intersection is:

$$l = k \, cosy \qquad (2.15)$$

To determine the equation of the hyperbolae in the w-plane we must eliminate x from the above equations. Putting

$$^u/_k \cos y = \cosh x$$

$$^v/_k \sin y = \sinh x \qquad (2.16)$$

and squaring and subtracting we obtain

$$\frac{u^2}{k^2} \cos^2 y - \frac{v^2}{k^2} \sin^2 y = 1 \qquad (2.17)$$

Thus, the lines $y = constant$ transform into hyperbole (of which only the positive branches are considered in this discussion). The hyperbolae have eccentricities, e, of $\sec y$ and asymptotes given by

$$v = \pm u \tan y \qquad (2.18)$$

The radius of curvature r at any point on the hyperbolae is given by:

$$r = \frac{\left[1 + \left(\frac{du}{dv}\right)^2\right]^{\frac{3}{2}}}{\frac{d^2u}{dv^2}} \tag{2.19}$$

Differentiation of eqn. (2.18) gives:

$$\frac{du}{dv} = \frac{v}{u}\cot^2 y$$

$$\frac{d^2u}{dv^2} = \frac{u^2\cot^2 y - v^2\cot^4 y}{u^3} \tag{2.20}$$

Clearly $\frac{du}{dv}$ is zero at the vertex where $v = 0$, thus eqn. (2.19) reduces to,

$$r_v = \left(\frac{d^2u}{dv^2}\right)^{-1}_{v=0}$$

where r_v is the value of r at the vertex. Thus,

$$r_v = u\tan^2 y$$

$$r_v = l\tan^2 y \tag{2.21}$$

In general, the field at the vertex of the hyperbola will have two components, in the u and v directions, $\frac{\partial V}{\partial u}$ and $\frac{\partial V}{\partial v}$, where V is the potential difference between the edge and the flat plate and corresponds to the potential difference between the two plates of the parallel-plate condenser. It can be written as:

$$\frac{\partial V}{\partial u} = \frac{\partial V}{\partial x}\frac{\partial x}{\partial u} + \frac{\partial V}{\partial y}\frac{\partial y}{\partial u}$$

$$\frac{\partial V}{\partial v} = \frac{\partial V}{\partial x}\frac{\partial x}{\partial v} + \frac{\partial V}{\partial y}\frac{\partial y}{\partial v} \tag{2.22}$$

However, $\frac{\partial V}{\partial x} = 0$ for the parallel-plate condenser, so

$$\left(\frac{\partial V}{\partial u}\right)_v = \left(\frac{dV}{dy}\right)\left(\frac{\partial y}{\partial u}\right)_v$$

$$\left(\frac{\partial V}{\partial v}\right)_u = \left(\frac{dV}{dy}\right)\left(\frac{\partial y}{\partial v}\right)_u \tag{2.23}$$

Differentiating eqn. (2.18) with respect to u and v in turn gives:

$$\left(\frac{\partial V}{\partial u}\right)_v = -\frac{u \cos y \sin^3 y}{u^2 \sin^4 y + v^2 \cos^4 y}$$

$$\left(\frac{\partial V}{\partial v}\right)_u = \frac{v \sin y \cos^3 y}{u^2 \sin^4 y + v^2 \cos^4 y} \tag{2.24}$$

Since $v = 0$ and $u = k \cos y$ at the vertex

$$\left(\frac{dy}{du}\right)_{v=0} = -\frac{1}{k \sin y}$$

$$\left(\frac{dy}{dv}\right)_{v=0} = 0 \tag{2.25}$$

Now in eqn. (2.22), $\frac{dV}{dy}$ is the uniform field in the parallel-plate condenser. The negative sign of eqns. (2.25) shows that the field in the edge and plate arrangement is in the opposite sense to that in the condenser. Evidently from Fig. 2.6, if the potential increases for decrease of y from $\frac{1}{2}\pi$ to zero, then the potential in the w-plane increases as u increases from zero to l. Let E_c be the uniform field in the parallel-plate condenser, and E_v be the field at the vertex of the edge, and the following is obtained.

$$E_v = -\frac{E_c}{l \tan y} = -\frac{E_c}{(r_v l)^{\frac{1}{2}}} \tag{2.26}$$

Thus,

$$E \propto r_v^{-\frac{1}{2}} \tag{2.27}$$

So, the overall electric field is inversely proportional to the square root of the edge curvature.

The complex relative permittivity of the highly doped p-silicon at telecom wavelengths can be modeled using the Lorentz-Drude model [28],

$$\epsilon(\omega) = \epsilon_\infty - \frac{\omega_P^2}{\omega^2\left(1 + \frac{j}{\omega\tau}\right)} = \epsilon_\infty - \frac{\omega_P^2 \tau^2}{1 + \omega^2\tau^2} + \frac{j\omega_P^2\tau}{\omega(1 + \omega^2\tau^2)} \tag{2.28}$$

where, ω_P is the plasma frequency, ε_∞ is the infinite frequency relative permittivity, τ is the electron/hole relaxation time, $\omega = \frac{2\pi c}{\lambda}$ is the angular frequency, c is the speed of light in

vacuum and j is the imaginary unit. In the case of the highly doped degenerate intrinsic semiconductors, $\omega_P^2 = \frac{Ne^2}{\epsilon_0 m_{eff}}$ and $\tau = \frac{\mu m_{eff}}{e}$; where, N is the free carrier concentration, μ is the electron/hole's drift mobility and m_{eff} is the averaged electron/hole effective mass. Usually, the angular frequency $\omega \gg \omega_P$ and $\omega\tau \gg 1$. Thus, equation 2.28 can be expressed as following,

$$\epsilon(\omega) = \epsilon_\infty - \frac{\sigma}{\omega^2 \epsilon_0 \tau} + \frac{j\sigma}{\omega^3 \epsilon_0 \tau^2} \tag{2.29}$$

where, $\sigma \approx eN\mu$ is the conductivity of the doped silicon and e is the charge of an electron and ε_0 is the free space permittivity. The dielectric-like property of highly doped p-silicon is decreased due to high carrier concentration and the infinite frequency relative permittivity, ε_∞ approaches 1.

To achieve an accurate design, a rigorous numerical approach is needed to calculate the confinement factors, together with the change in the guided mode effective index by sensing. As to all practical optical waveguides with 2D confinement, the eigenmodes are classified as quasi-TE and quasi-TM modes, and they contain all the six components of the E and H fields. Thus, a full-vectorial numerical finite element method should be used to find accurate eigenmodes in these waveguides.

2.3. Finite Element Method

The Finite element method is a numerical procedure for obtaining solutions to boundary value problems. The principle of the method is to replace an entire continuous domain by several subdomains in which the unknown function is represented by simple interpolation functions with unknown coefficients. Thus, the original boundary value problem with an infinite number of degrees of freedom is converted into a problem with a finite number of degrees of freedom. Then a set of algebraic equations or a system of equations is obtained by applying Ritz variational or Galerkin [29], [30] procedure and finally, solution is achieved by solving system of equations. Therefore, a finite element analysis should include the following basic steps:

    a. **Discretization of the domain:** The discretization of domain, say Ω, is the first and the most important step in any finite element method because the way the domain is discretized will affect memory management, computation time and accuracy of the numerical results. In this method, the entire domain Ω is subdivided into several small

domains, denoted as $\Omega^e (e = 1,2,3, \dots, M)$ with M denoting the total of subdomains. These subdomains are referred to as elements. In most finite element solutions, the problem is formulated in terms of ϕ at nodes associated with the elements.

b. **Selection of the interpolation function:** The second step of a finite element analysis is to select an interpolation function that provides an approximation of the unknown solution within an element. The interpolation is usually selected to be a polynomial of first or second order. Once the order is selected, an expression can be derived for unknown solution in an element, say element e, in the following form:

$$\tilde{\phi} = \sum_{j=1}^{n} N_j^e \phi_j^e = \{N^e\}^T \{\phi^e\} = \{\phi^e\}^T \{N^e\} \tag{2.30}$$
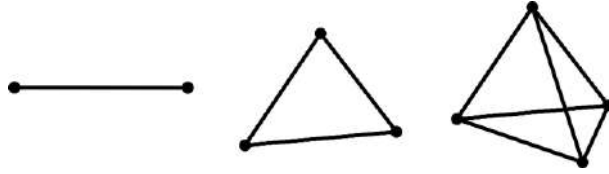
Figure 2.7: One dimensional, two dimensional and three-dimensional finite elements. [30]

c. **Formulation of the system of equations:** The third step, also a major step in a finite element method, is to formulate the system of equations. Both Ritz and Galerkin method can be used here.

In the Ritz method, the functional F given in equation 2.1 can be expressed as

$$F(\tilde{\phi}) = \sum_{e=1}^{M} F^e(\tilde{\phi}^e) \tag{2.31}$$

Here M is the number of elements comprising the entire domain.

The system of equations is obtained by minimizing the F:

$$\left\{\frac{\partial F}{\partial \phi}\right\} = \sum_{e=1}^{M} \left\{\frac{\partial \overline{F^e}}{\partial \phi^e}\right\} = \sum_{e=1}^{M} \left([\bar{K}^e]\{\bar{\phi}^e\} - \{\bar{b}^e\}\right) = 0 \tag{2.32}$$

Here bar means an extended or augmented matrix.

In the Galerkin method, the weighted residual for the eth element is:

$$R_e^i = \int_{\Omega^e} N_i^e \left(\mathcal{L}\tilde{\phi}^e - f\right) d\Omega \quad i = 1,2,3, \dots, n \tag{2.33}$$

It can be written in matrix form as:

$$\{R^e\} = [k^e]\{\phi^e\} - \{b^e\} \tag{2.34}$$

Since the expansion of the weighting function associated residual with a node spans all elements directly connected to the node, the weighted residual R_i associated with node i is the summation over the elements directly connected to node i. Therefore:

$$\{R\} = \sum_{e=1}^{M}\{\bar{R}^e\} = \sum_{e=1}^{M}[\bar{K}^e]\{\bar{\phi}^e\} - \{\bar{b}^e\} \tag{2.35}$$

The system of equations can be found by setting $\{R\} = 0$, resulting in:

$$\sum_{e=1}^{M}[\bar{K}^e]\{\bar{\phi}^e\} - \{\bar{b}^e\} = 0 \tag{2.36}$$

    d. Solution of the system of equations: From the above two methods ϕ is solved and updated at every iteration.

The following is an example of the basis functions for a triangular element.

For a linear triangular element, the unknown function ϕ within each element is approximated as follows:

$$\phi^e(x,y) = a^e + b^e x + c^e y \tag{2.37}$$

Where a^e, b^e and c^e are constant coefficients to be determined and e is the element number.
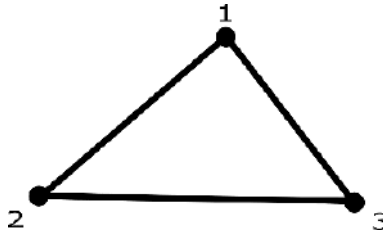
Figure 2.8: Linear triangular element [30]

For a linear triangular element, there are three nodes located at the vertices of the triangle. We number the nodes $1, 2$ and 3, with the corresponding values of ϕ denoted by ϕ_1^e, ϕ_2^e and ϕ_3^e respectively. Now we obtain three node equations:

$$\begin{aligned}
\phi_1^e &= a^e + b^e x_1 + c^e y_1 \\
\phi_2^e &= a^e + b^e x_2 + c^e y_2 \\
\phi_3^e &= a^e + b^e x_3 + c^e y_3
\end{aligned} \tag{2.38}$$

In matrix form the above equation can be expressed as follows:

$$\begin{bmatrix} \phi_1^e \\ \phi_2^e \\ \phi_3^e \end{bmatrix} = \begin{bmatrix} 1 & x_1 & y_1 \\ 1 & x_2 & y_2 \\ 1 & x_3 & y_3 \end{bmatrix} \begin{bmatrix} a^e \\ b^e \\ c^e \end{bmatrix} \tag{2.39}$$

Now the values of a^e, b^e and c^e in terms of ϕ_j^e $(j = 1,2,3)$ are as follows:

$$a^e = \frac{\begin{vmatrix} \phi_1^e & x_1 & y_1 \\ \phi_2^e & x_2 & y_2 \\ \phi_3^e & x_3 & y_3 \end{vmatrix}}{\begin{vmatrix} 1 & x_1 & y_1 \\ 1 & x_2 & y_2 \\ 1 & x_3 & y_3 \end{vmatrix}}, b^e = \frac{\begin{vmatrix} 1 & \phi_1^e & y_1 \\ 1 & \phi_2^e & y_2 \\ 1 & \phi_3^e & y_3 \end{vmatrix}}{\begin{vmatrix} 1 & x_1 & y_1 \\ 1 & x_2 & y_2 \\ 1 & x_3 & y_3 \end{vmatrix}}, c^e = \frac{\begin{vmatrix} 1 & x_1 & \phi_1^e \\ 1 & x_2 & \phi_2^e \\ 1 & x_3 & \phi_3^e \end{vmatrix}}{\begin{vmatrix} 1 & x_1 & y_1 \\ 1 & x_2 & y_2 \\ 1 & x_3 & y_3 \end{vmatrix}} \tag{2.40}$$

Using the values of a^e, b^e and c^e one can find the unknown function ϕ for each element.

$$\phi^e(x,y) = \frac{1}{2S_e} \left[(x_j y_k - x_k y_j) \phi_1^e + (x_k y_i - x_i y_k) \phi_2^e + (x_i y_j - x_j y_i) \phi_3^e \right]$$

$$+ \frac{1}{2S_e} \left[(y_j - y_k) \phi_1^e + (y_k - y_i) \phi_2^e + (y_i - y_j) \phi_3^e \right] x$$

$$+ \frac{1}{2S_e} \left[(x_j - x_k) \phi_1^e + (x_i - x_k) \phi_2^e + (x_j - x_k) \phi_3^e \right] y \tag{2.41}$$

$$\phi^e(x,y) = N_1^e \phi_1^e + N_2^e \phi_2^e + N_3^e \phi_3^e$$

$$= \sum_{i=1}^{3} N_i^e(x,y) \phi_i^e = [N^e]^T \{\phi^e\} = \{\phi^e\}^T [N^e] \tag{2.42}$$

Where $\{\phi^e\} = \begin{bmatrix} \phi_1^e \\ \phi_2^e \\ \phi_3^e \end{bmatrix}$ and $[N^e] = \begin{bmatrix} N_1^e \\ N_2^e \\ N_3^e \end{bmatrix}$

Therefore, it can be written as:

$$N_1^e(x,y) = \frac{1}{2S_e} \left[(x_j y_k - x_k y_j) + (y_j - y_k) + (x_j - x_k) \right]$$

$$N_2^e(x,y) = \frac{1}{2S_e} \left[(x_k y_i - x_i y_k) + (y_k - y_i) + (x_i - x_k) \right]$$

$$N_3^e(x,y) = \frac{1}{2S_e} \left[(x_i y_j - x_j y_i) + (y_i - y_j) + (x_j - x_k) \right] \tag{2.43}$$

So, basis functions are in general:

$$N_l^e(x,y) = \frac{1}{2S_e} (a_l^e + b_l^e x + c_l^e y) \quad (l = 1,2,3) \tag{2.44}$$

Here, S_e is the area of the element, and is given by:

$$S_e = \frac{1}{2} \begin{vmatrix} 1 & x_i & y_i \\ 1 & x_j & y_j \\ 1 & x_k & y_k \end{vmatrix} = \frac{1}{2}(x_j y_k - x_k y_j - x_i y_k + x_i y_j + y_i x_k - x_j y_i)$$

$$= \frac{1}{2}(b_1^e c_2^e - b_2^e c_1^e) \tag{2.45}$$

Laplace's equation:

$$\frac{\partial}{\partial x}\left(\epsilon_x \frac{\partial \phi}{\partial x}\right) + \frac{\partial}{\partial y}\left(\epsilon_y \frac{\partial \phi}{\partial y}\right) = 0$$

$$\epsilon_x \frac{\partial^2 \phi}{\partial x^2} + \epsilon_y \frac{\partial^2 \phi}{\partial y^2} = 0 \tag{2.46}$$

The Lagrangian functional is as follows:

$$F(\phi) = \frac{1}{2}\iint_\Omega [\,\epsilon_x \left(\frac{\partial \phi}{\partial x}\right)^2 + \epsilon_y \left(\frac{\partial \phi}{\partial y}\right)^2]dxdy \tag{2.47}$$

Poisson's equation is as follows:

$$\frac{\partial}{\partial x}\left(\epsilon_x \frac{\partial \phi}{\partial x}\right) + \frac{\partial}{\partial y}\left(\epsilon_y \frac{\partial \phi}{\partial y}\right) = -\rho_c$$

$$\epsilon_x \frac{\partial^2 \phi}{\partial x^2} + \epsilon_y \frac{\partial^2 \phi}{\partial y^2} = -\rho_c \tag{2.48}$$

The corresponding Lagrangian functional is given by:

$$F(\phi) = \frac{1}{2}\iint_\Omega [\,\epsilon_x \left(\frac{\partial \phi}{\partial x}\right)^2 + \epsilon_y \left(\frac{\partial \phi}{\partial y}\right)^2]d\Omega - \iint_\Omega \rho_c d\Omega \tag{2.49}$$

In general, $F(\phi) = \sum_{e=1}^{M} F^e(\phi^e)$, where M is the number of elements in the domain.

Since the unknown in each element is given by $\phi^e(x,y) = N_1^e \phi_1^e + N_2^e \phi_2^e + N_3^e \phi_3^e$

Now:

$$F^e(\phi^e) = \frac{1}{2}\iint_e \left[\epsilon_x \left(\phi_1^e \frac{\partial N_1^e}{\partial x} + \phi_2^e \frac{\partial N_2^e}{\partial x} + \phi_3^e \frac{\partial N_3^e}{\partial x} \right)^2 \right.$$

$$\left. + \epsilon_y \left(\phi_1^e \frac{\partial N_1^e}{\partial y} + \phi_2^e \frac{\partial N_2^e}{\partial y} + \phi_3^e \frac{\partial N_3^e}{\partial y} \right)^2 \right] dxdy$$

$$F^e(\phi^e) = \frac{1}{2}\iint_e [\epsilon_x\{ \left(\phi_1^e \frac{\partial N_1^e}{\partial x} \right)^2 + \left(\phi_2^e \frac{\partial N_2^e}{\partial x} \right)^2 + \left(\phi_3^e \frac{\partial N_3^e}{\partial x} \right)^2$$

$$+2\phi_1^e\phi_2^e\frac{\partial N_1^e}{\partial x}\frac{\partial N_2^e}{\partial x} + 2\phi_2^e\phi_2^e\frac{\partial N_2^e}{\partial x}\frac{\partial N_3^e}{\partial x} + 2\phi_3^e\phi_1^e\frac{\partial N_3^e}{\partial x}\frac{\partial N_1^e}{\partial x}\}$$

$$+\epsilon_y\{\left(\phi_1^e\frac{\partial N_1^e}{\partial y}\right)^2 + \left(\phi_2^e\frac{\partial N_2^e}{\partial y}\right)^2 + \left(\phi_3^e\frac{\partial N_3^e}{\partial y}\right)^2$$

$$+2\phi_1^e\phi_2^e\frac{\partial N_1^e}{\partial y}\frac{\partial N_2^e}{\partial y} + 2\phi_2^e\phi_2^e\frac{\partial N_2^e}{\partial y}\frac{\partial N_3^e}{\partial y} + 2\phi_3^e\phi_1^e\frac{\partial N_3^e}{\partial y}\frac{\partial N_1^e}{\partial y}\}]dxdy \qquad (2.50)$$

Taking derivative with respect to each ϕ:

$$\frac{\partial F^e}{\partial \phi_1^e} = \phi_1^e\iint\left[\epsilon_x\frac{\partial N_1^e}{\partial x}\frac{\partial N_1^e}{\partial x} + \epsilon_y\frac{\partial N_1^e}{\partial y}\frac{\partial N_1^e}{\partial y}\right]dxdy$$

$$+\phi_2^e\iint\left[\epsilon_x\frac{\partial N_1^e}{\partial x}\frac{\partial N_2^e}{\partial x} + \epsilon_y\frac{\partial N_1^e}{\partial y}\frac{\partial N_2^e}{\partial y}\right]dxdy$$

$$+\phi_3^e\iint\left[\epsilon_x\frac{\partial N_1^e}{\partial x}\frac{\partial N_3^e}{\partial x} + \epsilon_y\frac{\partial N_1^e}{\partial y}\frac{\partial N_3^e}{\partial y}\right]dxdy$$

$$=\sum_{l=1}^{3}\phi_l^e\iint\left[\epsilon_x\frac{\partial N_1^e}{\partial x}\frac{\partial N_l^e}{\partial x} + \epsilon_y\frac{\partial N_1^e}{\partial y}\frac{\partial N_l^e}{\partial y}\right]dxdy \qquad (2.51)$$

Thus, we can easily find $\frac{\partial F^e}{\partial \phi_2^e}$ and $\frac{\partial F^e}{\partial \phi_3^e}$. Now we can write:

$$\frac{\partial F^e}{\partial \phi_i^e} = \sum_{l=1}^{3}\phi_l^e\iint\left[\epsilon_x\frac{\partial N_i^e}{\partial x}\frac{\partial N_l^e}{\partial x} + \epsilon_y\frac{\partial N_i^e}{\partial y}\frac{\partial N_l^e}{\partial y}\right]dxdy \qquad (2.52)$$

Therefore, in matrix format we can write that:

$$\begin{bmatrix}\frac{\partial F^e}{\partial \phi_1^e}\\\frac{\partial F^e}{\partial \phi_2^e}\\\frac{\partial F^e}{\partial \phi_3^e}\end{bmatrix} = \iint_e \epsilon_x\begin{bmatrix}\frac{\partial N_1^e}{\partial x}\frac{\partial N_1^e}{\partial x} & \frac{\partial N_1^e}{\partial x}\frac{\partial N_2^e}{\partial x} & \frac{\partial N_1^e}{\partial x}\frac{\partial N_3^e}{\partial x}\\\frac{\partial N_2^e}{\partial x}\frac{\partial N_1^e}{\partial x} & \frac{\partial N_2^e}{\partial x}\frac{\partial N_2^e}{\partial x} & \frac{\partial N_2^e}{\partial x}\frac{\partial N_3^e}{\partial x}\\\frac{\partial N_3^e}{\partial x}\frac{\partial N_1^e}{\partial x} & \frac{\partial N_3^e}{\partial x}\frac{\partial N_2^e}{\partial x} & \frac{\partial N_3^e}{\partial x}\frac{\partial N_3^e}{\partial x}\end{bmatrix}\begin{bmatrix}\phi_1^e\\\phi_2^e\\\phi_3^e\end{bmatrix} dxdy$$

$$+\iint_e \epsilon_y\begin{bmatrix}\frac{\partial N_1^e}{\partial y}\frac{\partial N_1^e}{\partial y} & \frac{\partial N_1^e}{\partial y}\frac{\partial N_2^e}{\partial y} & \frac{\partial N_1^e}{\partial y}\frac{\partial N_3^e}{\partial y}\\\frac{\partial N_2^e}{\partial y}\frac{\partial N_1^e}{\partial y} & \frac{\partial N_2^e}{\partial y}\frac{\partial N_2^e}{\partial y} & \frac{\partial N_2^e}{\partial y}\frac{\partial N_3^e}{\partial y}\\\frac{\partial N_3^e}{\partial y}\frac{\partial N_1^e}{\partial y} & \frac{\partial N_3^e}{\partial y}\frac{\partial N_2^e}{\partial y} & \frac{\partial N_3^e}{\partial y}\frac{\partial N_3^e}{\partial y}\end{bmatrix}\begin{bmatrix}\phi_1^e\\\phi_2^e\\\phi_3^e\end{bmatrix} dxdy \qquad (2.53)$$

i.e.,

$$\left\{\frac{\partial F^e}{\partial \phi^e}\right\} = [K^e]\{\phi^e\} \qquad (2.54)$$

with

$$K_{ij}^e = \iint_e \left[\epsilon_x \frac{\partial N_i^e}{\partial x} \frac{\partial N_j^e}{\partial x} + \epsilon_y \frac{\partial N_i^e}{\partial y} \frac{\partial N_j^e}{\partial y} \right] dxdy \quad i,j = 1,2,3 \tag{2.55}$$

then

$$[K^e] = \iint_e \left[\epsilon_x \frac{\partial \{N\}}{\partial x} \frac{\partial \{N\}^T}{\partial x} + \epsilon_y \frac{\partial \{N\}}{\partial y} \frac{\partial \{N\}^T}{\partial y} \right] dxdy \tag{2.56}$$

Finally, the global system can be obtained from

$$\left\{ \frac{\partial F}{\partial \phi} \right\} = \sum_{e=1}^M \left\{ \frac{\partial \bar{F}^e}{\partial \phi^e} \right\} = \sum_{e=1}^M [\bar{K}^e]\{\bar{\phi}^e\} = 0 \tag{2.57}$$

Which gives

$$[K]\{\phi\} = 0 \tag{2.58}$$

Where $[K] = \sum_{e=1}^M [\bar{K}^e]$

Applying boundary conditions, we can deduce the form like*:*

$$[K']\{\phi'\} = \{b\} \tag{2.59}$$

The final equation can be solved by using any available FEM solver like COMSOL Multiphysics.

2.4.   Frequency Domain Electromagnetic Field Modeling

If we are modeling at a known frequency in COMSOL Multiphysics, where both the electric fields and the magnetic fields are significant, or induced currents are present, we will need to consider either the AC/DC Module, RF Module, or Wave Optics Module. The AC/DC Module offers a Frequency Domain form of the Magnetic Fields interface*:*

$$\nabla \times \mu^{-1}(\nabla \times \boldsymbol{A}) + (j\omega\sigma - \omega^2\epsilon)\boldsymbol{A} = \boldsymbol{J_s} \tag{2.60}$$

This solves for the magnetic fields, the electric fields $\boldsymbol{E} = j\omega\boldsymbol{A}$, as well as the induced currents, $\boldsymbol{J}_i = \sigma\boldsymbol{E}$.

The above equation is quite like the Electromagnetic Waves, Frequency Domain interface offered in both the RF and the Wave Optics modules, shown below*:*

$$\nabla \times \mu_r^{-1}(\nabla \times \boldsymbol{E}) - \omega^2 \epsilon_0 \mu_0 \left(\epsilon_r - \frac{j\sigma}{\omega\epsilon_0} \right) \boldsymbol{E} = 0 \qquad (2.61)$$

There are a couple of helpful concepts here that will help us decide which module to use. First, find the electrical size of the object we are modeling. Consider the maximum dimension of the object we are analyzing, L_c, and compare it to the free space wavelength at the operating frequency we are simulating: $\lambda = \frac{c}{f}$. The electrical size is the ratio of these two. If the object size is much smaller than wavelength, $L_c < \sim \frac{\lambda}{100}$, then it is likely that it is in the quasi-static regime, and the AC/DC Module is more appropriate. On the other hand, if the object size is comparable to the wavelength, then it is likely that the object will act as an antenna, as a transmission line or waveguide, or as a resonator. If we are trying to solve any kind of antenna, wave scattering, or resonant cavity problem, then the RF or Wave Optics modules should be used. (Note that this is independent of the operating frequency; it is only the ratio of object size to wavelength that matters.) There is some region of overlap between the AC/DC and the RF Modules, where either formulation could be used, and if we are right at the boundary between the regions of applicability, we may want to use both, depending on how wide of a frequency band we are simulating.
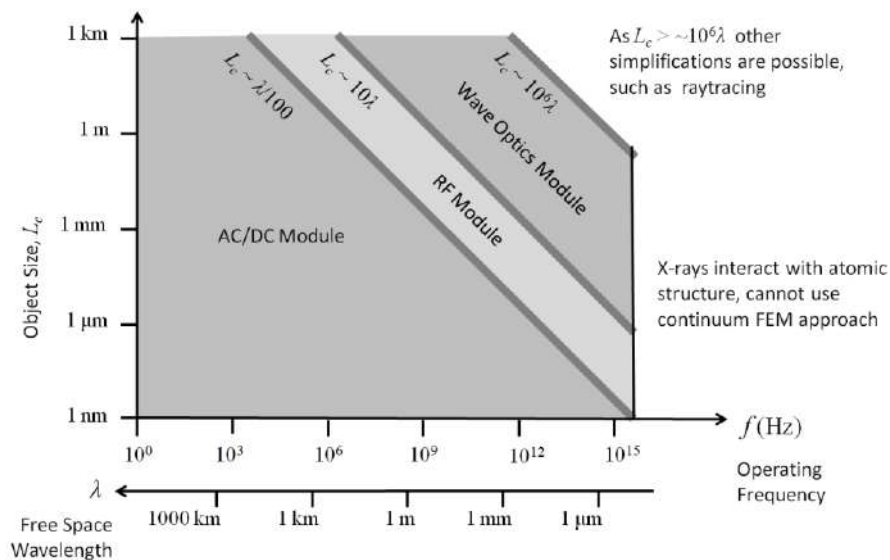
Figure 2.9: The range of applicability of the AC/DC, RF, and Wave Optics Modules, based on the operating frequency. [31]

As the object size, L_c, gets larger that the wavelength, $L_c > 10\lambda$, the models we build will become increasingly more computationally demanding (not a big problem in 2D, but for 3D modeling). In fact, for 3D models, Electromagnetic Waves, Frequency Domain form can only

practically be used up to an object size of about $10\lambda \times 10\lambda \times 10\lambda$. A model of that size would already take a 64GB RAM computer to solve, and memory requirements will grow as $O(L_c^3)$. For objects much larger than the wavelength, the Wave Optics Module can be appropriate.

In our proposed model we will use the RF module as our object size and wavelength fall into the RF module region.

Chapter 3

CONVENTIONAL SLOT WAVEGUIDES

3.1. Vertical Slot Waveguide

Conventional SOI slot waveguide [32], [33] (whose structure is shown in Fig. 3.1 modal behavior has been investigated by full-vectorial 2D FEM [19], [34], [35], assuming as cover medium air, silicon oxide or an aqueous solution (cover medium refractive index n_c equal to 1, 1.444 or 1.33, respectively). The following figures and simulations have been reproduced based on the paper for better understanding [16].
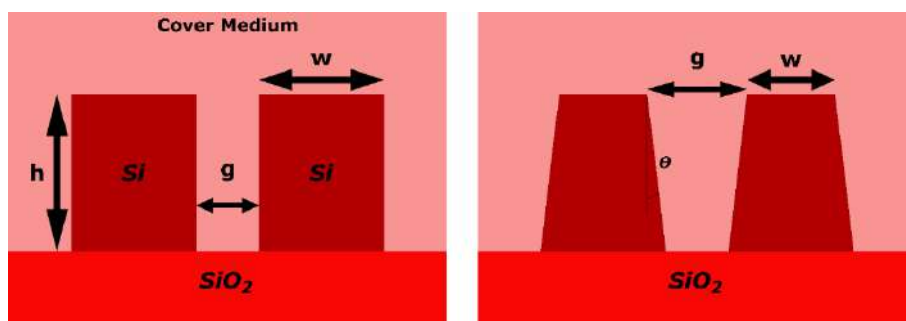
Figure 3.1: Vertical slot waveguide

In FEM mesh generation for effective index and modal profile calculation, triangular vector-elements have been adopted and maximum element size has been fixed as equal to $2.5 \, nm$ in the gap region, $3 \, nm$ in the Si wires region, $10 \, nm$ in the portion of calculation domain outside both gap region and Si wires region and included in a large rectangle $1 \, \mu m$ wide and $0.45 \, \mu m$ high centered in the center of the gap region, and $100 nm$ in the remaining domain portion having a total area of $8 \, \mu m^2$ ($4 \, \mu m \times 2 \, \mu m$). In total, we have always used about $100,000$ mesh elements. Changing the boundary condition from a perfect electric conductor to a perfect magnetic conductor has a negligible influence on the simulation results. Adopting these mesh parameters, the conventional slot waveguide fabricated has been simulated.

Assuming silicon wires with height $h = 250 \, nm$, width $w = 180 \, nm$ and gap region width $g = 100 \, nm$, the effective index change as induced by non-vertical sidewalls with respect to ideal case (vertical sidewalls), has been calculated. Tilting angle θ (Fig. 3.1) with respect to the vertical direction has been varied in the range from 3° to 9°, and quasi-TE and quasi-TM

modes have been considered. A linear dependence on effective index changes on θ has been observed for both polarizations. Non-vertical sidewalls influence on effective index is stronger for quasi-TE than for quasi-TM mode, because the relevant electric field squared module has its maxima along the vertical interfaces between silicon wires and gap region for quasi-TE mode, while the maxima are outside the gap region for quasi-TM mode. An increase of cover medium refractive index produces a decrease of θ influence on effective index, as it is shown in Fig. 3.2.
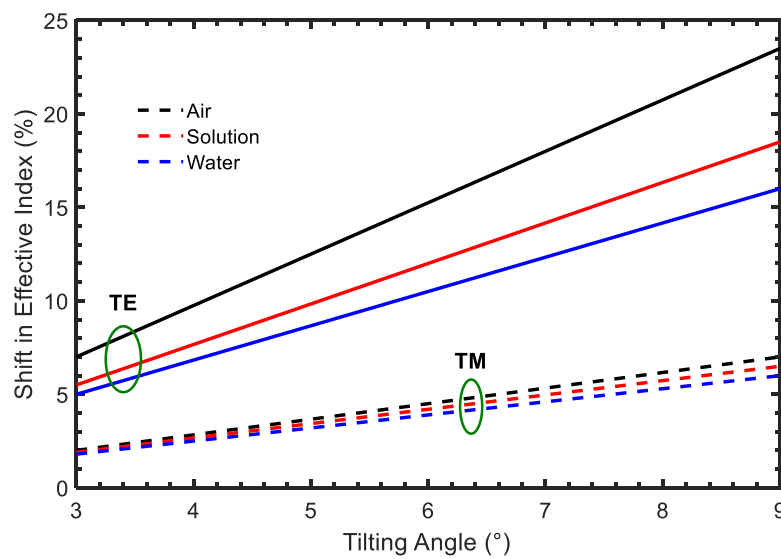
Figure 3.2: Percentage shift of quasi-TE and quasi-TM mode effective indices versus θ
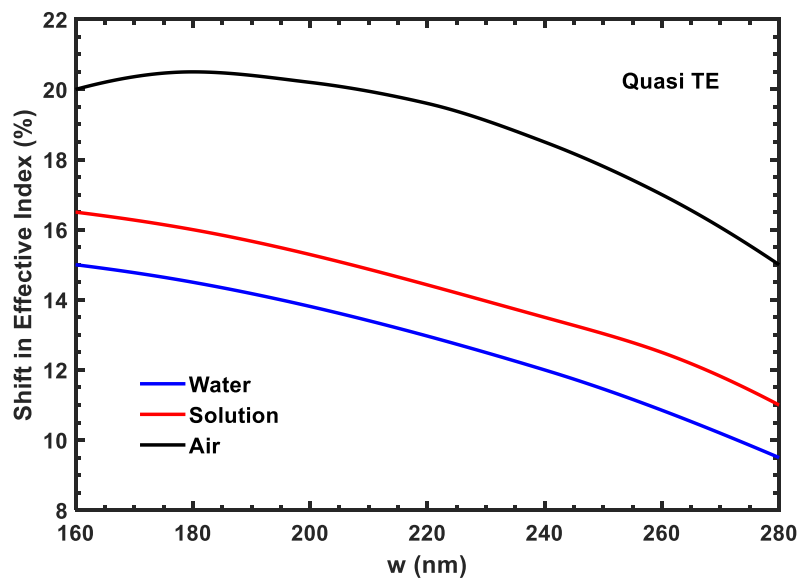
Figure 3.3: Percentage shift of quasi-TE effective indices (with respect to vertical case) versus w

Assuming $\theta = 8°$, $g = 100\ nm$ and $h = 250\ nm$, the effective index change induced by non-vertical sidewalls has been investigated as a function of w for quasi-TE and quasi-TM modes (Fig. 3.3 and Fig. 3.4). If the cover medium is silicon oxide or an aqueous solution, this change monotonically decreases by increasing the silicon wire width. When the cover medium is air, the dependence of effective index shift on w exhibits a maximum for $w = 180\ nm$ (maximum values are 20.5 % and 6.15% for quasi-TE and quasi-TM mode, respectively).
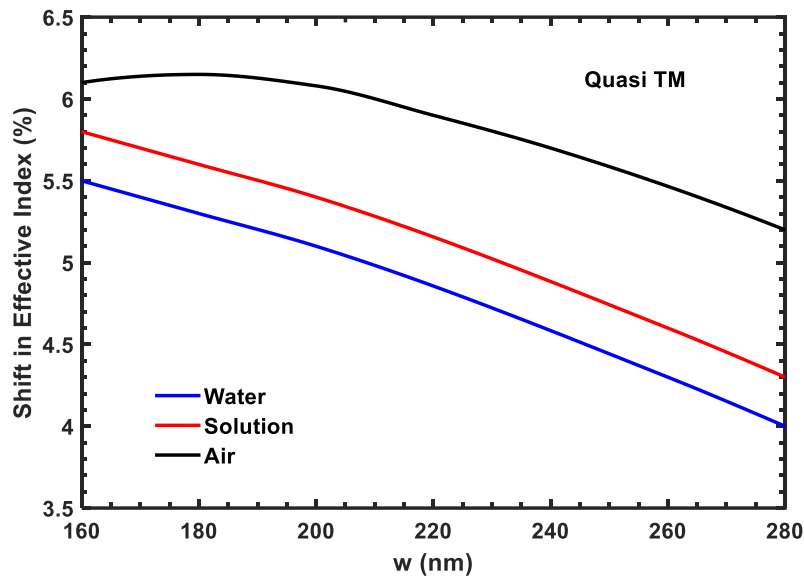
Figure 3.4: Percentage shift of quasi-TM effective indices (with respect to vertical case) versus w
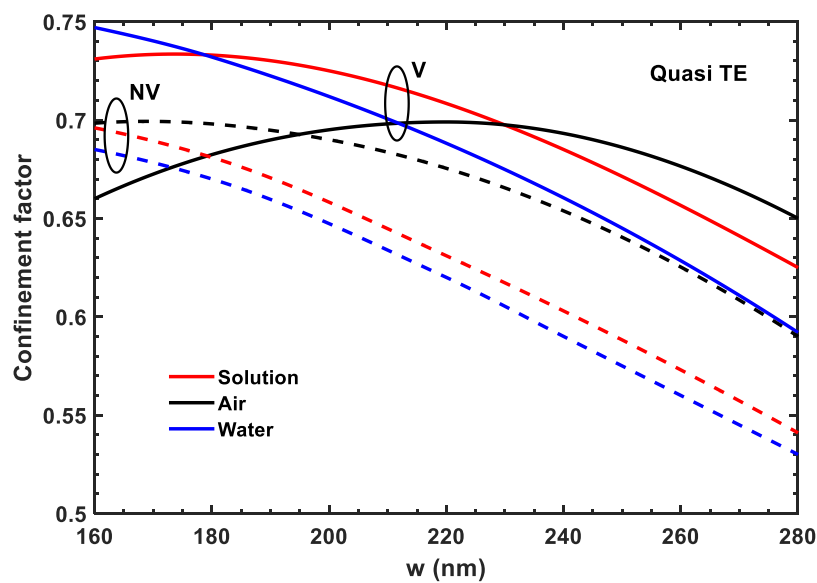
Figure 3.5: Confinement factors in cover medium (TE mode)

Dependence of confinement factors Γ_C and Γ_G on w has been investigated for $g = 100\ nm$ and $h = 250\ nm$. Effect of non-vertical sidewalls ($\theta = 8°$) on these factors has been also considered, as shown in Fig. 3.5 and Fig. 3.6. The confinement factors are larger for quasi-TE than for quasi-TM mode. For quasi-TE mode, non-vertical sidewalls produce a decrease in Γ_C and an increase in Γ_G. For quasi-TM mode, non-vertical sidewalls produce a decrease of both confinement factors.

For both polarizations, when the cover medium is an aqueous solution or silicon oxide, Γ_C monotonically decreases when w increases whereas, when the cover medium is air, Γ_C exhibits a maximum. Confinement factor Γ_G has a maximum in quite all considered cases (only when we consider silicon oxide, non-vertical sidewalls, and quasi-TM mode, Γ_G dependence on w is monotone.
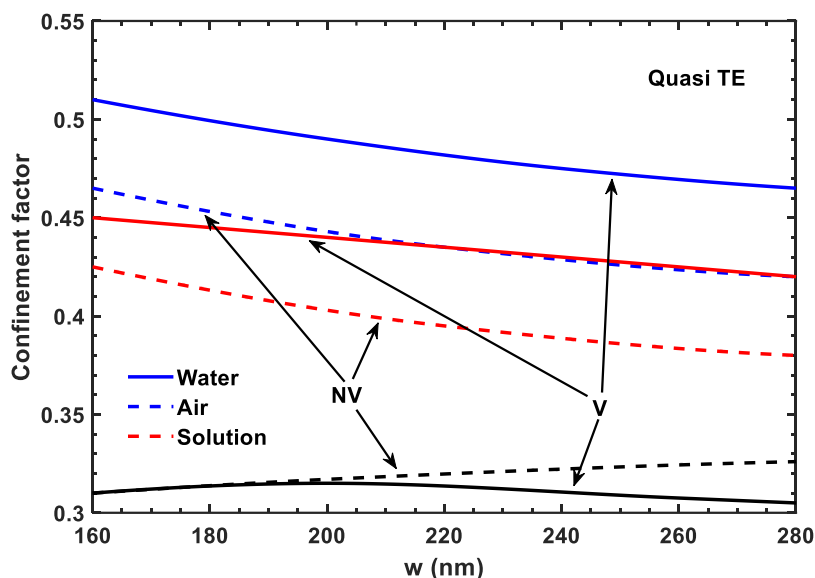
Figure 3.6: Confinement factors in cover medium (TM mode)

Surface sensing is exploited in a wide range of biochemical applications, such as DNA sequencing by hybridization, antigen-antibody reactions study or pollution concentration measures in water. This kind of sensing is based on immobilization of an ultra-thin layer of receptor molecules on the guiding film surface. The interaction between analyte and receptor molecules produces a change of molecular adlayer thickness, affecting the effective index of propagating optical mode.

Conventional slot and slot rib waveguides can be used for surface sensing immobilizing an ultra-thin layer of receptor molecules on Si/cover medium interface. In FEM mesh generation

for sensitivity calculation, the same parameters as in modal investigation have been used. In molecular adlayer region, maximum element size is equal to $1\ nm$. The increase of number of mesh elements around 30% produces a negligible change of surface sensitivity, lower than 0.4%.

Assuming $h = 250\ nm$, conventional slot waveguide surface sensitivity has been investigated as a function of Si-wire width w, for g equal to $100\ nm$ and $200\ nm$ and for both polarizations. As cover medium, an aqueous solution having a constant refractive index 1.33 has been again assumed. Molecular adlayer refractive index has been assumed as 1.45. Either vertical or non-vertical ($\theta = 8°$) sidewalls have been considered. The results are shown in Fig. 3.7 and Fig. 3.8.

Figure 3.7: Confinement factors in gap medium (TE mode)
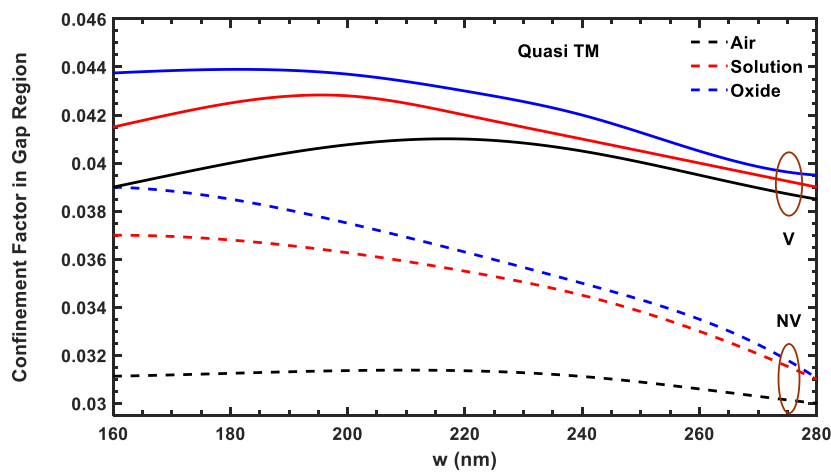
Figure 3.8: Confinement factors in gap medium (TM mode)

Conventional slot and slot rib waveguides can be used for surface sensing immobilizing an ultra-thin layer of receptor molecules on Si/cover medium interface.

In FEM mesh generation for sensitivity calculation, the same parameters as in modal investigation have been used. In molecular adlayer region, maximum element size is equal to $1\ nm$. The increase of number of mesh elements around 30% produces a negligible change of surface sensitivity, lower than 0.4%.

Assuming $h = 250\ nm$, conventional slot waveguide surface sensitivity has been investigated as a function of Si-wire width w, for g equal to $100\ nm$ and $200\ nm$ and for both polarizations. As cover medium, an aqueous solution having a constant refractive index 1.33 has been again assumed. Molecular adlayer refractive index has been assumed as 1.45. Either vertical or non-vertical ($\theta = 8°$) sidewalls have been considered. The results are shown in Fig. 3.7 and Fig. 3.8.

Figure 3.9: Slot waveguide surface sensitivity versus w, for vertical sidewalls

In conventional slot waveguide, quasi-TM mode is significantly more sensitive than quasi-TE one to deposited adlayer thickness increase. For both polarizations, sensitivity increases by increasing w. For quasi-TE mode, non-vertical sidewalls produce a surface sensitivity decrease whereas, for quasi-TM mode, non-verticality determinates a sensitivity increase. Maximum surface sensitivity $(4.05 \times 10^{-4}\ nm^{-1})$ is obtained for $w = 280\ nm$, $g = 100\ nm$ and quasi-TM mode. For $w = 280\ nm$, sensitivity dependence on gap region width has been investigated by considering both polarization (Fig. 3.9 and Fig. 3.10). For quasi-TM mode, surface sensitivity monotonically decreases when g increases whereas, for quasi-TE mode, surface sensitivity exhibits a maximum for $g = 70\ nm$. For conventional slot waveguide,

maximum sensitivity $(4.31 \times 10^{-4} \, nm^{-1})$ has been obtained when $g = 60 \, nm$, $h = 250 \, nm$, $w = 280 \, nm$ (quasi-TM mode).
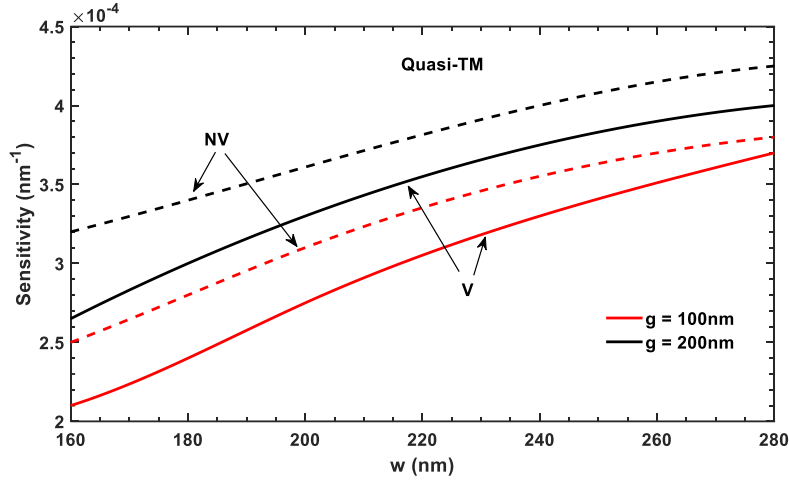
Figure 3.10: Slot waveguide surface sensitivity versus w, for slanted sidewalls

3.2.   Vertical Slot Waveguide With Ag Layer

In the structure (Fig. 3.11), a thin SiO_2 layer is sandwiched between Ag and silicon slot waveguides [36]–[38]. It is assumed that the over claddings are filled with acetylene gas in both slot waveguides, and the refractive indexes of amorphous $Si \, (a-Si)$, Si, SiO_2, acetylene gas, and Ag are 3.455, 3.455, 1.445, 1.000593, and $0.1453 - j11.3587$, respectively. In the metal-assisted slot waveguide, the core material is assumed to be $a - Si$ [39] because the structure is multilayered. The Si-width, slot width, and waveguide height are denoted as w, w_s, and H respectively. The thickness of the SiO_2 layer is denoted as t. The following figures and simulations have been reproduced based on the paper for better understanding [40].
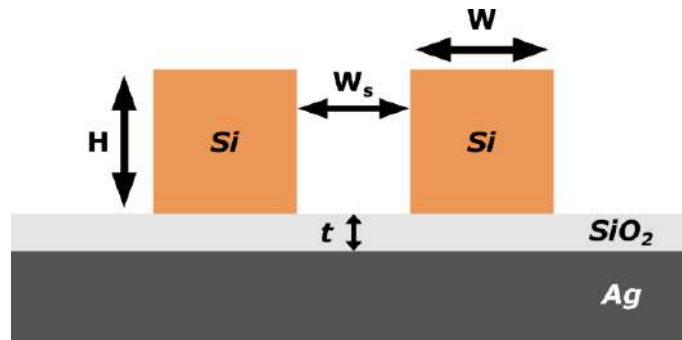
Figure 3.11: Vertical Slot Waveguide with Ag layer under the SiO_2 layer

All the 2-D simulations are conducted with the wavelength of $1550\ nm$. The proposed structure is compatible with existing CMOS fabrication processes and can be constructed as follows*:* After the Ag layer is coated on the Si wafer with the SiO_2 layer, amorphous silicon is deposited onto the SiO_2 surface. Then, the amorphous silicon layer is etched to form a slot waveguide. Fig. 3.12 shows the electric field distributions of the metal-assisted silicon slot waveguide ($w = 0.29\ \mu m$, $w_s = 0.1\ \mu m$, $H = 0.22 \mu m$, $t = 0.05 \mu m$) for the TE mode and the TM mode, respectively. For the TE mode that is used in the structure, the light concentration in the gas region is remarkable compared with the TM mode that has been frequently used in SPP-based waveguides. In the same Fig. the electric field distribution of the conventional silicon slot waveguide ($w = 0.29 \mu m$, $w_s = 0.1 \mu m$, $H = 0.22 \mu m$) is shown. The light confinement of the under cladding region in the proposed structure is weaker than the conventional slot waveguide. These characteristics facilitate a large confinement of light in the over cladding.
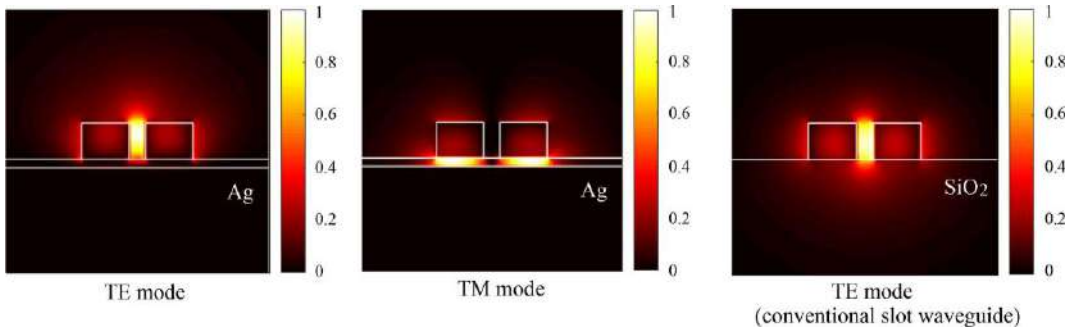
Figure 3.12: Light confinement in the Vertical Slot Waveguide with Ag layer under the SiO_2 layer for TE and TM mode

Fig. 3.13 illustrates the dependence of the effective refractive index, n_{eff}, on the Si-width, w, for both the conventional silicon slot waveguide and the metal-assisted silicon slot waveguide. As the Si-width of the slot waveguides increases, the effective refractive index also increases. In order to maintain guided modes, the real part of the effective refractive index should be less than the second-largest refractive index. For the photonic slot waveguide without metal, the cut-off condition is when the real part of n_{eff} is less than 1.445, which corresponds to the refractive index of SiO_2. However, in the proposed structure with metal, acetylene gas has a substantial refractive index due to reflection at the metal layer with the thin SiO_2 layer. In this case, the cut-off condition is when the real part of n_{eff} is less than 1.000593. It should be noted that all plotted points, including those with $n_{eff}<1.445$ for the blue and purple lines, indicate guided modes.
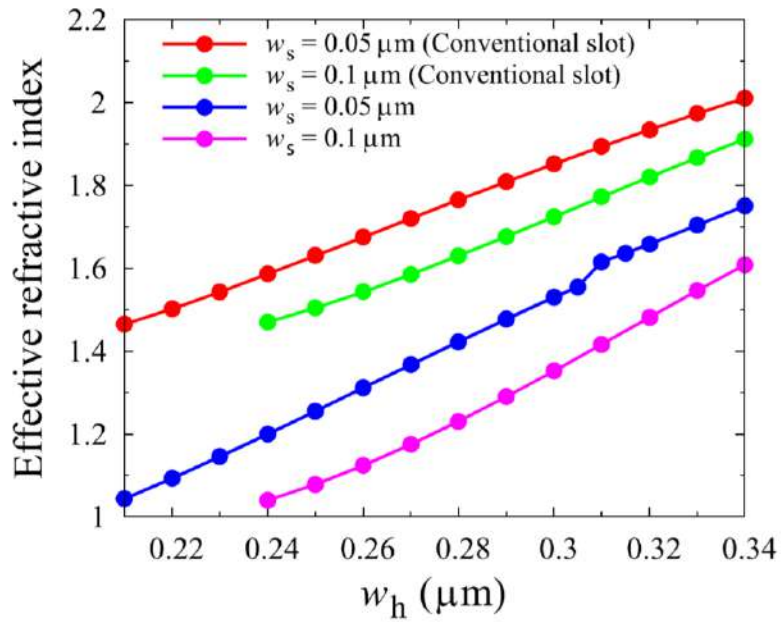
Figure 3.13: Effective refractive index as a function of w_h
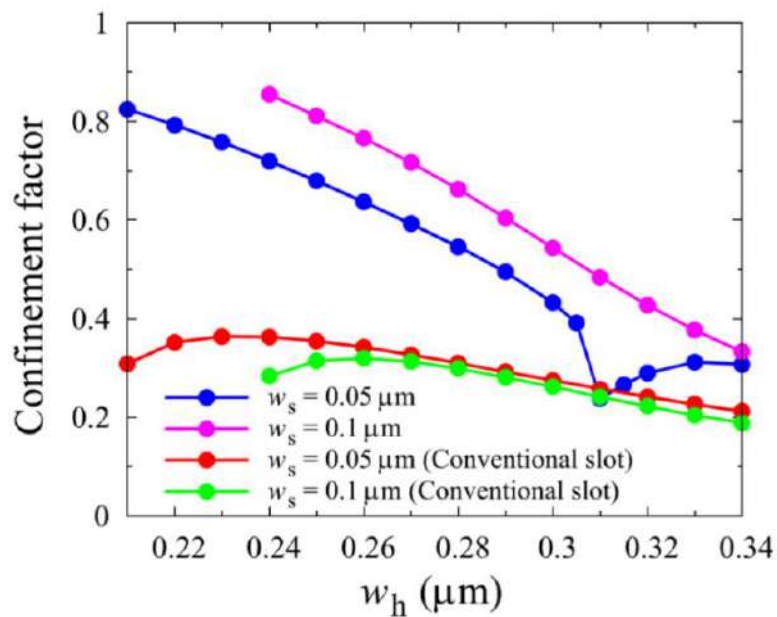
Figure 3.14: Optical confinement factor as a function of w_h

Fig. 3.14 displays the optical confinement factor in the gas region of both slot waveguides as a function of the Si-width. The metal-assisted silicon slot waveguide exhibits a higher optical confinement factor than the conventional slot waveguide. The maximum confinement factor of 85% is achieved in the proposed structure when $w = 0.24\mu m$ and $w_s = 0.1\mu m$, whereas the conventional structure only achieves a maximum confinement factor of 36% when $w = 0.23\mu m$ and $w_s = 0.05\mu m$. The significant improvement in light confinement is attributed to the large reflection by the metal. It is worth noting that a rapid decline in the optical

confinement factor at $t = 0.31\mu m$ for the blue line is due to mode coupling between the TE mode and the TM mode.

As the sensitivity of the device is determined by the ratio between the shift in the resonant wavelength and the shift in the refractive index of the gas, we evaluate the values of $\lambda_0 \Gamma / n_{eff}$ (nm/RIU). Fig. 3.15 shows the sensitivity of both slot waveguides as a function of the Si-width w_h when assuming $\lambda_0 = 1550nm$. From Fig. 3.16, we find that the sensitivity of the proposed structure exceeds $1000 \ nm/RIU$. This value is more than two times as large as the sensitivity of the conventional slot waveguide. As metal is introduced in the proposed structure, it is necessary to estimate the propagation loss due to the optical absorption in the metal. Fig. 3.16 shows the propagation length as a function of the Si-width. The propagation length L_{prop}, which is determined by the condition that light intensity attenuates to $\frac{1}{e}$, is given by [19]

$$L_{prop} = \frac{1}{|2Im(\beta)|} \tag{3.1}$$
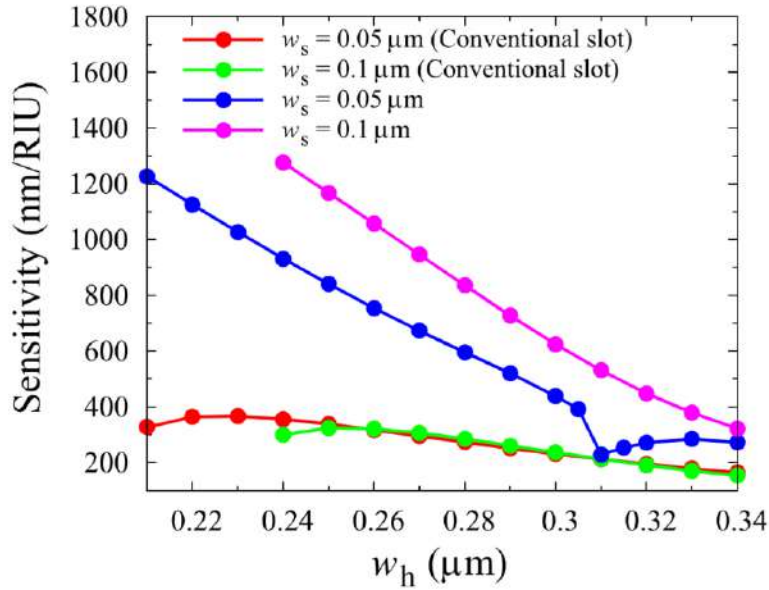
Figure 3.15: Sensitivity as a function of w_h

In this section, we examine the impact of SiO_2 thickness on the light confinement in the gas region, which is crucial to determine the distance between the core region and the Ag layer. Fig. 3.17 displays the effective refractive index plotted against t for $w_s = 0.1\mu m$. It reveals that the effective refractive index increases with t. As t increases, our structure approaches a conventional slot waveguide. Figs. 3.18 and 3.19 depict the optical confinement factor and sensitivity, respectively, with respect to t when $w_s = 0.1\mu m$. These two graphs are similar

because the optical confinement factor is proportional to sensitivity. The optical confinement factor and sensitivity decline as t increases due to a decrease in metal reflection effects. Additionally, significant declines are observed at $t = 0.12\mu m$ and $w = 0.26\mu m$ (indicated by the red line) and at $t = 0.09\mu m$ and $w = 0.3\mu m$ (indicated by the green line). Fig. 3.20 demonstrates the propagation length as a function of t for $w_s = 0.1\mu m$. As the structure approaches a conventional slot waveguide, losses caused by the metal gradually decrease. For instance, when $t = 0.3$ and $w = 0.26\mu m$, the propagation length is approximately $1000~\mu m$.

Figure 3.16: Propagation length as a function of w_h
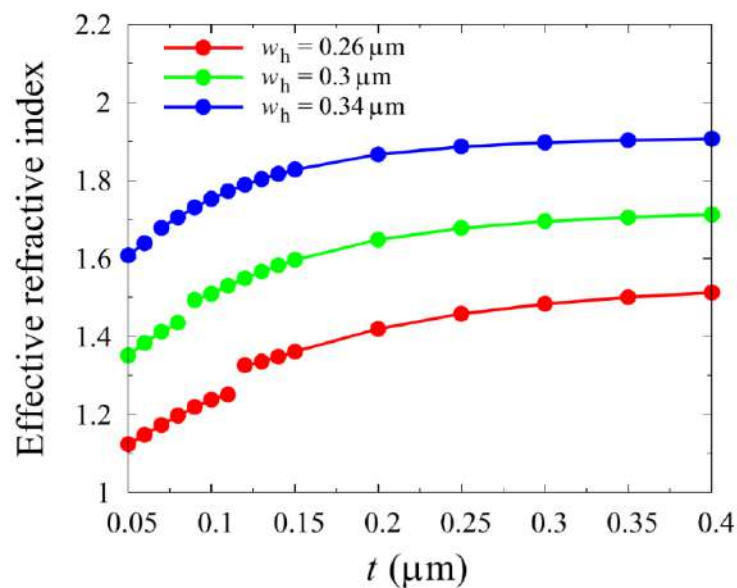
Figure 3.17: Effective refractive index as a function of t

In this section, we examine the impact of SiO_2 thickness on the light confinement in the gas region, which is crucial to determine the distance between the core region and the Ag layer. Fig. 3.17 displays the effective refractive index plotted against t for $w_s = 0.1\mu m$. It reveals that the effective refractive index increases with t. As t increases, our structure approaches a conventional slot waveguide.
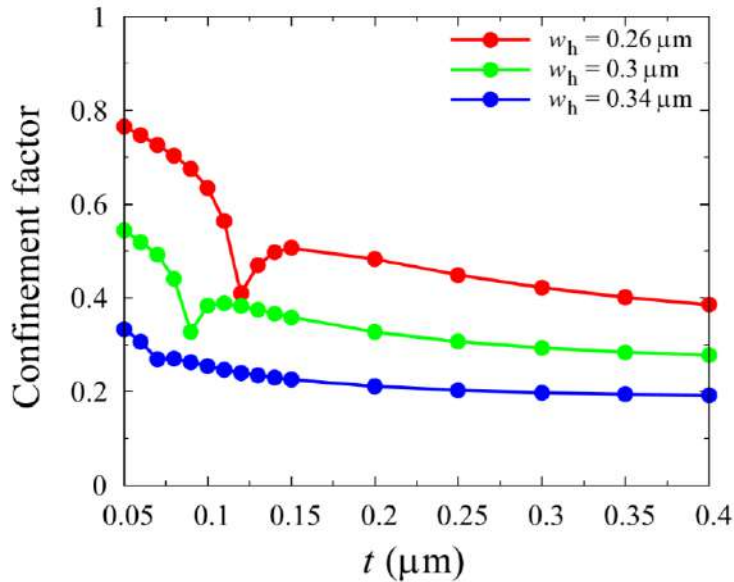
Figure 3.18: Optical confinement factor as a function of t
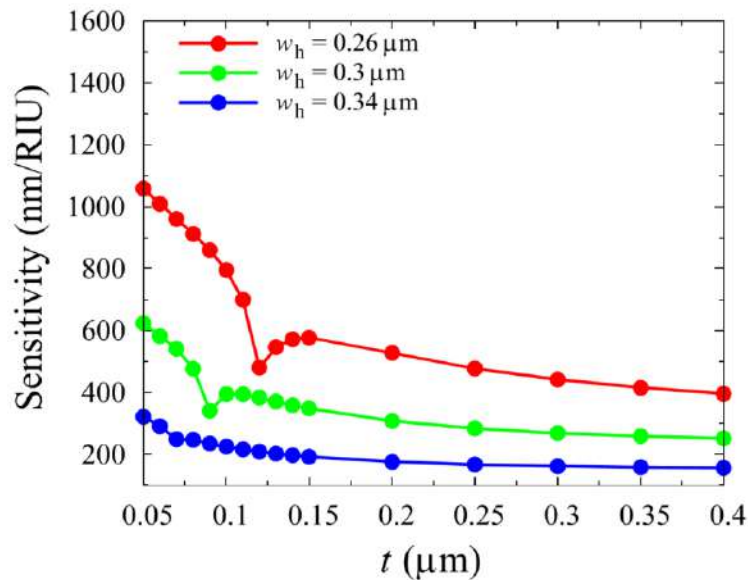
Figure 3.19: Sensitivity as a function of t

Figs. 3.18 and 3.19 depict the optical confinement factor and sensitivity, respectively, with respect to t when $w_s = 0.1\mu m$. These two graphs are similar because the optical confinement

factor is proportional to sensitivity. The optical confinement factor and sensitivity decline as t increases due to a decrease in metal reflection effects. Additionally, significant declines are observed at $t = 0.12\mu m$ and $w = 0.26\mu m$ (indicated by the red line) and at $t = 0.09\mu m$ and $w = 0.3\mu m$ (indicated by the green line). Fig. 3.20 demonstrates the propagation length as a function of t for $w_s = 0.1\mu m$. As the structure approaches a conventional slot waveguide, losses caused by the metal gradually decrease. For instance, when $t = 0.3$ and $w = 0.26\mu m$, the propagation length is approximately $1000 \ \mu m$.

Figure 3.20: Propagation length as a function of t

3.3.   Cross-Slot Waveguide

We will proceed to our result in several steps. First, we will analyze both vertical and horizontal waveguide separately. Secondly, we will make a combination of vertical and horizontal waveguide. Finally, we will add a metallic barrier around the silicon cores. The following figures and simulations have been reproduced based on the paper for better understanding [41].

First, biochemical sensors based on vertical and horizontal slot waveguides are characterized. The structure of a typical vertical slot waveguide for biochemical sensing is shown in Fig. 3.21. The waveguide is completely covered with a thin sensing layer with a refractive index value of 1.45. Refractive indices of silicon core, SiO_2 substrate, and the aqueous solution are taken as 3.47548, 1.44402, and 1.33, respectively. Initially, the sensing layer thickness, τ and the slot width, W_S are taken as 5 and 100 nm, respectively.
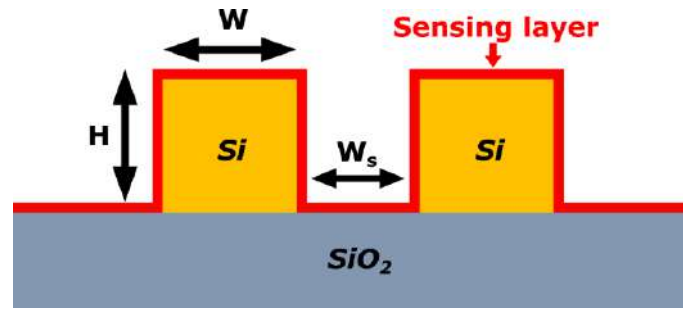
Figure 3.21: Vertical slot waveguide
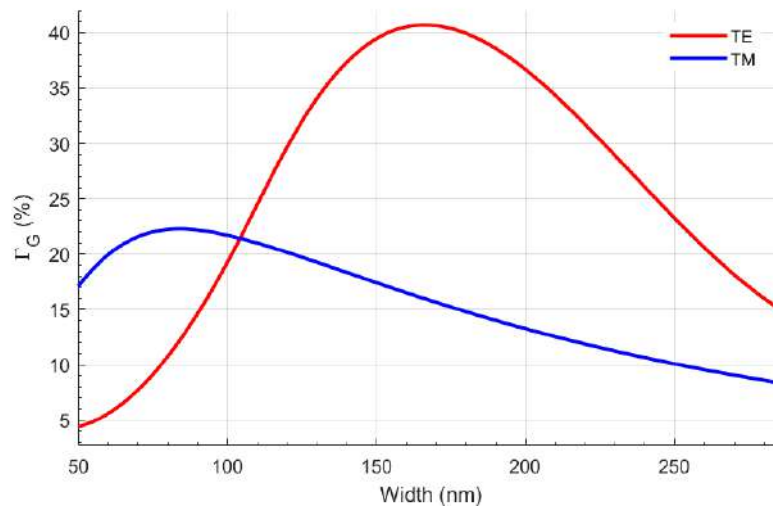
Figure 3.22: Variation with width
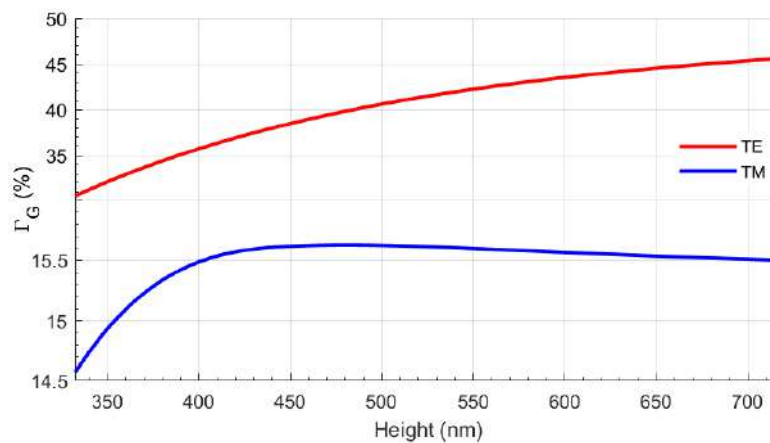
Figure 3.23: Variation with height

For this work, in optimizing the dimension of the silicon cores, Γ_G is taken as the optimization parameter. It can be observed that confinement factors in the slot region, Γ_G for both the polarizations increase at first and then decrease with the increase of the silicon core width, but

they have their peaks at different values of the width (Fig. 3.22). The Γ_G for the E_x mode reach its maximum value of 40.7% when the width is $160\ nm$, while Γ_G for the E_y mode reach its maximum value of only 21.9% when the width is $80\ nm$. Obviously, as for a vertical slot, the dominant E_x field of the E_x mode is enhanced in the slot region, and thus the maximum value of Γ_G for the E_x mode is nearly double than that for the E_y mode. As a result, in a vertical slot waveguide, quasi-TE mode should be employed as the operating polarization. Variations of Γ_G for the E_x and E_y modes with the silicon core height, H of a vertical slot waveguide are shown in Fig. 3.23 by red and blue lines, respectively. Widths of the silicon core and slot are taken as 160 and $100\ nm$, respectively. It is shown here that with the increase in height, Γ_G for the E_x mode increases monotonically but slows down at a larger height. On the other hand, Γ_G for the E_y mode increases at first and decreases slightly after reaching the highest value, but this is much smaller.

Next, optimization of a horizontal slot waveguide for biochemical sensing is carried out. The horizontal slot waveguide with aqueous solution or air in the slot region, which is designed to relate to tapered and feed waveguides, can be fabricated by controlling the etching process. Here, the horizontal slot height is taken as $100\ nm$.
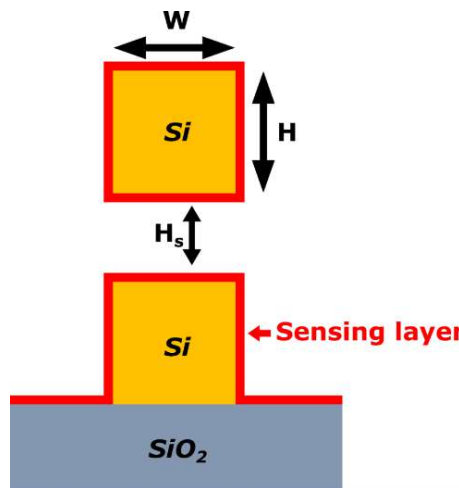
Figure 3.24: Horizontal waveguide

The structure of a typical vertical slot waveguide for biochemical sensing is shown in Fig. 3.24. Variations of Γ_G for the E_x and E_y modes with the silicon core height, H, for $W = 500\ nm$ are shown in Fig. 3.25 by solid red and blue lines, respectively, while those for $W = 750\ nm$, are shown by dashed red and blue lines, respectively. It can be observed that Γ_G for the E_y mode

increases at first, reaches its maximum value of 38.9% when $H = 170 \, nm$ and then decreases with the further increase of silicon core height.
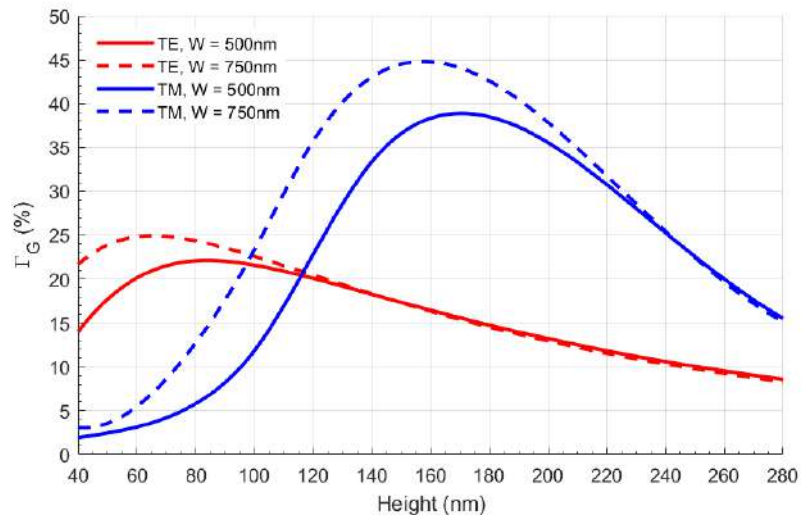
Figure 3.25: Variation with height
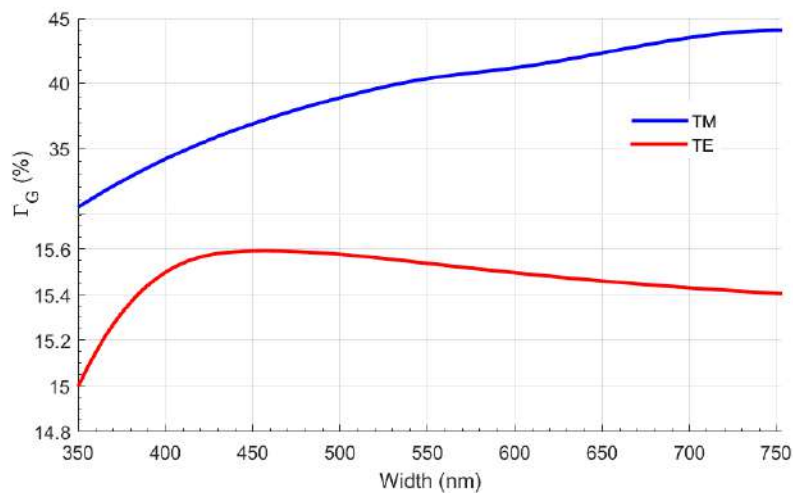
Figure 3.26: Variation with width

The maximum value of Γ_G for the E_y mode is significantly bigger than that for the E_x mode, as the dominant E_y field of E_y mode is enhanced in the horizontal slot region. It can also be observed that when the width is increased from 500 to 750 nm, for the E_y mode can reach its peak value, up to 44.6%, but at a slightly lower height, $H = 160 \, nm$. Variations of Γ_G for the E_x and E_y modes with the silicon core width, W of a horizontal slot waveguide whose height is set to 170 nm, are also shown in Fig. 3.26. Their tendencies are like those of Γ_G for the E_x mode in a vertical slot waveguide but with the silicon core height. Overall, it is true that there

is a strong correspondence between the vertical and horizontal slot waveguides, and the variation characteristics of Γ_G for the E_x and E_y modes with the silicon core width and height for a vertical slot waveguide are nearly similar as the variation characteristics of Γ_G for the E_y and E_x modes with the silicon core height and width for a horizontal slot waveguide, respectively.
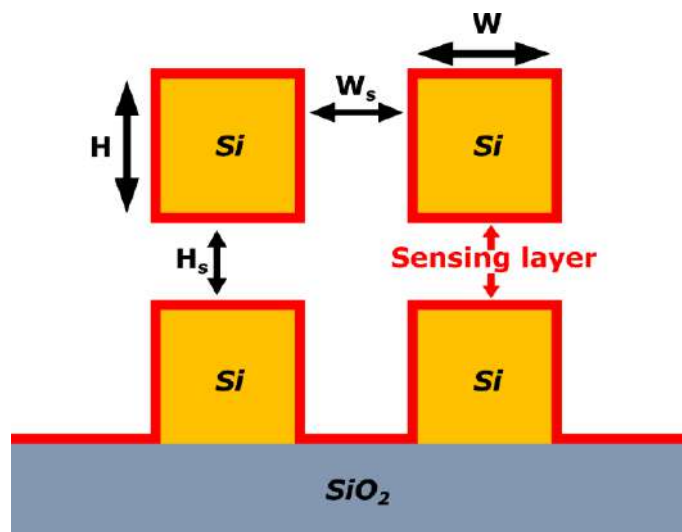
Figure 3.27: Cross-slot waveguide

In this section, a cross-slot waveguide [42] for biochemical sensing which supports field enhancement in the slot region for both quasi-TE and quasi-TM modes is done [43], [44]. The cross-slot waveguide is composed of both vertical and horizontal slot regions. This structure can be designed to connect via the tapered waveguides and can be fabricated on a SOI wafer with a $220\ nm$ top Si layer (or a thicker layer if necessary) on a $2\ \mu m$ or similar thick buried oxide (BOX) layer. After the cross-slot waveguide is formed, the several nm thick sensing layer for biochemical sensing can be added to all the surface of the silicon cores such as silanized with 3-glycidyloxy propyl trimethoxy saline [41] for label free protein sensing or dipped into aqueous glutaraldehyde for the study of label-free molecular binding reactions, as shown in Fig. 3.27. Here the thickness of sensing layer is taken as $5\ nm$.

Variations of confinement factors in the vertical, horizontal, and total slot regions for the E_x mode with the width of silicon cores, W are shown in Fig. 3.28. The silicon core height, H, the vertical slot width, W_S and the horizontal slot height, H_S are taken as $200, 100, and\ 100nm$, respectively. It can be observed that for the E_x mode, with the increase of the silicon core width, the confinement factor in the vertical slot region increases at first and then it decreases. Its maximum value is 29.7% when the silicon width is $190\ nm$. The confinement factor in the

horizontal slot region also increases at the beginning but asymptotically reaches its stable value when the silicon core width increases.
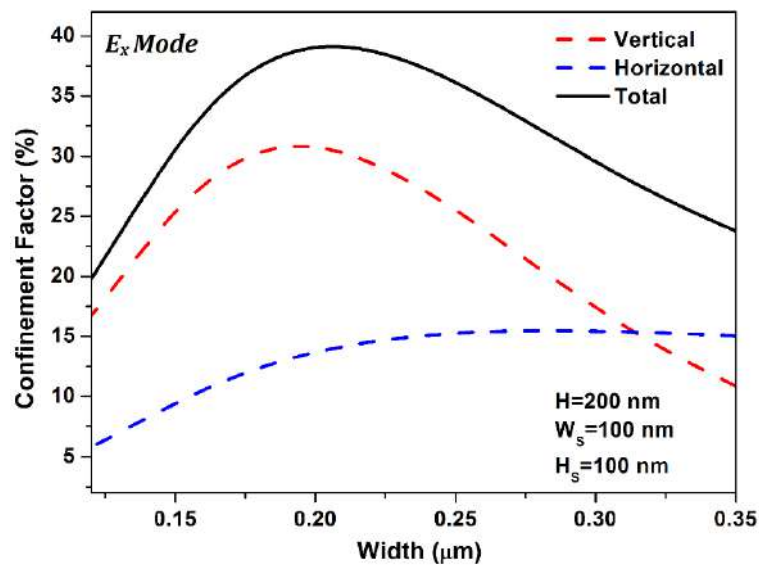
Figure 3.28: Variations of confinement factors in the vertical, horizontal, and total slot regions for the E_x mode with the width of silicon cores, w
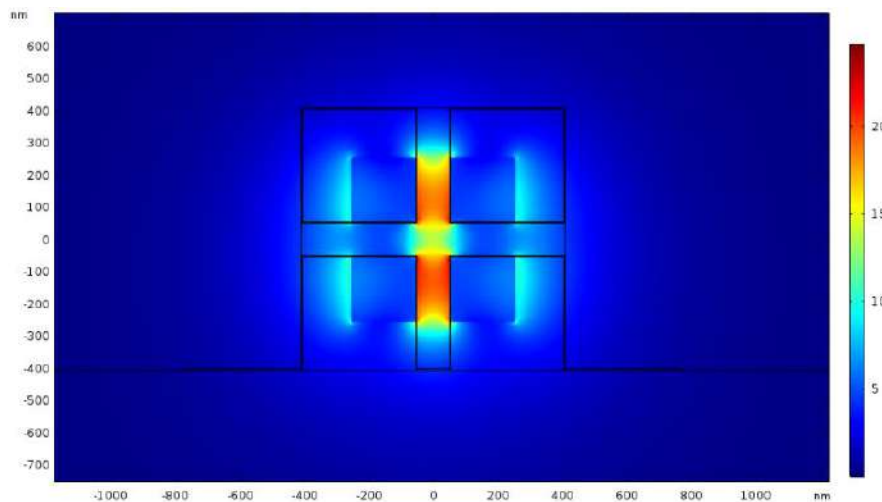
Figure 3.29: E_x field enhancement

For quasi-TE mode, as its dominant E_x field is enhanced in the vertical region, which is shown in Fig. 3.29, its vertical confinement is dominant here. Therefore, the maximum value of the confinement factor in the vertical slot region is much larger than that in the horizontal slot region. Variation of the confinement factor in the whole slot regions (total-slot confinement factor, Γ_{T-E_x}) with the silicon width has a similar tendency as the vertical slot but reaches its maximum value of 39.4%, when $W = 210\ nm$. Correspondingly, for the E_y mode, the maximum value of the confinement factor in the vertical slot region is much lower than that in

the horizontal slot region, for dominant E_y field of the quasi-TM mode (shown in Fig. 3.30) is enhanced in the horizontal region.
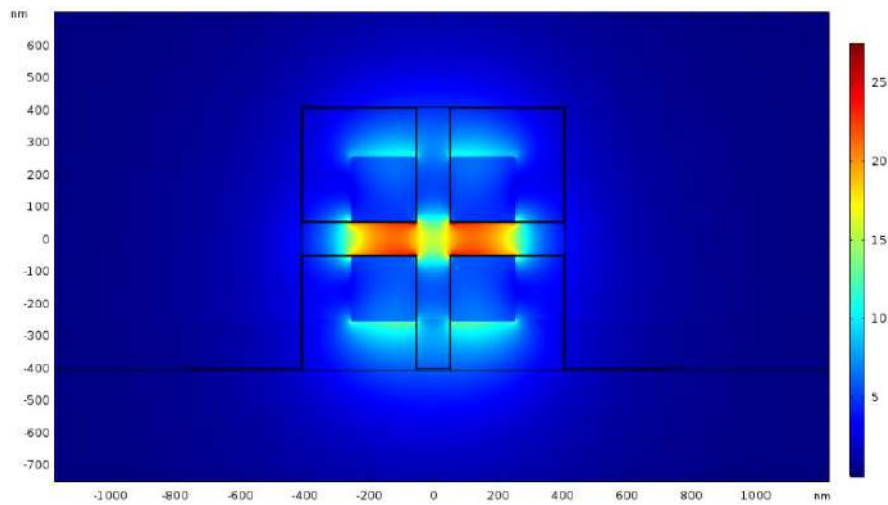
Figure 3.30: E_y field enhancement

Variations of total-slot confinement factors for the E_x mode, Γ_{T-E_x}, with the width of silicon cores, W for different silicon core heights are shown in Fig. 3.31 and 3.32 by colored lines. It can be observed that for the E_x mode, in all the cases, total-slot confinement factors increase at first and then decrease with the increase of the silicon core width, and they reach their peak values at different width values. It can be concluded that for the E_x mode, the value of the silicon width for the highest total-slot confinement factor decreases with the increase of the silicon core height. These curves also show that higher total confinement factor can be obtained by using larger height, H and smaller width, W.
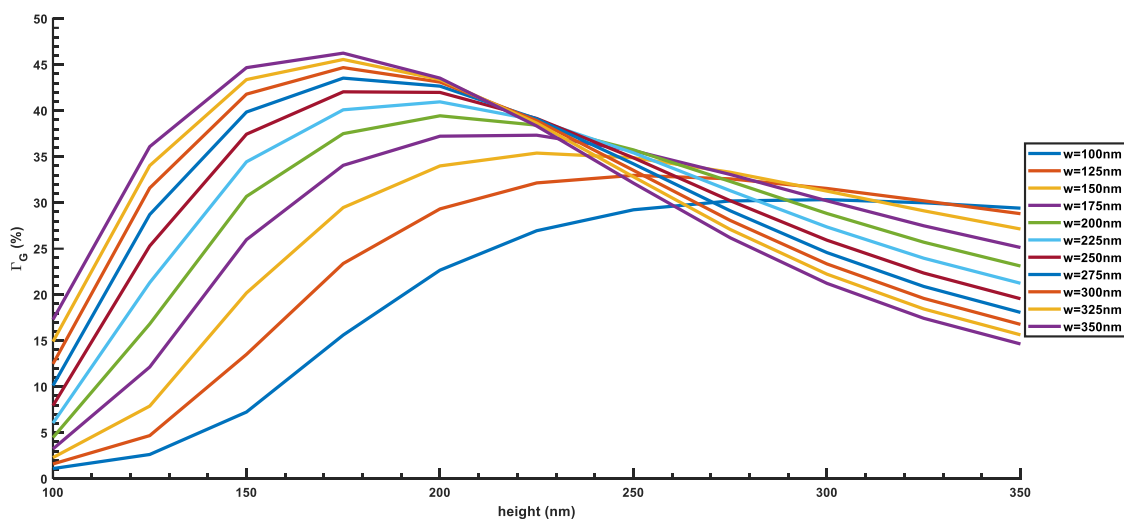
Figure 3.31: Variations of total-slot confinement factors with the silicon core width (TE mode)
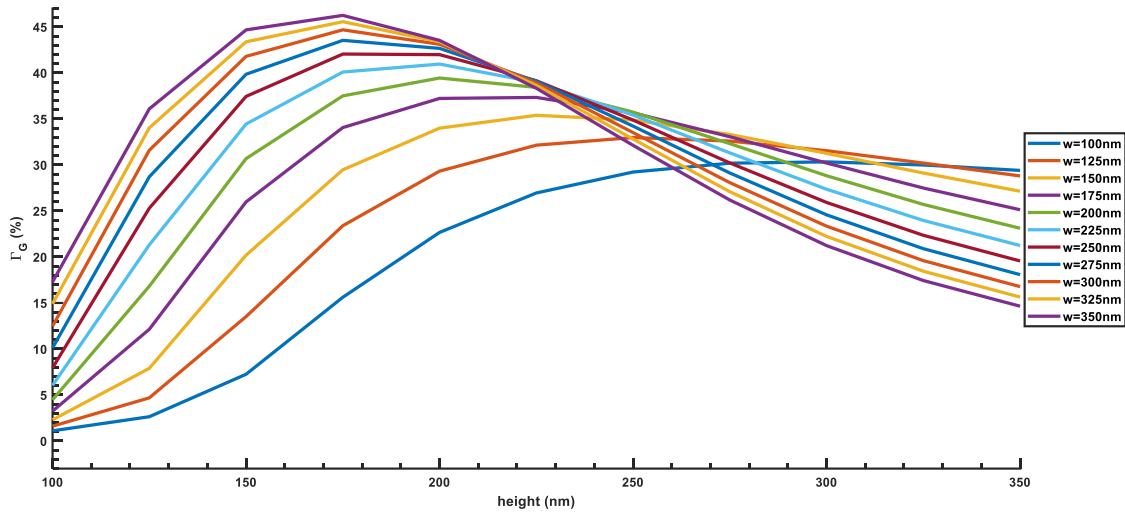
Figure 3.32: Variations of total-slot confinement factors with the silicon core width (TM mode)

Fig. 3.33 and 3.34 shows variations of Γ_{T-E_x} with the silicon core height, H for different silicon widths. It can be observed that in all cases, for the E_x mode, with the increase of the silicon core height, the total-slot confinement factors increase at first and then asymptotically reach their stable values. Variations of total-slot confinement factors for the E_y mode, Γ_{T-E_y}, with the height of silicon cores for different widths are shown by colored lines.
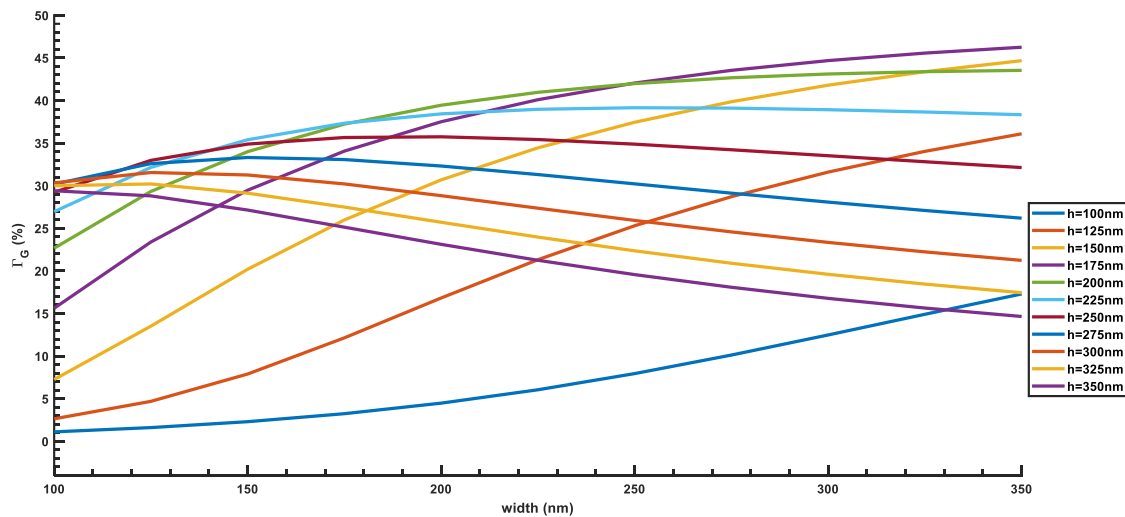
Figure 3.33: Variations of total-slot confinement factors with the silicon core height (TE mode)

It can be observed that in all the cases for the E_y mode, the total-slot confinement factors increase first and then decrease with the increase of the silicon core height. The value of silicon height for the highest total-slot confinement factor decreases with the increase in the silicon core height, like the variation of total-slot confinement factor with the silicon core width for the E_x mode. Variations of total-slot confinement factors for the E_y mode with the width of

silicon cores also have the similar tendencies as those of the total-slot confinement factors for the E_x mode with the height of silicon cores.
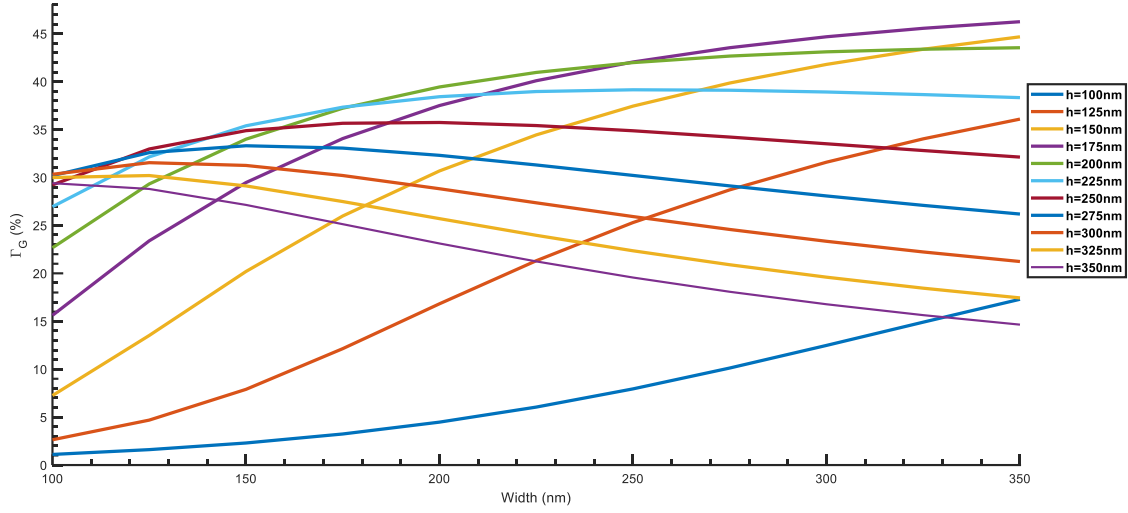
Figure 3.34: Variations of total-slot confinement factors with the silicon core height (TM mode)

To make the comparison of the confinement factors in the total slot region between the cross and the vertical or horizontal slot waveguides more reasonable, the height of the cross and vertical slot waveguides should be set to the same value, or the width of the cross and horizontal slot waveguides should be set to the same value. For the vertical or horizontal slot waveguide, the waveguide height or width equals its silicon height or width.

However, for the cross-slot waveguide, its waveguide width and height are taken as the summation of two silicon core and a vertical slot width, and the summation of two silicon core and a horizontal slot height, respectively. The maximum Γ_{T-E_x} in the slot region of the cross-slot waveguide is slightly less than that in the vertical slot waveguide, for instance, the maximum confinement factors are 39.4% and 40.9% in the slot regions of the cross and vertical slot waveguides with the same waveguide height of $500\ nm$. Correspondingly, the maximum Γ_{T-E_y} in the slot region of the cross-slot waveguide nearly equals to that of the horizontal slot waveguide with the same waveguide width. As shown in Fig. 3.35, for the E_x mode, with an increase in the silicon core height, the total-slot confinement factor may keep increasing by reducing the silicon core width continuously. Similarly, for the E_y mode, with the increase of the silicon core width, the total-slot confinement factor may keep increasing by reducing the silicon core height continuously. Next, summation of the total-slot confinement factors for the E_x and E_y modes, $\Gamma_{T-E_x} + \Gamma_{T-E_y}$ is taken as the optimization parameter to design a cross-slot waveguide with the highest sensitivity for its polarization independent operation.

Variations of $\Gamma_{T-E_x} + \Gamma_{T-E_y}$ with the width, W of silicon cores is shown in Fig. 3.35. It can be observed that for a given silicon core height, with the increase of width, their summation increases at first and then decreases. It can also be observed when the width and height of the silicon cores are set to around 205 and 220 nm, respectively, the $\Gamma_{T-E_x} + \Gamma_{T-E_y}$ is as high as 79%, nearly the same as the summation of the maximum Γ_G for the E_x mode in the vertical slot waveguide with similar waveguide height and the maximum Γ_G for the E_y mode in the horizontal slot waveguide with similar waveguide width. The structure is not sensitive to the fluctuation of the dimension, allowing more than $\pm 10 \; nm$ possible fabrication tolerances in both the width and the height.
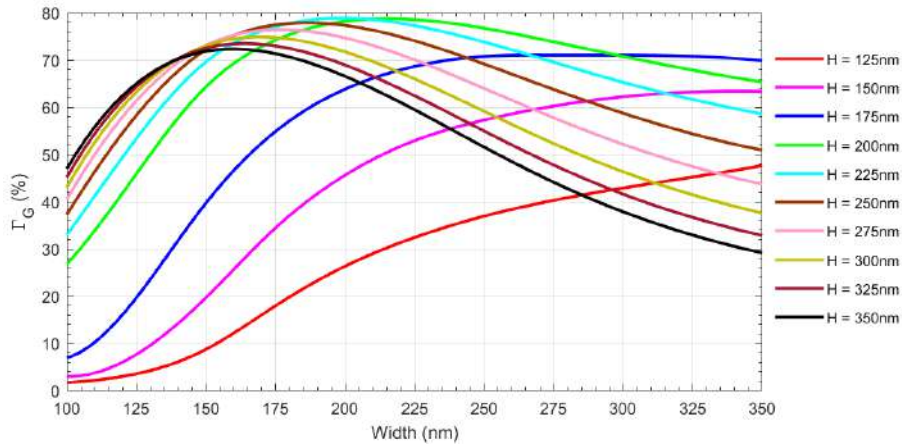
Figure 3.35: Variations of $\Gamma_{T-E_x} + \Gamma_{T-E_y}$ with the width, w

For a polarization-independent structure which can support quasi-TE and quasi-TM modes with similar performance, besides the total-slot confinement factor, ratio of the total-slot confinement factors for the E_x and E_y modes, $\Gamma_{T-E_x}/\Gamma_{T-E_y}$, should also be calculated to optimize the cross-slot dimensions. Variations of $\Gamma_{T-E_x}/\Gamma_{T-E_y}$ with the width, W and height, H of silicon cores are shown in Fig. 3.13 and 3.14, respectively. The ratio of 1 is shown here by a black dashed line. It can be observed from Fig. 3.36 that for a given height, due to the parabolic variation tendency of Γ_{T-E_x} and the monotone-increasing variation tendency of Γ_{T-E_y} with the silicon core width, all the ratios increase at first and then decrease with the increase of the silicone core width. The red curve for $H = 250 \; nm$ shows that the cross-slot waveguide can confine equal power in the whole slot region for both the polarizations, but total-slot confinement factor for each one is around 34%. On the other hand, for $H = 220 \; nm$, shown by a green line, total-slot confinement factor for each polarization can reach to the same value

of 39.3%, when the silicon core width is taken as $212\ nm$. On the other hand, for a given width, the confinement ratios decrease at first and then increase with the increase of the silicon core height, as shown in Fig. 3.37. It is obvious that the ratio can reach 1 at several width and height combinations.
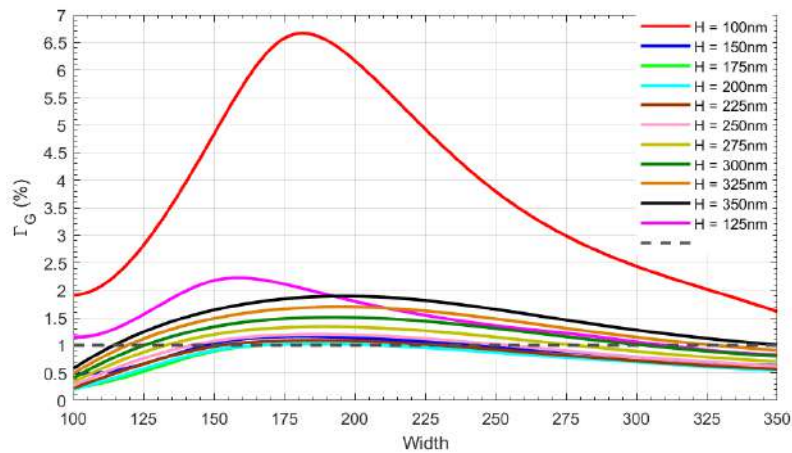
Figure 3.36: Variations of $\Gamma_{T-E_x}/\Gamma_{T-E_y}$ with the width, w
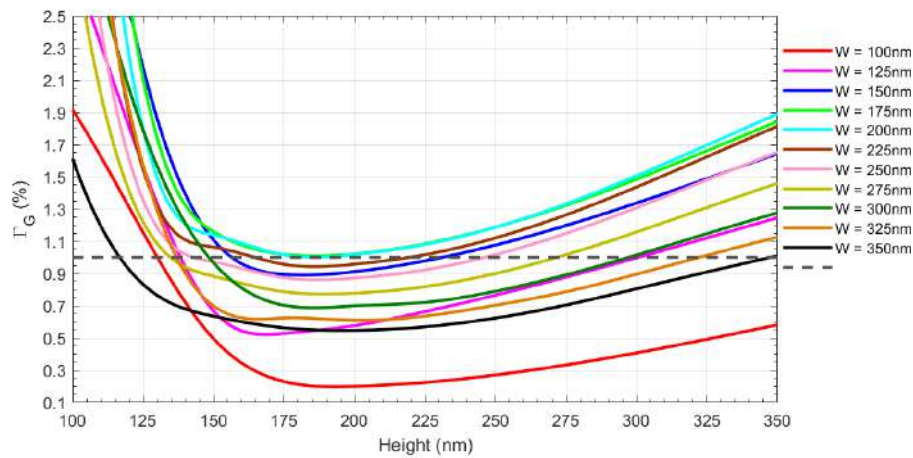
Figure 3.37: Variations of $\Gamma_{T-E_x}/\Gamma_{T-E_y}$ with the height, H

To achieve a successful polarization independent design, the sensitivities for the E_x and E_y modes should be not only nearly the same but also large enough, so the width and height of the silicon cores are optimized to be around 223 and $216\ nm$, with the total-slot confinement factor for each polarization of 39.4%.

Chapter 4

METAL ASSISTED CROSS SLOT WAVEGUIDE

In an optical silicon-on-insulator waveguide sensor for chemical and biochemical analysis, the effective index is affected by either the change in the refractive index of the cladding medium, known as homogeneous sensing, or the change in the thickness of an ultra-thin layer of receptor molecules immobilized on the waveguide surface, known as surface sensing. Various integrated optical structures have been proposed to measure the change in the effective index, such as directional couplers, interferometers, and micro ring resonators [25], [45]–[47]. However, the sensitivity of these devices is limited due to the confinement of light to the core region of the waveguide, which restricts light interaction with the sensing material in the cladding region or at the surface of the nanowire.

The unique feature of a slot waveguide, where light is guided in a low index region, allows for easy access of the sensing layer to high field regions, potentially improving the sensitivity of the sensor. The guidance property in a slot waveguide is due to the continuity of the normal component of the Electric Flux Density in the low index region. There are two types of slot waveguides, vertical and horizontal, which are distinguished by their structural orientation and Electrical field enhancement. Unfortunately, both the horizontal and vertical slot guides confine only one specific polarization, limiting their usefulness in sensing applications. However, recent research has shown that combining a vertical and a horizontal slot can lead to the design and optimization of a silicon-on-insulator cross-slot waveguide for biochemical sensing, which can support both polarized waves simultaneously. The high index contrasts necessary to enhance the power in the slot region results in an optical mode that is hybrid in nature.

Among other various waveguides, nanoscale optical waveguides based on surface plasmon polaritons (SPP) have gained attention due to their strong localization in the nanoscale region. Several types of SPP-based waveguides have been reported, including metal-insulator-metal (MIM) waveguides, dielectric-loaded SPP waveguides, and hybrid plasmonic waveguides (HPWs). HPWs achieve sub-wavelength confinement and can reduce propagation loss [36]–[38]. The TM mode has been widely used in SPP-based waveguides as it is required to excite the SPP mode. However, recent studies have demonstrated the advantages of using the TE

mode in polymer based SPP waveguides, particularly in realizing sharp bends and achieving small bending with long propagation length. The TE mode, also known as the metal-assisted photonic mode, has a longer propagation length compared to the TM mode, despite having a larger distribution of fields.

Based on these findings, we propose a novel structure of a metal-assisted silicon cross-slot waveguide with potential applications in a wide range of areas including medical diagnostics, environmental monitoring, and food safety testing, and highly sensitive gas detection. Our structure involves inserting a metal layer beside the silicon cross-slot to suppress light confinement in the slot region, resulting in strong light confinement.

4.1. Structure of the Proposed Sensor
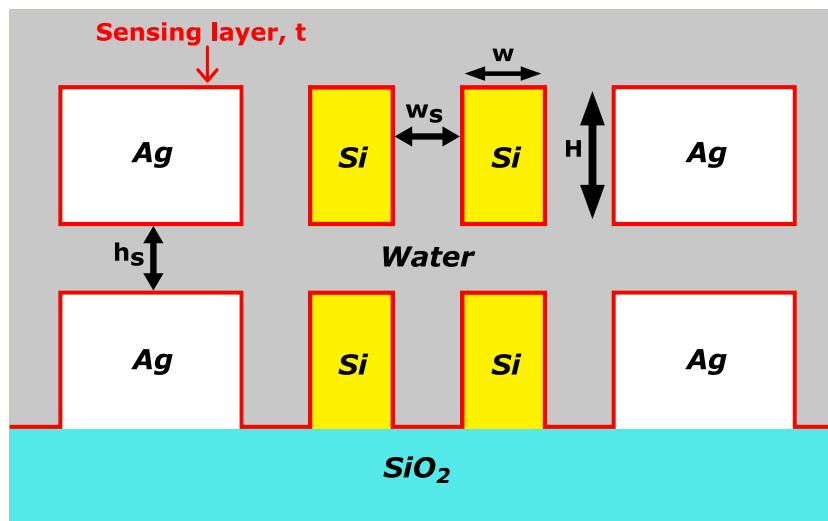
Figure 4.1: Si Cross-slot waveguide with Ag layer

Fig. 4.1 displays a metal-assisted silicon cross-slot waveguide, which is a structure that can be used as a sensor. The sensor is built on top of a thin layer of SiO_2 substrate. The waveguide is covered by a thin sensing layer with a refractive index value of 1.45. The refractive indices of the materials used in the sensor structure are as follows: the silicon core has a refractive index of 3.47548, the SiO_2 substrate has a refractive index of 1.44402, the aqueous solution has a refractive index of 1.33, and the silver layer has a complex refractive index of $0.1453 -$ j11.3587. The dimensions of the waveguide are specified by the Si-width (w), slot width (w_s), and waveguide height (h). The thickness of the SiO_2 layer is denoted as t. The simulations that were conducted to study the behavior of the waveguide were done at a wavelength of 1550 nm.

In summary, the Fig. 4.1 represents a metal-assisted silicon cross-slot waveguide sensor that is built on a SiO_2 substrate and covered with a thin sensing layer with a refractive index of 1.45. The materials used in the sensor have specific refractive indices, and the dimensions of the waveguide are defined by the Si-width, slot width, waveguide height, and thickness of the SiO_2 layer. The simulations were conducted at a wavelength of 1550 nm.

4.2. Results and Discussions

The width and height of the silicon cores are taken to be around 223 and 216 nm. It can be observed that confinement factors in the slot region, Γ_G for TE polarizations depend on the width of Ag core and silicon core. The less silicon core width and the more Ag core width, the more is the confinement factor, Γ_G. The Γ_G for the E_x mode reach its maximum value of 57% when the silicon core width is 150 nm and Ag core width is $350nm$. Again, for TM mode, Γ_G increases as the Ag width increases and when W is $150nm$, but for other values of silver and silicon core widths, Γ_G increases first but remains fixed at a value. Variations of Γ_G for the E_x and E_y modes with the silicon core height, H, Ag and silicon core width of a metal assisted cross-slot waveguide are shown in Fig. 3.16 and Fig. 3.17 by colored lines. Heights of the silicon core and slot are taken as 223 and 100 nm, respectively.

For quasi-TE mode, as its dominant E_x field is enhanced in the vertical region, which is shown in Fig. 4.2, its vertical confinement is dominant here. Therefore, the maximum value of the confinement factor in the vertical slot region is much larger than that in the horizontal slot region.

Correspondingly, the maximum value of the confinement factor in the vertical slot region is much lower than that in the horizontal slot region, for dominant E_y field of the quasi-TM mode (shown in Fig. 4.3) is enhanced in the horizontal region.

Variations of confinement factors in the total slot regions for both TE and TM mode with the height of silicon cores, H are shown in Fig. 4.4. The silicon core width, W, the vertical slot width, W_S and the horizontal slot height, H_S are taken as $216, 100$ and $100nm$, respectively. For TM mode confinement factor, Γ_G increases first with the increase of height up to $175nm$ with a confinement factor of 68%. After that, the confinement factor, Γ_G decreases sharply. Again, for TE mode, confinement factor, Γ_G increases up to a height of $220nm$, then it decreases slightly up to $480nm$. But it decreases very sharply beyond that limit.
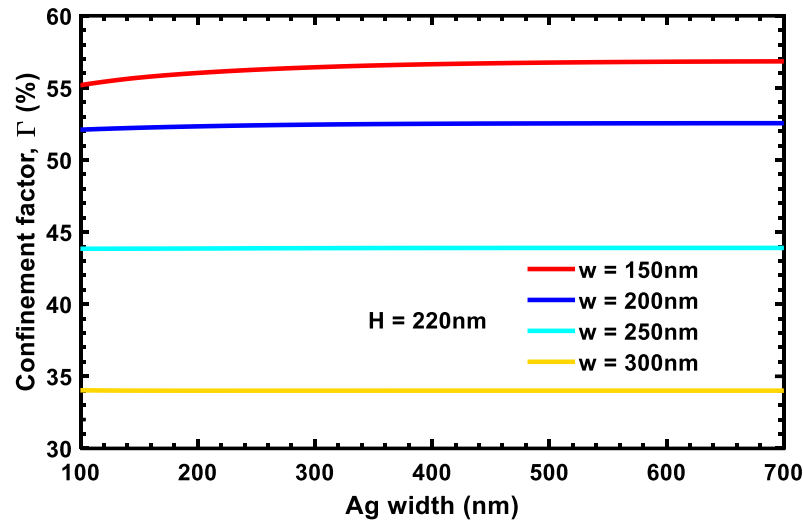
Figure 4.2: Variation with width (TE mode)
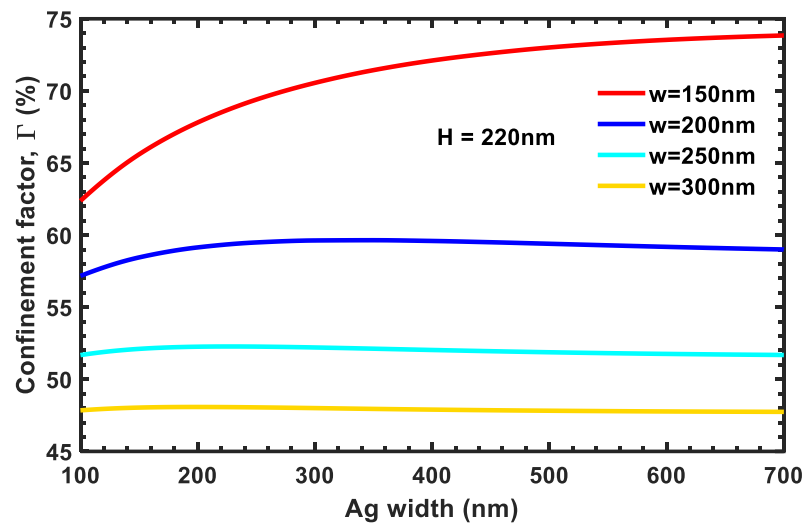
Figure 4.3: Variation with width (TM mode)

From Fig. 4.2 and 4.3, the confinement factor increases with the increment of silver width for both TE and TM mode. Increasing the length of silver can increase the amount of light that propagates through the silver, which can result in higher absorption and a higher extinction coefficient. This, in turn, can increase the amount of light that is confined within the slot region, leading to a higher mode confinement.

From Fig. 4.4 there is a rapid decline of the confinement factor for the TE mode. It is because of the TE and TM mode coupling at the particular height. Mode coupling occurs when energy from one mode is transferred to another mode, leading to changes in the propagation characteristics of both modes.
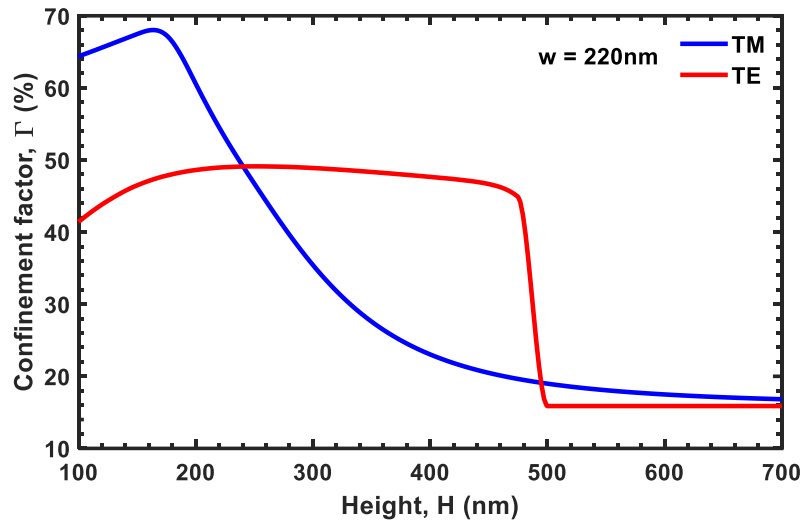
Figure 4.4: Variation of Confinement Factor with height.
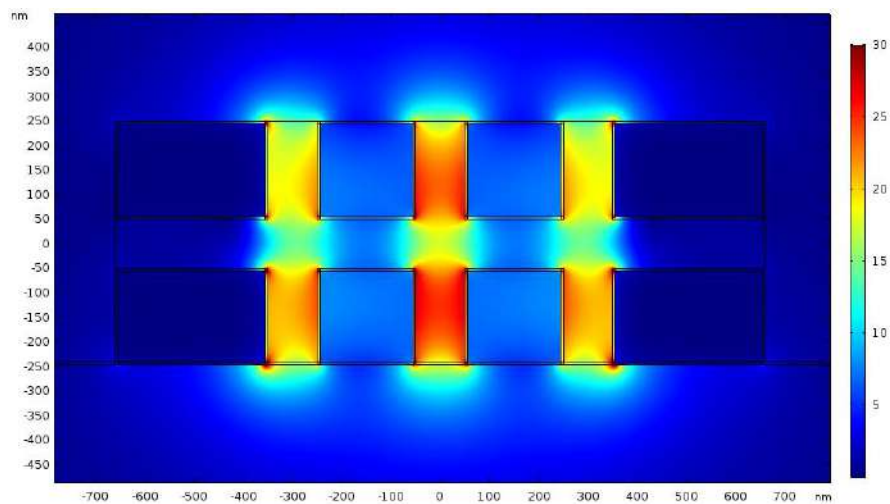
Figure 4.5: E_x field enhancement for TE mode.

Now, final optimization will be carried out based on previously simulated information. Before final optimization the following key factors must be addressed:

a) The confinement factor for TE and TM polarization must be equal so that the design becomes polarization independent.

b) The sensitivity must be as high as possible.

In Fig. 4.5 and 4.6, silicon width, silver width, height and confinement factor of both polarizations has been demonstrated. It is a big challenge to optimize four parameters with high accuracy as there are many parameters involved.
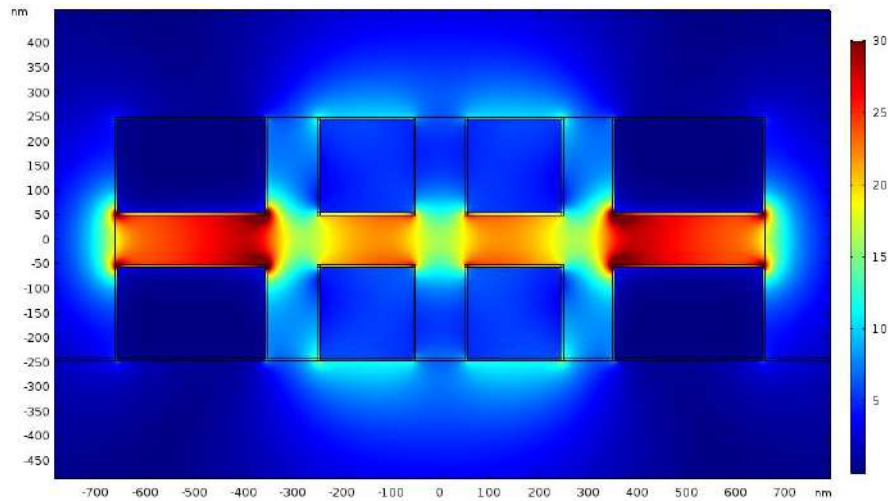
Figure 4.6: E_y field enhancement for TM mode.
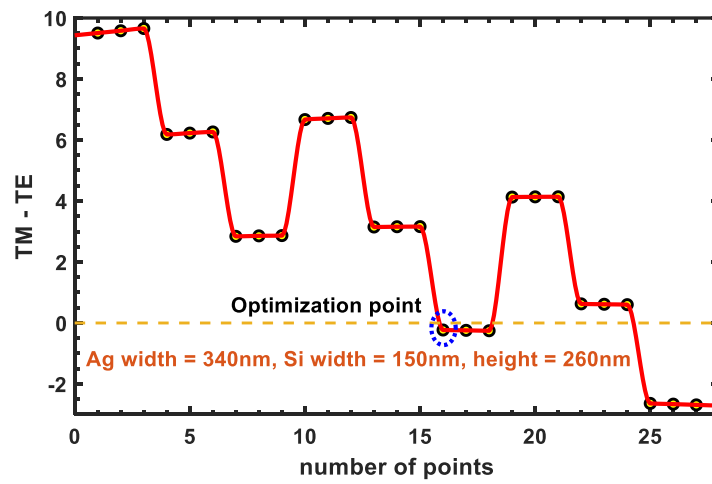
Figure 4.7: Optimization of TE and TM mode with Ag width = 340nm, Si width = 150nm, height=260nm
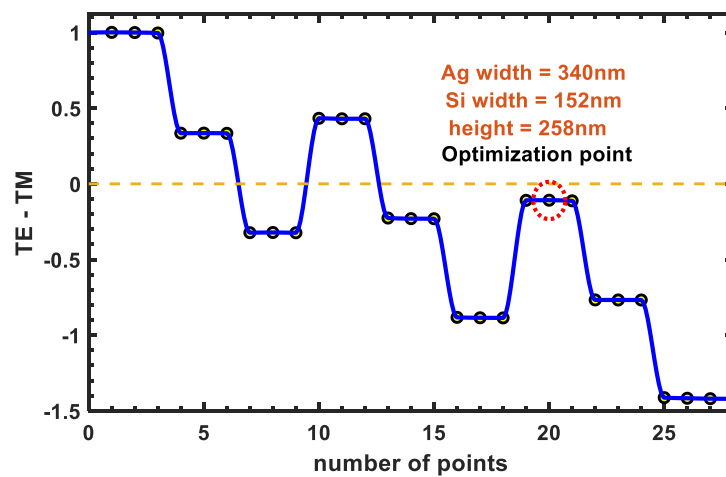
Figure 4.8: Optimization of TE and TM mode with Ag width = 340nm, Si width = 150nm, height=258nm
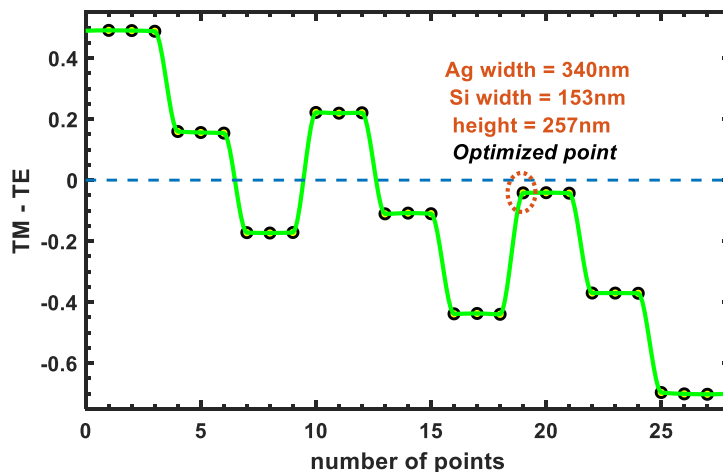
Figure 4.9: Optimization of TE and TM mode with Ag width = 340nm, Si width = 153nm, height=257nm

To overcome this, a very basic approach is taken. First, for a wide range of width and height of TE and TM mode, confinement factor is calculated. The height ranges from 150nm to 250nm, silicon width ranges from 150nm to 250nm and silver width range is 150nm to 350nm. Then, the difference of confinement factor of two polarization modes is made. For the lowest mismatch of 3.2%, the next optimization is carried out. A new optimization point is found around 150nm silicon width, 260nm height and 340nm silver width. A new range of width and height around the optimization point is taken for simulation, but the deviation of maximum and minimum height and width is kept small. For fine tuning new ranges of height, silver width and silicon width are 258nm to 262nm, 338nm to 342nm and 148nm to 152nm respectively. TE and TM polarization mismatch is found to be 0.23% for a height of 258nm, Si width of 152nm and Ag width of 340nm. Following the same procedure and keeping the difference windows of height and width very narrow (silver width 151 to 153nm, silicon width 339 to 341nm, height 257 to 259nm), the final solution is found with just a mismatch of 0.04%. The optimized height, silver width and silicon width are 257nm, 340nm and 153nm respectively. The results are displayed in Fig. 4.7 to 4.9.

In Figures 4.10 to 4.11 silicon width is varied from $150nm$ to $250nm$. The width and height of the silicon core is kept fixed at $350nm$ and $200nm$ respectively. For TE and TM mode confinement factor increases gradually with the increase of width and refractive index. For TE and TM modes, the electric and magnetic fields are predominantly confined within the dielectric layer, with a relatively small field component extending into the metal layers. Increasing the width of the metal layers can enhance the confinement of the electric field within the dielectric layer, because the metal layers can act as mirrors to reflect the electric field back

into the dielectric layer, reducing the amount of field that extends into the metal layers. For TM modes, a wider metal layer can provide a stronger screening effect to confine the magnetic field within the metal layers. As a result, the confinement factor for TE and TM modes increases with increasing metal layer width.
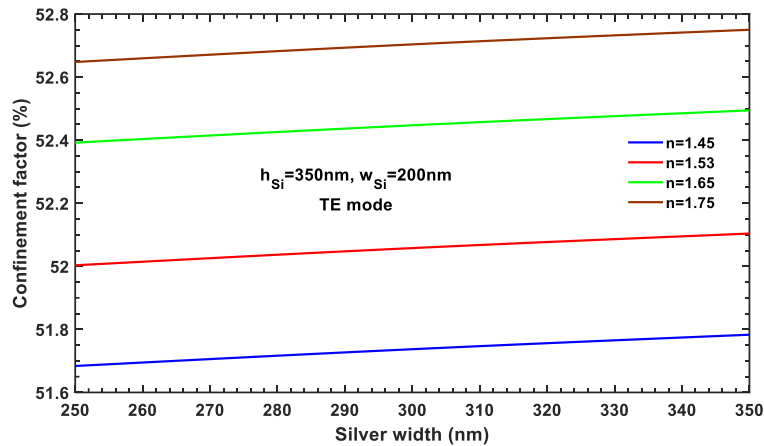
Figure 4.10: Confinement factor with the variation of Ag width for TE mode
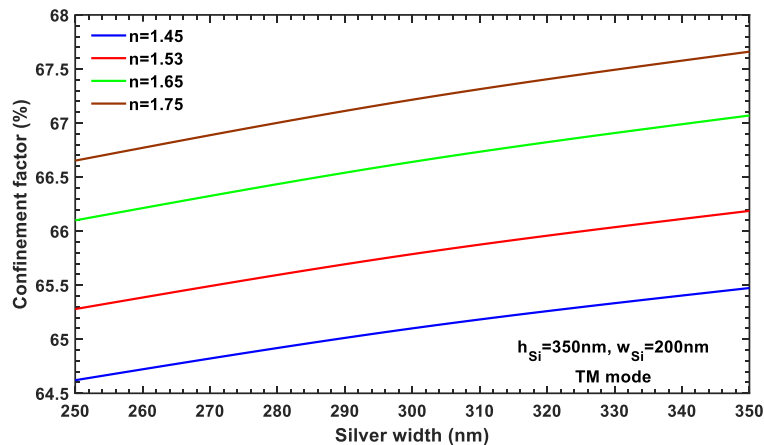
Figure 4.11: Confinement factor with the variation of Ag width for TM mode

In Figures 4.12 to 4.13 silicon height is varied from $150nm$ to $250nm$. The width of silver and silicon core is kept fixed at $350nm$ and $200nm$ respectively. For TE mode confinement factor increases gradually with the increase of height. But for TM mode confinement factor decreases with the increment.
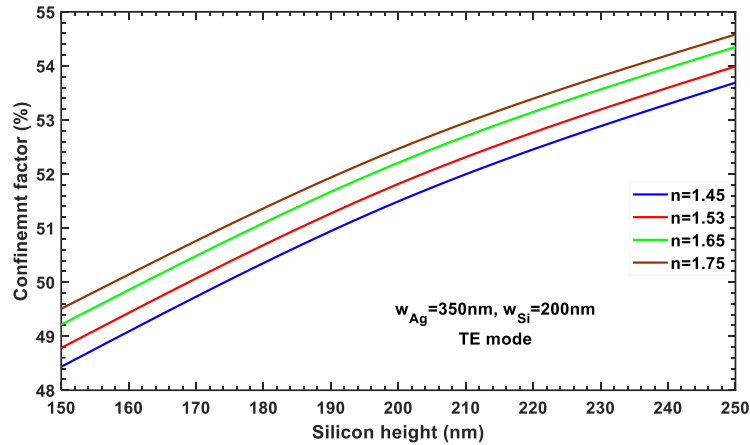
Figure 4.12: Confinement factor with the variation of Si height for TE mode for different indexes
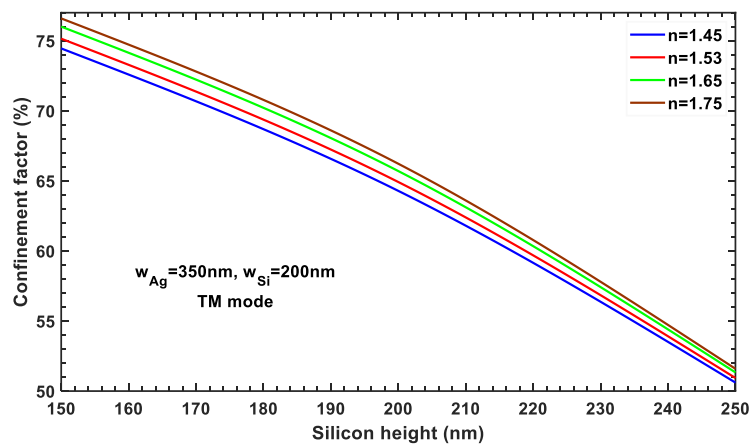
Figure 4.13: Confinement factor with the variation of Si height for TM mode for different index

For TE modes, the electric field is predominantly confined to the region of highest refractive index, which is the core in the case of a waveguide. Increasing the height of the waveguide can lead to a stronger confinement of the electric field within the core region. This is because a higher waveguide height allows for a greater difference in refractive index between the core and cladding regions, which leads to a stronger guidance of the electric field within the core. For TM modes, the magnetic field is predominantly confined to the region of lowest refractive index, which is the cladding in the case of a waveguide. Increasing the height of the waveguide can lead to a weaker confinement of the magnetic field within the core region. This is because a higher waveguide height results in a smaller difference in refractive index between the core and cladding regions, which leads to a weaker guidance of the magnetic field within the core.

For TE and TM modes, the confinement factor decreases as the width of the waveguide increases because the electric and magnetic field is primarily confined to the core region and

has little penetration into the cladding region. As the width of the waveguide increases, there is more room for the fields to spread out and leak into the cladding region, resulting in a lower confinement factor. As the refractive index of the core material increases relative to the cladding material, the mode becomes more tightly confined, and the confinement factor increases.

Figure 4.14: Confinement factor with the variation of Si width for TE mode for different index.
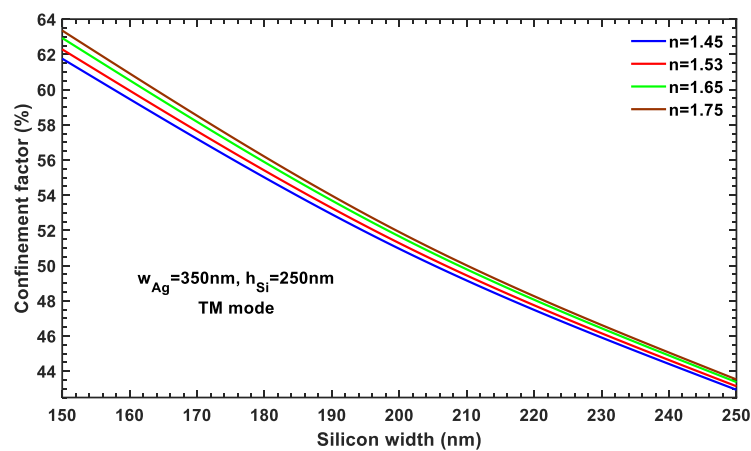
Figure 4.15: Confinement factor with the variation of Si width for TM mode for different index.

After finding the optimized dimension for the refractive index of 1.45, the same process is carried out for other refractive indices. In Fig. 4.14 and 4.15 the silver width is varied from $250nm$ to $350nm$ keeping core height of $350nm$ and doped Si width of $200nm$. In both TE and TM mode cases, confinement factor increases with the increase of refractive index. For TE mode confinement factor increment is slow compared to TM mode.

In the following table the optimization results for different refractive indexes and the difference between TE and TM mode have been stated. It can be seen that the design is very optimized for a wide range of refractive indexes with a high degree of polarization independence.

Table 4-1: Optimization results for different refractive index

Refractive index	TE mode Confinement factor	TM mode Confinement factor	Difference
1.45	59.3166	59.2780	0.0386
1.53	59.7721	59.7486	0.0235
1.65	60.3207	60.3208	-0.0001
1.75	60.6859	60.6941	-0.0082

4.3. Cross-slot Waveguide with Highly Doped Silicon

In this section the design will be viewed from a different angle. Instead of Ag layer around the Si layer, a highly doped Si layer will be used. The main contribution is the use of highly doped silicon instead of metals to form the hybrid plasmonic waveguide. The real part of the complex relative permittivity of the highly doped p-silicon approaches a negative value and therefore exhibits metal-like properties. Utilizing highly doped p-silicon instead of metal enables our proposed polarizer to be fabricated using the CMOS process.
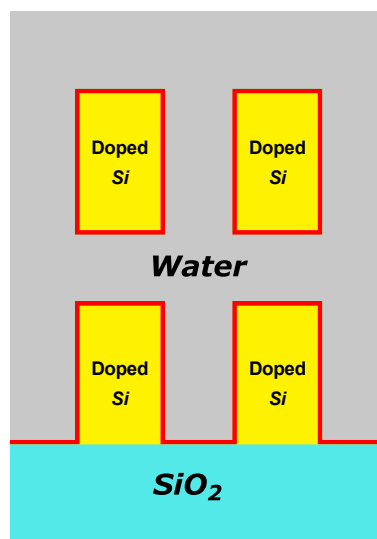
Figure 4.16: Cross-slot waveguide with highly doped silicon

In this section, the regular slot waveguide element Si has been replaced with highly doped silicon. The structure of a slot waveguide for biochemical sensing is shown on Fig. 4.16. The waveguide is completely covered with a thin sensing layer with a refractive index value of

1.45. Refractive indices of SiO_2 substrate, and the aqueous solution are taken as 3.47548, 1.44402, and 1.33, respectively. Initially, the sensing layer thickness and the slot width, are taken as 5 and 100 nm, respectively. The refractive index of the doped silicon depends on the doping concentration.

For this work, in optimizing the dimension of the silicon cores, Γ_G is taken as the optimization parameter. It can be observed that confinement factors in the slot region, Γ_G for both the polarizations increase with the increase of the silicon core height. The Γ_G for the E_x and E_y mode reach 74% at its intersection point when the width is 280 nm. Widths of the silicon core and slot are taken as 200 and 100 nm, respectively and the doping concentration of $P-type\ Si$ is kept at $10^{22}\ cm^{-3}$.

Figure 4.17: Confinement factor with the variation of height (h) for TE and TM mode.

Variations of Γ_G for the E_x and E_y modes with the silicon core width of a cross-slot waveguide are shown in Fig. 4.17 and 4.18 by red and blue lines, respectively. The height of the silicon cores is taken as 200 and the doping concentration remains at $10^{22}\ cm^{-3}$. It is shown here that with the increase in width, Γ_G for the E_x and E_y mode increases rapidly. Two curves meet at a confinement factor of 72% at a width of $226nm$. In Fig. 4.19 the height and width of the Si core is kept at $200nm$ while changing the concentration of doping from $1 \times 10^{22}\ cm^{-3}$ to $5 \times 10^{22}\ cm^{-3}$. There is an exponential decrease in confinement factor for both TE and TM modes. Though TE mode has a higher magnitude of confinement factor.
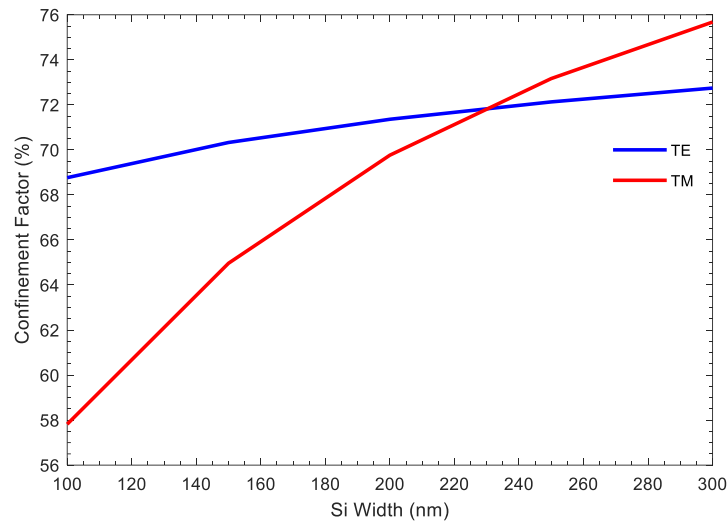
Figure 4.18: Confinement factor with the variation of Si width (w) for TE and TM mode.

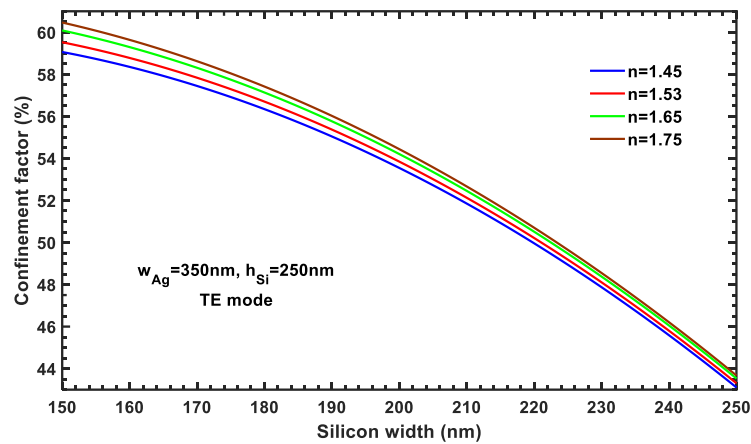*Figure 4.19: Confinement factor with the variation of doped Si concentration for TE and TM mode.*

In the case of a highly doped silicon slot waveguide, the confinement factor increases with an increase in height and width. This is because increasing the height and width of the waveguide increases the effective refractive index of the waveguide, which in turn increases the confinement of the optical mode within the waveguide core.

On the other hand, the confinement factor decreases with an increase in doping concentration. This is because increasing the doping concentration of the waveguide material reduces the effective refractive index contrast between the waveguide core and cladding, leading to a decrease in the confinement of the optical mode within the waveguide core. Additionally,

increasing doping concentration can increase the absorption loss of the waveguide, which further reduces the confinement factor.

In this section, the previous design will be modified. Previously we added a silver barrier around silicon slots. Now doped silicon layer will replace the Ag layers around the silicon slots (Fig. 4.20). The waveguide is completely covered with a thin sensing layer with a refractive index value of 1.45. Refractive indices of SiO_2 substrate, and the aqueous solution are taken as 3.47548, 1.44402, and 1.33, respectively. Initially, the sensing layer thickness and the slot width, are taken as 5 and 100 nm, respectively. The refractive index of the doped silicon depends on the doping concentration.
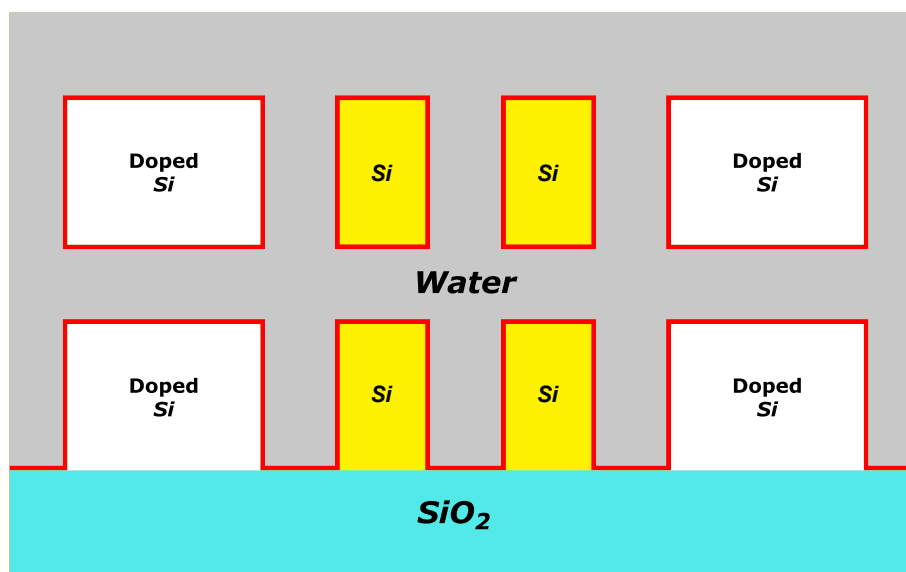
Figure 4.20: Conventional cross-slot waveguide with highly doped Si.
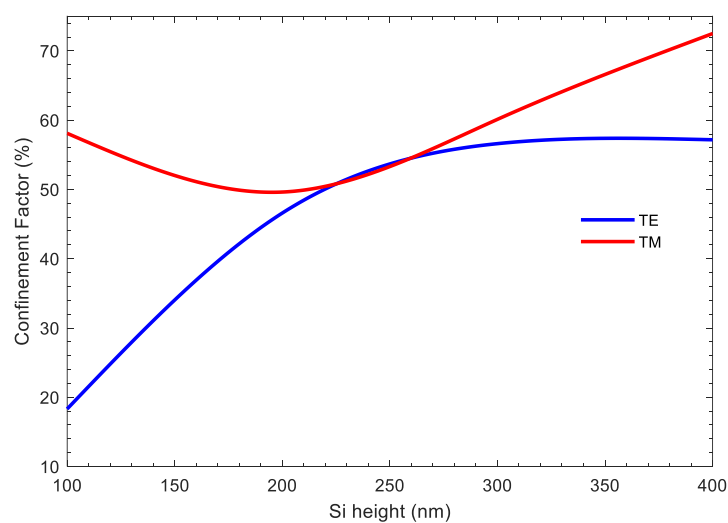
Figure 4.21: Confinement factor with the variation of height (h) for TE and TM mode.

It can be observed in Fig. 4.21 that confinement factors in the slot region, Γ_G for TE polarization increases first then decreases with the increase of the silicon core height. But Γ_G for TM polarization behaves in the opposite way. The Γ_G for the E_x and E_y mode reach 55% at its intersection points when the width is around 250 nm. Widths of the doped silicon cores and slot are taken as 200 and 100 nm, respectively and the doping concentration of $P - type\ Si$ is kept at $10^{22}\ cm^{-3}$.
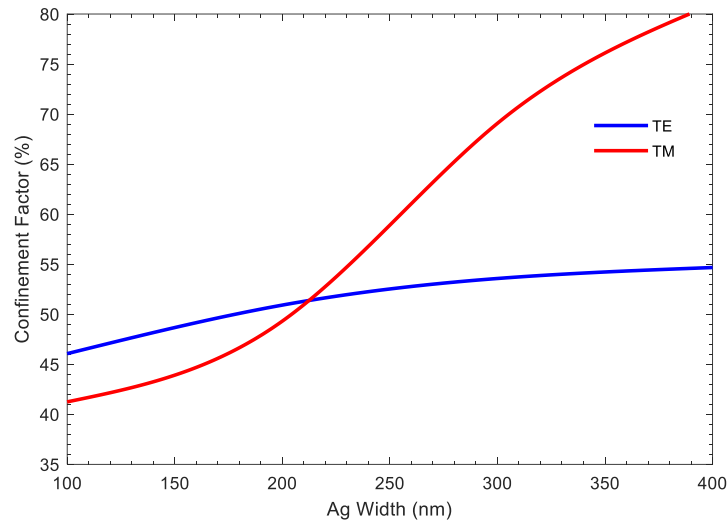
Figure 4.22: Confinement factor with the variation of width (w) for TE and TM mode.
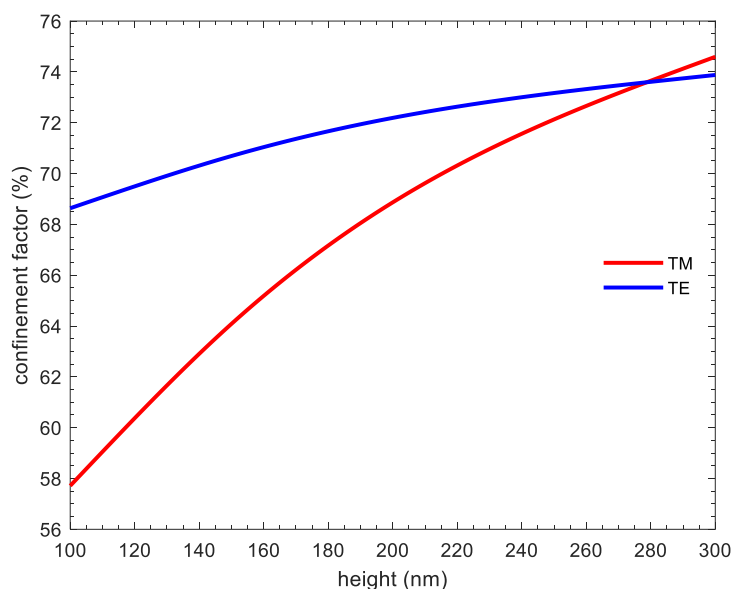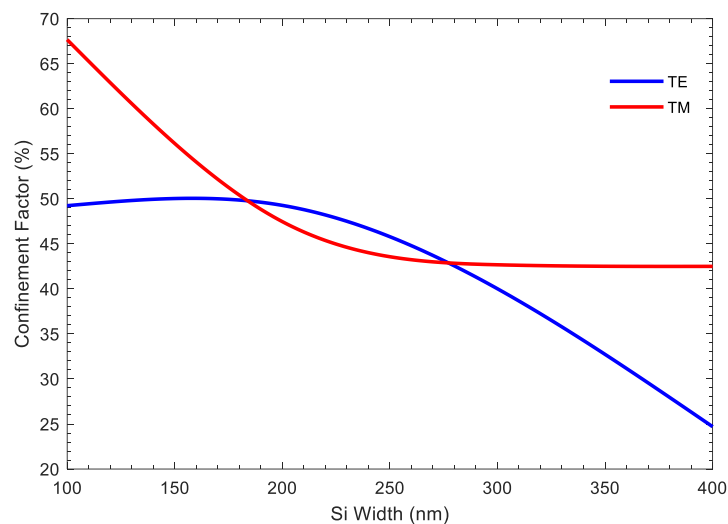

Figure 4.23: Confinement factor with the variation of Si width (w) for TE and TM mode.

Variations of Γ_G for the E_x and E_y modes with the silicon core width of a cross-slot waveguide are shown in Fig. 4.22 by red and blue lines, respectively. Height of the silicon cores and slot width are taken as 200 and 100 nm, respectively and the doping concentration remains at

$10^{22} \, cm^{-3}$. It is shown here that with the increase in width, Γ_G for the E_y mode increases faster than E_x mode. Two curves meet at a confinement factor of 50% at a width of $216 \, nm$.

Fig. 4.23 demonstrates the confinement factor curves for TE and TM modes for a varying Si width. The curve for TE mode slowly increases then decreases. But the TM curve decreases first then increases. The curves meet at two different points with different Γ_G and Si width. In Fig. 4.24 the height and width of the Si cores are kept at $200nm$ while changing the concentration of doping from $1 \times 10^{22} \, cm^{-3}$ to $5 \times 10^{22} \, cm^{-3}$. There is a rapid increase in confinement factor for TM mode. Though TE mode confinement factor remains flat.

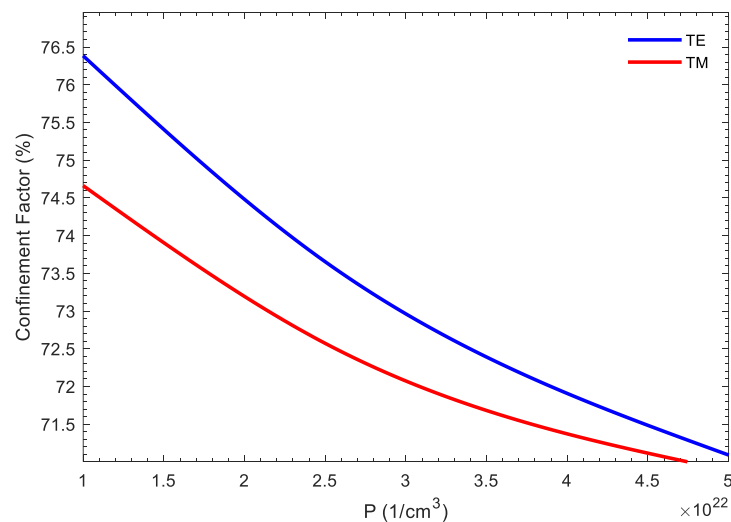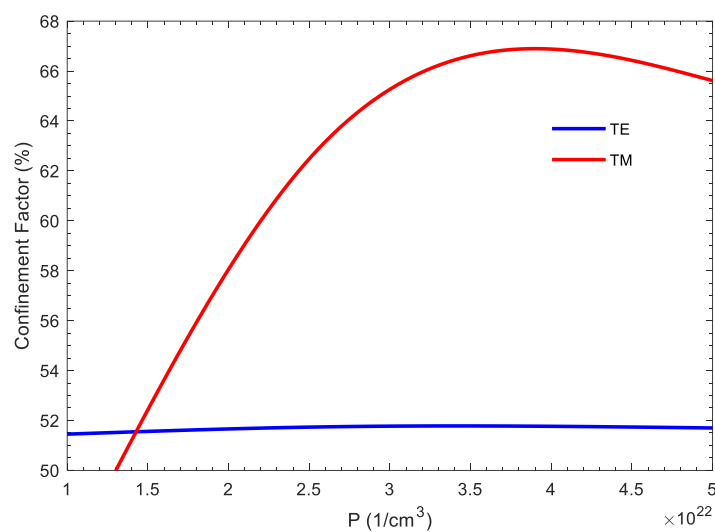*Figure 4.24: Confinement factor with the variation of doped Si concentration for TE and TM mode.*

In the case of a highly doped silicon slot waveguide, the confinement factor increases normally with an increase in height and width. This is because increasing the height and width of the waveguide increases the effective refractive index of the waveguide, which in turn increases the confinement of the optical mode within the waveguide core. On the other hand, the confinement factor decreases with an increase in doping concentration. This is because increasing the doping concentration of the waveguide material reduces the effective refractive index contrast between the waveguide core and cladding, leading to a decrease in the confinement of the optical mode within the waveguide core. Additionally, increasing doping concentration can increase the absorption loss of the waveguide, which further reduces the confinement factor. But in the case of cross slot waveguide with highly doped Si, sometimes the confinement factor decreases and then increases. It is because of the TE and TM mode coupling at the particular height. Mode coupling occurs when energy from one mode is

transferred to another mode, leading to changes in the propagation characteristics of both modes.

4.4. Possible Fabrication Technique

The development of new technologies has led to the ability to manufacture complex structures using complementary metal-oxide-semiconductor (CMOS) processes. In this article, we will describe the step-by-step process of fabricating a structure using recent CMOS innovations [37], [42], [48]–[50].

The fabrication process begins with the growth of a Si layer on a silicon dioxide (SiO_2) layer. The SiO_2 layer is an excellent electrical insulator and can also act as a masking layer during fabrication. To create this layer, a SiO_2 layer is first grown on a pure silicon wafer using a thermal oxidation process. This process involves exposing the wafer to high temperatures, which causes oxygen to react with the silicon, resulting in the formation of a thin layer of SiO_2.

Next, a silicon layer is deposited over the SiO_2 layer using a chemical vapor deposition (CVD) process. This process involves the deposition of silicon atoms onto the SiO_2 layer at high temperatures. The deposited silicon layer is then smoothed to the desired thickness using a chemical mechanical polishing (CMP) technique. This technique involves using a polishing pad to remove excess silicon until the desired thickness is achieved.

Once the silicon layer has been smoothed, a vertical slot can be created on the SiO_2 layer using ultraviolet (UV) lithography and dry etching techniques. UV lithography involves the use of a patterned mask to transfer a desired pattern onto the SiO_2 layer. This pattern is then transferred to the underlying silicon layer using a dry etching process. The resulting structure is a vertical slot that exposes the underlying SiO_2 layer.

The next step in the fabrication process is the growth of a silver layer on the exposed SiO_2 layer. To do this, excess silicon must be removed before thin silver films are developed. Silver films are developed using an electron beam evaporation process. In this process, the evaporation chamber pressure is maintained at a very low set point, and the evaporation rate must be carefully controlled to achieve the desired thickness. The resulting silver layer is then cleaned using acid baths, water flushes, and high-pressure gas drying to remove any excess silicon and silver particles.

In summary, the fabrication process of a complex structure using recent CMOS innovations involves several key steps. First, a SiO_2 layer is grown on a pure silicon wafer using thermal oxidation. Next, a silicon layer is deposited over the SiO_2 layer using a CVD process and smoothed to the desired thickness using CMP. A vertical slot is then created on the SiO_2 layer using UV lithography and dry etching techniques. Finally, a silver layer is grown on the exposed SiO_2 layer using an electron beam evaporation process and cleaned using acid baths, water flushes, and high-pressure gas drying. By following these steps, a complex structure can be fabricated with high precision and accuracy using recent CMOS innovations.

Chapter 5

SLOT WAVEGUIDE WITH SILVER NANOPARTICLES

The surface-enhanced Raman scattering (SERS) is a powerful analytical method discovered in 1974 that has been widely acknowledged for its high sensitivity and single-molecule detection ability. The enhanced Raman signals are primarily attributed to the electromagnetic (EM) and chemical mechanisms [51]. However, recent comprehensive studies have revealed that the excitation of the localized surface plasmon resonance on the metal surface regulates the enhancement of the local EM field, which is the major contributor to the SERS effect [52], [53]. Additionally, the SERS intensity is highly sensitive to various factors such as surface structure, particle shape, size, composition, spatial arrangement, and dielectric environment [54], [55]. To overcome these challenges, researchers have focused on developing high-density and homogeneous SERS substrates, which have proven to be a challenging task.

Currently, silicon photonics has emerged as a critical consideration in the development of SERS substrates [56]. This technology has revolutionized the field of optoelectronics by integrating the advances of photonics with electrical technologies, leveraging the special electromagnetic structure of silicon. This has resulted in versatile, durable, and cost-effective production, dimensions, and power requirements of integrated optoelectronics silicon devices. The advances in complementary metal-oxide-semiconductor (CMOS) technology [51], [57], [58] have played a significant role in the development of silicon on chip gadgets, enabling the consolidation of electronic components and photonics, thanks to the high thermal stress capacity of silicon and the high optical damage threshold. Therefore, silicon photonics is expected to have a significant impact on the development of high-performance and cost-effective SERS substrates in the future. Research has looked into biosensors that are constructed solely from porous materials, specifically porous silicon (PSi) [59], [60], which is an appealing material for biosensing due to its extensive surface area. PSi, like other porous materials, can immobilize a considerable number of biomolecules, thereby increasing the chances of capturing target species. PSi is unique in that it is compatible with semiconductor processing and has a pore size that can be tuned widely, ranging from nanometers to microns.

5.1. Theory of Raman Scattering

The relationship between the induced electrical dipole moment of the molecule and the electrical field that generates it [61]–[63]. This dynamic and time-dependent electric field is defined by **E**, which is also a monochromatic plane wave of frequency ω. The total time-dependent induced electric dipole moment vector of a molecule can be written as the summation of time-dependent induced electric dipole moment vectors $p^{(1)}, p^{(2)}, p^{(3)}$ ... as follows:

$$p = p^{(1)} + p^{(2)} + p^{(3)} + \cdots \tag{5.1}$$

where, $p^{(1)} \gg p^{(2)} \gg p^{(3)} \gg \cdots$ is a fast-converging sequence. The relationship between $\boldsymbol{p}^{(1)}$ and $\boldsymbol{E}$ has the form of

$$p^{(1)} = \alpha . E \tag{5.2}$$

where, $\boldsymbol{\alpha}$ is the polarizability tensor. For $\boldsymbol{p}^{(1)}$ there may be three frequency components, one associated with Rayleigh scattering with frequency ω, and two associated with Raman scattering at frequencies $\omega \pm \omega_M$, where ω_M is a molecular frequency. Thus, we may write in component form for Raman scattering,

$$p(\omega \pm \omega_M) = \alpha E(\omega) \tag{5.3}$$

Another point of interest is the Local Field Intensity Enhancement Factor (LFIEF) [14] at the surface (i.e., by how much the intensity of the electromagnetic field is changed with respect to the intensity). The local field intensity at a specific point is proportional to the square of the electric field amplitude at that point: $|\boldsymbol{E}(r)|^2$) The LFIEF at a specific point is the normalized value of $|\boldsymbol{E}(r)|^2$ with respect to the intensity of the incoming field at that point: $|\mathbf{E}_0(r)|^2$. Explicitly,

$$LFIEF(r, \omega) = \frac{|E(r,\omega)|^2}{|E_0(r,\omega)|^2} \tag{5.4}$$

The Raman process takes advantage from both the emission and excitation enhancements, and this leads to an enhancement factor EF for SERS of the form:

$$EF \sim LFIEF^2(r, \omega) = \frac{|E(r,\omega)|^4}{|E_0(r,\omega)|^4} \tag{5.5}$$

This is called $|E|^4$ approximation for the SERS enhancement. Despite its many approximations and simplifications, it provides a very useful estimate of the real experimental SERS

improvements in a single molecule located at r. It is often used as a standard merit Fig. to test and compare theoretical models with experiments.

5.2.   Structure of the Proposed Sensor

The structure of the proposed Ag nanoparticle waveguide [64] is shown in Fig. 5.1. The high index silicon structure is surrounded by nano-silver balls. The entire system stands on a SiO_2 foundation. As the simulation will be performed for a wide range of light wavelengths, the refractive index must be a variable of wavelength. The interpolation method that uses wavelength as x parameter and linear and homogeneous refractive index as y parameter is used to achieve this goal in COMSOL. The x parameter is set from 200nm to 2000nm. The refractive index for Ag is taken from Rakić et al. [65], Green [66] and Malitson [67] provided the data needed for Si and SiO_2 respectively. The refractive index of the surrounding air medium is taken 1.00 for the entire simulation. The input electric field E_0 is set to $1\ V/m$.
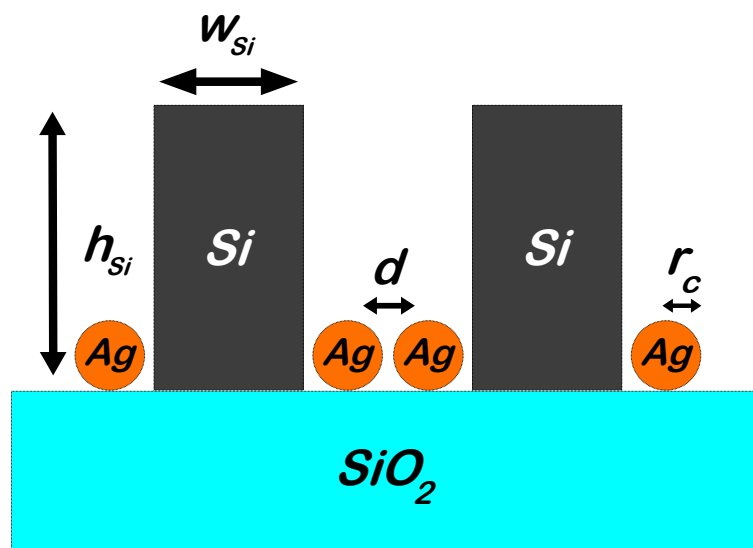
Figure 5.1: Slot waveguide with Ag nanoparticles

5.3.   Results and Analysis

In this section, the variation of Enhancement Factor (EF) for different radius of silver nanoparticle is carried out. The outcome is shown in Fig. 5.2. In Fig. r_c is appeared in the x axis, where at this point, the change in EF is plotted against the change in wavelength which plays the major role in the actual refractive index of all materials. It is quite easily observable that for the first data set of 32 nm radius, 150 nm width, 175 nm height and 2 nm separation

distance, the EF value rises fast after $1600\ nm$. For the second data set of $36\ nm$ radius, $200\ nm$ width, $225\ nm$ height and $3\ nm$, the EF curve rises a little only after $1800\ nm$. But for the last set, the magenta line is almost flat near zero. Raman scattering enhancement factor increases with wavelength is that at longer wavelengths, the light penetrates deeper into the sample, which allows for more interactions between the incident light and the sample molecules. This increased interaction results in more efficient excitation of the Raman active modes, which leads to a higher Raman scattering signal.

In Fig. 5.2 EF appears as y axis variable. Slot width, height, distance between two nanoparticles and wavelength are put as legend. It can be observed that for Si width of $150\ nm$, height of $175\ nm$, separation distance of $2\ nm$ and a wavelength of $1000\ nm$, the EF decreases almost linearly from 8.0×10^9 to 4.5×10^9. For the values of $200\ nm$, $225\ nm$, $3\ nm$ and $1550\ nm$ of Si width, height, separation, and wavelength, the EF remains almost the same which is 3.4×10^9. But when the legend values are increased more, the EF rises fast from 3.5×10^9 to 6.0×10^9. The Raman scattering enhancement factor can be significantly influenced by the size of the metal particles, with smaller particles typically providing higher enhancement factors due to their larger surface area-to-volume ratio and stronger localized electric fields. However, there is an optimal size range for metal particles and going beyond this range can result in a decrease in the Raman scattering enhancement factor. This is because the plasmon resonance frequency shifts to the ultraviolet region for particles that are too small, resulting in a decrease in the field enhancement factor in the visible region where Raman scattering occurs.
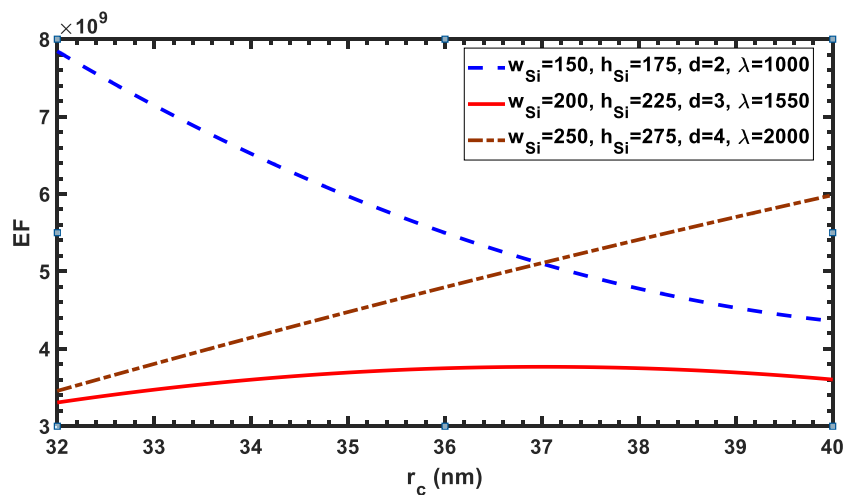
Figure 5.2: Variation of $\mathbf{EF}$ with $\mathbf{r_c}$

Variation of enhancement factor with various width is shown in Fig. 5.3. The radius is taken as $32\ nm$, $36\ nm$ and $40\ nm$. Height is varied from $175\ nm$ to $275\ n$m with a $50\ nm$ step. Separation distance is moved from $2\ nm$ to $4\ nm$, and the wavelength is chosen between $1000\ nm$ and $2000\ nm$. For $r_c = 32\ nm$, $h_{Si} = 175\ nm$, $d = 2\ nm$, $\lambda = 1000\ nm$, and the EF decreases with the increase of width. At $150\ nm$ width, the enhancement factor was 0.9×10^9. but at $250\ nm$ width, it is almost very little. This is due to the large Si width which diminishes the propagating wave faster. For $r_c = 36\ nm$, $h_{Si} = 225\ nm$, $d = 3\ nm$, $\lambda = 1550\ nm$, EF increases from 0.3×10^9 to 1.0×10^9. In this case refractive index change with wavelength plays a crucial role. It minimizes the effect of increasing Si width. In the case of $r_c = 40\ nm$, $h_{Si} = 275\ nm$, $d = 4\ nm$, $\lambda = 2000\ nm$, from a value of 4.0×10^9, EF decreases linearly up to 1.0×10^9 for a width of $195\ nm$, then it remains almost flat.

*Figure 5.3 Variation of **EF** with w_{Si}*
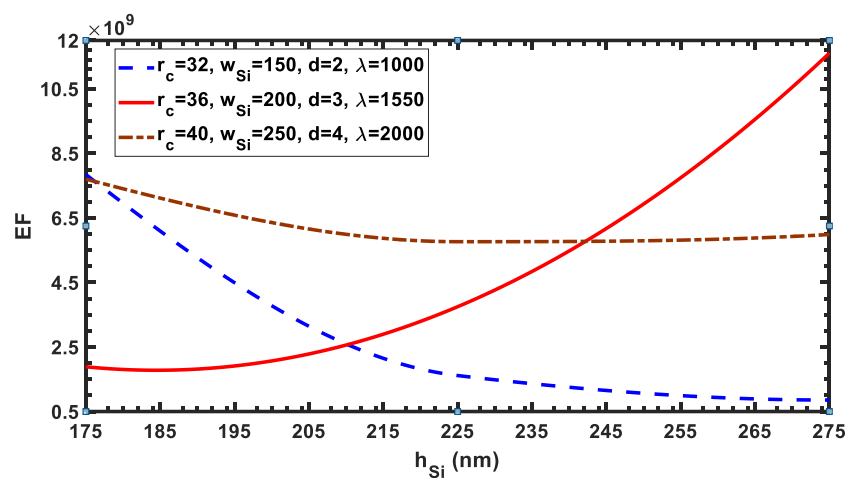
*Figure 5.4: Variation of **EF** with h_{Si}*

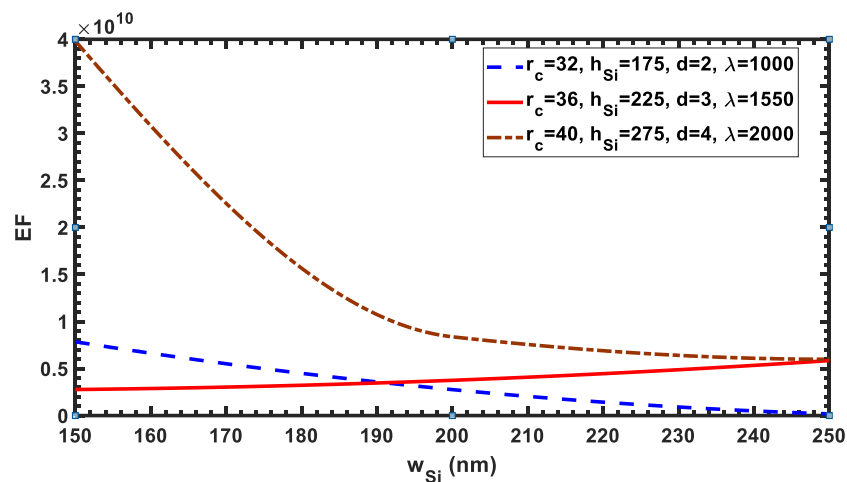With the change in Si height, the variation of enhancement factor is shown in Fig. 5.4. The radius is taken as $32\ nm$, $36\ nm$ and $40\ nm$. Width is varied with a $50\ nm$ step from $150\ nm$ to $250\ nm$. Separation distance is moved from $2\ nm$ to $4\ nm$, and the wavelength is chosen between $1000\ nm$ and $2000\ nm$. For $r_c = 32nm$, $w_{Si} = 150nm$, $d = 2nm$, $\lambda = 1000nm$, EF decreases with the increase of height. At $175\ nm$ height, the enhancement factor was 8×10^9. but at $250\ nm$ width, it is almost 1.0×10^9. This is due to the large Si height which makes slot waveguide field between Si structures. For $r_c = 36\ nm$, $w_{Si} = 200\ nm$, $d = 3\ nm$, $\lambda = 1550\ nm$, EF increases from 2×10^9 to 12.0×10^9. In this case refractive index change with wavelength plays the critical role. It neutralizes the effect of increasing Si height. In the case of $r_c = 40\ nm$, $w_{Si} = 250\ nm$, $d = 4\ nm$, $\lambda = 2000\ nm$, from a value of 8.0×10^9, EF decreases slowly to 6.5×10^9 for a width of $225\ nm$, then it remains almost same.

The height of the slot waveguide can affect the Raman scattering enhancement factor by changing the effective mode volume, which is the volume of the region where the electromagnetic field is concentrated. A smaller height can lead to a smaller mode volume and higher field enhancements, resulting in a higher Raman scattering enhancement factor. However, if the height becomes too small, the confinement of the electromagnetic field can become too strong, leading to significant absorption losses and decreased Raman scattering enhancement. The width of the slot waveguide can also influence the Raman scattering enhancement factor. A smaller width can lead to a stronger electromagnetic field concentration within the slot, resulting in higher field enhancements and a higher Raman scattering enhancement factor. However, the optimal width depends on the wavelength of the incident light and the refractive index of the materials used in the waveguide. If the width becomes too small, the waveguide may not be able to support the desired mode or may lead to significant propagation losses.

In this section, the variation of EF for different separation distance of silver nanoparticle is carried out. The result is shown in Fig. 5.5 In Fig. d is put along the x axis, where EF is shown as y axis variable. Slot width, height, radius of the nanoparticles and wavelength are put as legend. It can be observed that for the radius of $32\ nm$, height of $175\ nm$, width of $150\ nm$ and a wavelength of $1000\ nm$, the EF decreases almost linearly from 8.0×10^9 to almost zero. For the values of $36\ nm$, $200\ nm$, $225\ nm$ and $1550\ nm$ of radius, Si width, height, and wavelength, the EF changes almost the same as the previous from 9.0×10^9 to 1.0×10^9. But when the legend values are changed to $r_c = 40\ nm$, $w_{Si} = 250nm$, $h_{Si} = 275nm$, $\lambda =$

2000 nm, the EF falls fast from 2.0×10^{10} to 8.0×10^{9}. When the molecules are separated by a distance that is smaller than the wavelength of the incident light, the near-field interactions between the molecules become important. In this case, the Raman scattering enhancement factor can be significantly influenced by the distance between the molecules. When the distance between the molecules is small, the near-field interactions can lead to an enhancement of the Raman scattering signal. However, as the distance between the molecules increases, the near-field interactions become weaker, and the Raman scattering enhancement factor decreases.
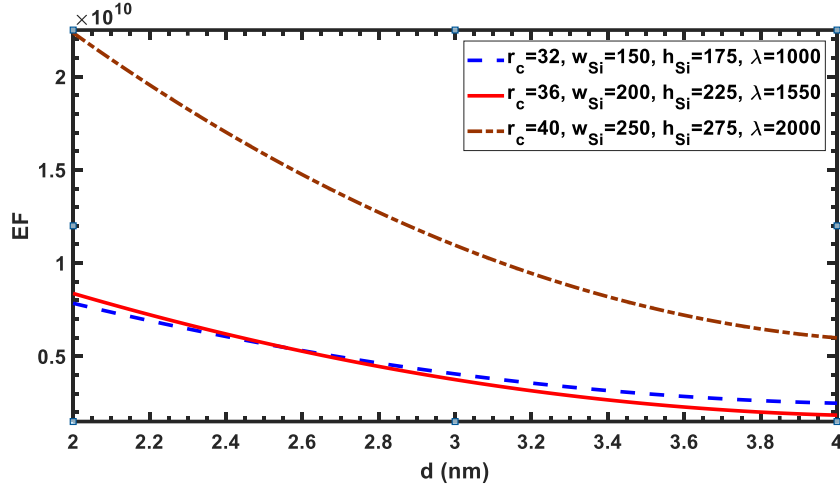
*Figure 5.5: Variation of **EF** with **d***
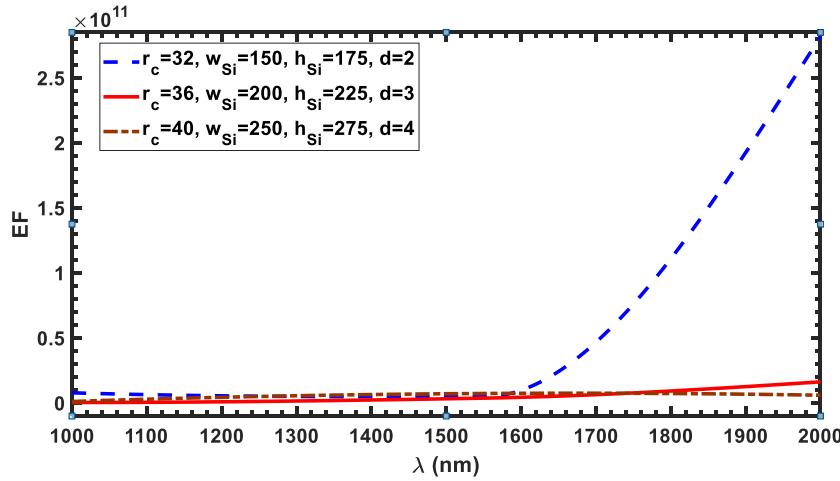
*Figure 5.6: Variation of **EF** with **λ***

At this point, the change in EF is plotted against the change in wavelength which plays the major role in the actual refractive index of all materials. The graph is shown in Fig. 5.6 it is quite easily observable that for the first data set of $32\ nm$ radius, $150\ nm$ width, $175\ nm$ height and $2\ nm$ separation distance, the EF value rises fast after $1600\ nm$. For the second

data set of 36 *nm* radius, 200 *nm* width, 225 *nm* height and 3 *nm* separation distance, the *EF* curve rises a little only after 1800 *nm*. But for the last set, the magenta line is almost flat near zero. Raman scattering enhancement factor increases with wavelength is that at longer wavelengths, the light penetrates deeper into the sample, which allows for more interactions between the incident light and the sample molecules. This increased interaction results in more efficient excitation of the Raman active modes, which leads to a higher Raman scattering signal.
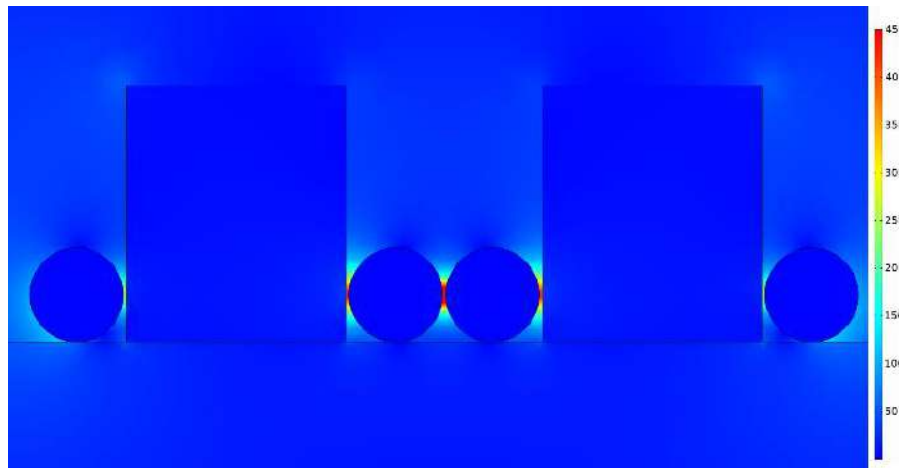
Figure 5.7: E-field surface plot
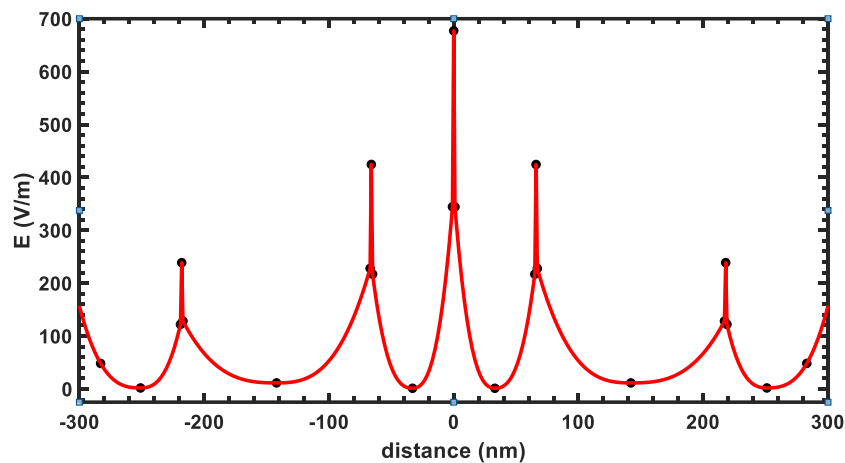
Figure 5.8: Field variation along horizontal distance

The electric field distribution is shown in Fig. 5.7 and 5.8 it is easily observable from the first Fig. that there is a high electric field in the region between the slots. There is an absence of field inside silver nanoparticles. This is due to the high attenuation factor of silver. There is an enhancement of field between the silicon and silver nanoparticles around both sides of silicon slots. Electric field at the centre is the highest seen from the second Fig. which is around

$700\ V/m$. It gradually decreases to zero inside the middle of Ag nano particles. However, it rises back to nearly 60% of the peak value again. There is a strong rise in electric fields at the far ends of the slot.
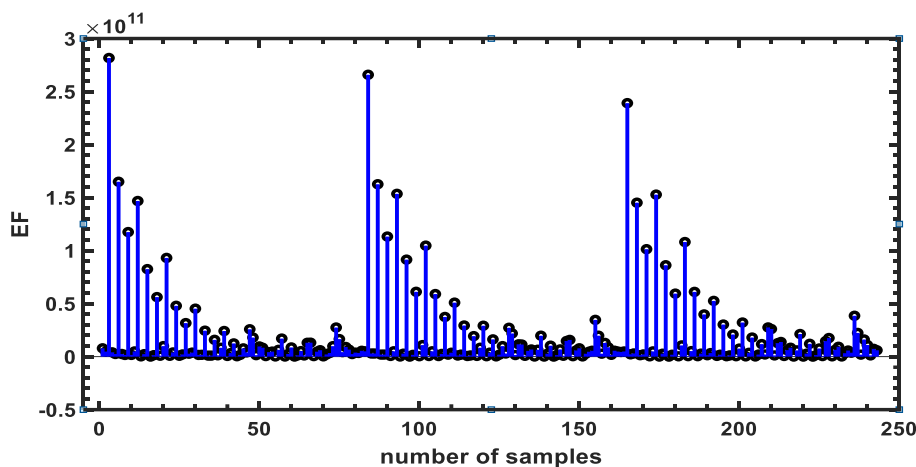
*Figure 5.9: Variation of **EF***

An approach must be pursued with the intention of making the design enhancement factor as large as possible to make it appropriate for the detection of biochemicals and other substances. It is a huge mathematical challenge to optimize all parameters with high precision. A very simple approach is taken to solve this. It is shown in Fig. 5.9, where the enhancement factor against the total number of data points is plotted. From 0 to 80 enhancement factor steadily decreases from 2.8×10^{11} to 1.3×10^{9}. It rises again close to 2.8×10^{11} in the vicinity of 85 and falls down to a negligible value at 167. The same window appears again in the 170 to 245 range. This data variance can be used as an optimization parameter. The data set can be divided into three primary data sets depending on the characteristics of the data sample variance. The maximum value of the enhancement factor is estimated in MATLAB for all data sets along with all the respective occurrences. Then all the peak points are grouped together to figure out the final result. The highest of the peak values is found with the index of 3. Putting all of the optimization parameters together with the obtained index, respective values are found. Radius of the nanoparticles is found to be $32\ nm$. Silicon height and width are $175\ nm$ and $150\ nm$ are calculated respectively. Separation distance of $2\ nm$ and $2000\ nm$ of wavelength is the outcome of the final optimization.

5.4.   Possible Fabrication Technique

The entire structure can be fabricated using recent CMOS technologies. The Si layer on the silicon-di-oxide layer is formed at the initial stage. Silicon-oxide layer is a high-quality electrically protective layer that serves as a dielectric medium in a variety of gadgets and can also be a critical masking layer in a variety of ways during manufacturing. To achieve this, the first SiO$_2$ layer is produced for pure silicon wafers using thermal oxidation [14]. After that stage, the silicon layer is stored using the chemical vapor deposition process. In this process, silicon is processed at a high temperature. Next, the silicon layer is smoothed to the appropriate size by a chemical mechanical polishing technique. After that, the vertical slot on the SiO_2 layer can be rendered using ultraviolet lithography and dry etching strategies. Colloidal Ag is prepared by an aqueous reduction of silver nitrate with trisodium citrate using the method of Lee and Meisel [68], [69]. 1ml of 0.1M $AgNO_3$ is added to 99ml of water and rapidly heated to boiling under vigorous stirring. Subsequently, 1% (w/v) trisodium citrate solution is applied to the solution and the solution is kept boiling and cooled by continuous stirring. The prepared Ag solution is first washed and then centrifuged. The remaining substrate is dispersed under sounding and dropped on the SiO_2/Si with a natural drying process [70].

Chapter 6

CONCLUSIONS

6.1. Summary of the work

The purpose of this research was to develop and enhance a metal-assisted biochemical sensor using nano-slots in silicon-on-insulator waveguide. To achieve this, three different types of sensors were explored, namely a metal-assisted cross slot waveguide, a cross slot waveguide with a highly doped silicon barrier, and a slot waveguide with silver nanoparticles. These designs were based on previous research on slot waveguides.

In the case of the metal-assisted cross slot waveguide, the dimensions of the metallic barrier and silicon were varied for both the TE and TM modes, as well as the height and refractive index. The results were then analyzed to determine the confinement factor that would make the design polarization-independent for all refractive index variations. The polarization-independent confinement factor was found to be approximately 60%, which is higher than the conventional cross slot waveguide that has a confinement factor of around 39.5%. The optimized dimensions for this arrangement were found to be Ag width = 340 nm, Si width = 153 nm, and height = 257 nm.

In the second case, the metal silver used in the previous metal-assisted cross slot waveguide was replaced with highly doped p-type silicon. The reason for this change is that highly doped silicon exhibits properties similar to those of metal. During this simulation, the width and p-type concentration of the doped silicon, the width of the silicon, the height of the waveguide were varied for both TE and TM modes, and several refractive indexes. The optimized confinement factor for this design was found to be approximately 51%, which is comparatively lower than the previous metal-assisted cross slot waveguide. The dimensions for this arrangement were optimized with a doped silicon width of 210 nm, silicon width of 180 nm, and height of 220 nm, and the doping concentration was found to be $1.44 \times 10^{22} \ cm^{-3}$.

In the last case, a different approach was taken to design the sensor, where a simple slot waveguide structure was surrounded by silver nanoparticles, and the electric field enhancement factor was calculated instead of the confinement factor. This was achieved through Raman

scattering by the silver nanoparticles. Compared to the other two designs, this approach generated a much higher electric field, with an average electric field of around 350 V/m, while the first case only had an electric field of 30 V/m. Optimization led to the identification of values such as a nanoparticle radius of 32 nm, silicon height of 175 nm, width of 150 nm, a separation distance of 2 nm, and a wavelength of 2000 nm that resulted in the highest peak values at an index of 3 with an enhancement factor of 2.87×10^{11}.

Out of the three different designs that were investigated, the metal assisted cross slot waveguide and the slot waveguide with silver nanoparticles produced the best results for biosensing applications. The metal assisted cross slot waveguide was able to maximize the confinement factor with polarization independence, which is highly desirable for biosensing due to its sensitivity and ability to detect changes in the refractive index of the surrounding medium. Furthermore, this design does not require any sample labeling or modification, making it a practical option for many biosensing applications. In contrast, the design that employed Raman scattering was found to be suitable for biosensing applications where samples need to be analyzed in their natural state without any modifications. This includes the analysis of live cells or tissues, disease diagnosis, drug discovery, and environmental monitoring. Overall, both designs have their unique advantages and could be used for different biosensing applications depending on the requirements of the experiment.

6.2.   Suggestions for Future Research

Silicon photonic components have revolutionized the field of electronics, enabling the development of faster and more efficient communication systems. However, to design optimal discrete silicon photonic components, different silicon thicknesses are required. While the leading open-access foundries have adopted a 220 nm thick device layer as the standard for circuit development, recent reviews suggest that a thicker device layer may be a better trade-off point for certain passive and active components. It should be taken into account the availability of super-flat SOI wafers with precise thickness control and the more advanced immersion lithography techniques. These factors will influence engineering decisions and help to ensure that the silicon photonic components can achieve the required performance. In the longer term, co-integration of several waveguide structures with different silicon thicknesses and operating polarizations may become necessary to achieve the required circuit performance.

This will require careful consideration of the design, fabrication, and testing of these components to ensure that they can be integrated seamlessly into the overall system.

One area that warrants further investigation is the connection of waveguides to carbon nanotube-based components. This is an exciting prospect that could lead to a brighter future, as the speed of waveguides combine with the robustness of nanotubes to create an entirely new generation of components and systems. In addition to the considerations mentioned above, there are several new research ideas that could further enhance the development of discrete silicon photonic components. One area of research that shows great promise is the use of artificial intelligence (AI) and machine learning algorithms to optimize the design of these components. AI and machine learning algorithms can be trained to analyze vast amounts of data and identify the optimal designs for specific applications. This could lead to the development of highly customized and efficient silicon photonic components that are tailored to meet the specific requirements of different systems and applications.

Another area of research that could be explored is the development of new materials for photonic components silicon. While silicon has proven to be an excellent material for waveguides and other components, there may be other materials that could offer even better performance. For example, new materials could be developed that have higher refractive indices or lower loss coefficients, which would improve the efficiency of the components. Additionally, research could be conducted into the integration of silicon photonic components with other emerging technologies, such as quantum computing and neuromorphic computing. These technologies rely on highly efficient communication networks, and the integration of silicon photonic components could enable faster and more reliable data transmission.

References

[1] R. J. Bates, "Optical switching and networking handbook," p. 302, 2001.

[2] Jeff. Hecht, "City of light : the story of fiber optics," p. 340, 2004.

[3] H. H. HOPKINS and N. S. KAPANY, "A Flexible Fibrescope, using Static Scanning," *Nature*, vol. 173, no. 4392, pp. 39–41, Jan. 1954, doi: 10.1038/173039b0.

[4] V. R. Almeida, Q. Xu, C. A. Barrios, and M. Lipson, "Guiding and confining light in void nanostructure," *Opt Lett*, vol. 29, no. 11, p. 1209, Jun. 2004, doi: 10.1364/OL.29.001209.

[5] Q. Xu, V. R. Almeida, R. R. Panepucci, and M. Lipson, "Experimental demonstration of guiding and confining light in nanometer-size low-refractive-index material," *Opt Lett*, vol. 29, no. 14, p. 1626, Jul. 2004, doi: 10.1364/OL.29.001626.

[6] R. F. Oulton, V. J. Sorger, D. A. Genov, D. F. P. Pile, and X. Zhang, "A hybrid plasmonic waveguide for subwavelength confinement and long-range propagation," *Nat Photonics*, vol. 2, no. 8, pp. 496–500, Aug. 2008, doi: 10.1038/nphoton.2008.131.

[7] N.-N. Feng, J. Michel, and L. C. Kimerling, "Optical Field Concentration in Low-Index Waveguides," *IEEE J Quantum Electron*, vol. 42, no. 9, pp. 883–888, Sep. 2006, doi: 10.1109/JQE.2006.880061.

[8] R. Sun *et al.*, "Horizontal single and multiple slot waveguides: optical transmission at λ = 1550 nm," *Opt Express*, vol. 15, no. 26, p. 17967, 2007, doi: 10.1364/OE.15.017967.

[9] T. Baehr-Jones, M. Hochberg, C. Walker, and A. Scherer, "High-Q optical resonators in silicon-on-insulator-based slot waveguides," *Appl Phys Lett*, vol. 86, no. 8, p. 081101, Feb. 2005, doi: 10.1063/1.1871360.

[10] J. Schrauwen, D. Van Thourhout, and R. Baets, "Iodine enhanced focused-ion-beam etching of silicon for photonic applications," *J Appl Phys*, vol. 102, no. 10, p. 103104, Nov. 2007, doi: 10.1063/1.2815664.

[11] C. A. Barrios *et al.*, "Demonstration of slot-waveguide structures on silicon nitride / silicon oxide platform," *Opt Express*, vol. 15, no. 11, p. 6846, 2007, doi: 10.1364/OE.15.006846.

[12]   G. S. Wiederhecker *et al.*, "Field enhancement within an optical fibre with a subwavelength air core," *Nat Photonics*, vol. 1, no. 2, pp. 115–118, Feb. 2007, doi: 10.1038/nphoton.2006.81.

[13]   S. Lee, S. C. Eom, J. S. Chang, C. Huh, G. Y. Sung, and J. H. Shin, "A silicon nitride microdisk resonator with a 40-nm-thin horizontal air slot," *Opt Express*, vol. 18, no. 11, p. 11209, May 2010, doi: 10.1364/OE.18.011209.

[14]   D. Liang *et al.*, "Low-Temperature, Strong SiO2-SiO2 Covalent Wafer Bonding for III–V Compound Semiconductors-to-Silicon Photonic Integrated Circuits," *J Electron Mater*, vol. 37, no. 10, pp. 1552–1559, Oct. 2008, doi: 10.1007/s11664-008-0489-1.

[15]   J. B. Driscoll, X. Liu, S. Yasseri, I. Hsieh, J. I. Dadap, and R. M. Osgood, "Large longitudinal electric fields (E_z) in silicon nanowire waveguides," *Opt Express*, vol. 17, no. 4, p. 2797, Feb. 2009, doi: 10.1364/OE.17.002797.

[16]   F. Dell'Olio and V. M. Passaro, "Optical sensing by optimized silicon slot waveguides," *Opt Express*, vol. 15, no. 8, p. 4977, 2007, doi: 10.1364/OE.15.004977.

[17]   M. Lipson, "Guiding, modulating, and emitting light on Silicon-challenges and opportunities," *Journal of Lightwave Technology*, vol. 23, no. 12, pp. 4222–4238, Dec. 2005, doi: 10.1109/JLT.2005.858225.

[18]   A. V. Krasavin and A. V. Zayats, "Silicon-based plasmonic waveguides," *Opt Express*, vol. 18, no. 11, p. 11791, May 2010, doi: 10.1364/OE.18.011791.

[19]   F. Prieto *et al.*, "An integrated optical interferometric nanodevice based on silicon technology for biosensor applications," *Nanotechnology*, vol. 14, no. 8, pp. 907–912, Aug. 2003, doi: 10.1088/0957-4484/14/8/312.

[20]   Dan-Xia Xu *et al.*, "Silicon Photonic Integration Platform—Have We Found the Sweet Spot?," *IEEE Journal of Selected Topics in Quantum Electronics*, vol. 20, no. 4, pp. 189–205, Jul. 2014, doi: 10.1109/JSTQE.2014.2299634.

[21]   C. A. Barrios *et al.*, "Slot-waveguide biochemical sensor," *Opt Lett*, vol. 32, no. 21, p. 3080, Nov. 2007, doi: 10.1364/OL.32.003080.

[22]   C. A. Barrios *et al.*, "Label-free optical biosensing with slot-waveguides," *Opt Lett*, vol. 33, no. 7, p. 708, Apr. 2008, doi: 10.1364/OL.33.000708.

[23]   B. J. Luff, R. Wilson, D. J. Schiffrin, R. D. Harris, and J. S. Wilkinson, "Integrated-optical directional coupler biosensor," *Opt Lett*, vol. 21, no. 8, p. 618, Apr. 1996, doi: 10.1364/OL.21.000618.

[24] K. De Vos, J. Girones, S. Popelka, E. Schacht, R. Baets, and P. Bienstman, "SOI optical microring resonator with poly(ethylene glycol) polymer brush for label-free biosensor applications," *Biosens Bioelectron*, vol. 24, no. 8, pp. 2528–2533, Apr. 2009, doi: 10.1016/j.bios.2009.01.009.

[25] T. Claes, J. G. Molera, K. De Vos, E. Schacht, R. Baets, and P. Bienstman, "Label-Free Biosensing With a Slot-Waveguide-Based Ring Resonator in Silicon on Insulator," *IEEE Photonics J*, vol. 1, no. 3, pp. 197–204, Sep. 2009, doi: 10.1109/JPHOT.2009.2031596.

[26] A. Gupta, D. Akin, and R. Bashir, "Detection of bacterial cells and antibodies using surface micromachined thin silicon cantilever resonators," *Journal of Vacuum Science & Technology B: Microelectronics and Nanometer Structures*, vol. 22, no. 6, p. 2785, 2004, doi: 10.1116/1.1824047.

[27] D. F. Brailsford, "Electric field strengths and ion trajectories in sharp-edge field ionization sources," *J Phys D Appl Phys*, vol. 3, no. 2, p. 314, Feb. 1970, doi: 10.1088/0022-3727/3/2/314.

[28] D. J. Griffiths, "Introduction to electrodynamics,Griffith-3ed.pdf," *Int J Neural Syst*, vol. 3, no. 3, p. 580, 2010, Accessed: Apr. 13, 2023. [Online]. Available: http://www.ncbi.nlm.nih.gov/pubmed/20563938

[29] A. Ern and J.-L. Guermond, *Theory and Practice of Finite Elements*, vol. 159. New York, NY: Springer New York, 2004. doi: 10.1007/978-1-4757-4355-5.

[30] S. C. Brenner and R. L. Scott, "The mathematical theory of finite element methods; Texts in applied mathematics ; 15.," *Springer*, vol. 2nd, pp. xv, 361, 2002.

[31] "Computational Electromagnetics Modeling: Which Module to Use? | COMSOL Blog." https://www.comsol.com/blogs/computational-electromagnetics-modeling-which-module-to-use/ (accessed Apr. 05, 2023).

[32] F. Morichetti, A. Canciamilla, C. Ferrari, M. Torregiani, A. Melloni, and M. Martinelli, "Roughness Induced Backscattering in Optical Silicon Waveguides," *Phys Rev Lett*, vol. 104, no. 3, p. 033902, Jan. 2010, doi: 10.1103/PhysRevLett.104.033902.

[33] J. A. Dionne, L. A. Sweatlock, H. A. Atwater, and A. Polman, "Plasmon slot waveguides: Towards chip-scale propagation with subwavelength-scale localization," *Phys Rev B*, vol. 73, no. 3, p. 035407, Jan. 2006, doi: 10.1103/PhysRevB.73.035407.

[34]   B. Rahman and J. Davies, "Finite-element solution of integrated optical waveguides," *Journal of Lightwave Technology*, vol. 2, no. 5, pp. 682–688, 1984, doi: 10.1109/JLT.1984.1073669.

[35]   K. Saitoh and M. Koshiba, "Full-vectorial imaginary-distance beam propagation method based on a finite element scheme: application to photonic crystal fibers," *IEEE J Quantum Electron*, vol. 38, no. 7, pp. 927–933, Jul. 2002, doi: 10.1109/JQE.2002.1017609.

[36]   Y. Ishizaka, Y. Kawaguchi, K. Saitoh, and M. Koshiba, "Three-Dimensional Finite-Element Solutions for Crossing Slot-Waveguides With Finite Core-Height," *Journal of Lightwave Technology*, vol. 30, no. 21, pp. 3394–3400, Nov. 2012, doi: 10.1109/JLT.2012.2217478.

[37]   M. Nagai, Y. Ishizaka, K. Saitoh, and M. Koshiba, "Propagation length and coupling characteristics of a hybrid plasmonic waveguide with a uniform silica layer," in *2013 Conference on Lasers and Electro-Optics Pacific Rim (CLEOPR)*, IEEE, Jun. 2013, pp. 1–2. doi: 10.1109/CLEOPR.2013.6600401.

[38]   S. Makino, T. Sato, Y. Ishizaka, T. Fujisawa, and K. Saitoh, "Three-Dimensional Finite-Element Time-Domain Beam Propagation Method and Its Application to 1-D Photonic Crystal-Coupled Resonator Optical Waveguide," *Journal of Lightwave Technology*, vol. 33, no. 18, pp. 3836–3842, Sep. 2015, doi: 10.1109/JLT.2015.2446514.

[39]   M. A. Sefunc, M. Pollnau, and S. M. García-Blanco, "Low-loss sharp bends in polymer waveguides enabled by the introduction of a thin metal layer," *Opt Express*, vol. 21, no. 24, p. 29808, Dec. 2013, doi: 10.1364/OE.21.029808.

[40]   Y. Ishizaka, S. Makino, T. Fujisawa, and K. Saitoh, "A Metal-Assisted Silicon Slot Waveguide for Highly Sensitive Gas Detection," *IEEE Photonics J*, vol. 9, no. 1, pp. 1–9, Feb. 2017, doi: 10.1109/JPHOT.2016.2630308.

[41]   C. Pan and B. M. A. Rahman, "High-Sensitivity Polarization-Independent Biochemical Sensor Based on Silicon-on-Insulator Cross-Slot Waveguide," *IEEE Journal of Selected Topics in Quantum Electronics*, vol. 23, no. 2, pp. 64–71, Mar. 2017, doi: 10.1109/JSTQE.2016.2594094.

[42]   T. Dar, J. Homola, B. M. A. Rahman, and M. Rajarajan, "Label-free slot-waveguide biosensor for the detection of DNA hybridization," *Appl Opt*, vol. 51, no. 34, p. 8195, Dec. 2012, doi: 10.1364/AO.51.008195.

[43]   V. P. Tzolov and M. Fontaine, "A passive polarization converter free of longitudinally-periodic structure," *Opt Commun*, vol. 127, no. 1–3, pp. 7–13, Jun. 1996, doi: 10.1016/0030-4018(96)00039-9.

[44]   M. Soma *et al.*, "Optimum waveguide-core size for reducing device property distribution of Si-wire waveguide devices," *Jpn J Appl Phys*, vol. 54, no. 4S, p. 04DG03, Apr. 2015, doi: 10.7567/JJAP.54.04DG03.

[45]   H. Subbaraman *et al.*, "Recent advances in silicon-based passive and active optical interconnects," *Opt Express*, vol. 23, no. 3, p. 2487, Feb. 2015, doi: 10.1364/OE.23.002487.

[46]   S. Balslev *et al.*, "Lab-on-a-chip with integrated optical transducers," *Lab Chip*, vol. 6, no. 2, pp. 213–217, 2006, doi: 10.1039/B512546D.

[47]   Q. Liu, J. S. Kee, and M. K. Park, "A refractive index sensor design based on grating-assisted coupling between a strip waveguide and a slot waveguide," *Opt Express*, vol. 21, no. 5, p. 5897, Mar. 2013, doi: 10.1364/OE.21.005897.

[48]   C. Viphavakit, M. Komodromos, C. Themistos, W. S. Mohammed, K. Kalli, and B. M. Azizur Rahman, "Optimization of a horizontal slot waveguide biosensor to detect DNA hybridization," *Appl Opt*, vol. 54, no. 15, p. 4881, May 2015, doi: 10.1364/AO.54.004881.

[49]   X. Zhang, C. R. Yonzon, M. A. Young, D. A. Stuart, and R. P. Van Duyne, "Surface-enhanced Raman spectroscopy biosensors: excitation spectroscopy for optimisation of substrates fabricated by nanosphere lithography," *IEE Proc Nanobiotechnol*, vol. 152, no. 6, p. 195, 2005, doi: 10.1049/ip-nbt:20050009.

[50]   J. Chee, S. Zhu, and G. Q. Lo, "CMOS compatible polarization splitter using hybrid plasmonic waveguide," *Opt Express*, vol. 20, no. 23, p. 25345, Nov. 2012, doi: 10.1364/OE.20.025345.

[51]   H. Xu, J. Aizpurua, M. Käll, and P. Apell, "Electromagnetic contributions to single-molecule sensitivity in surface-enhanced Raman scattering," *Phys Rev E*, vol. 62, no. 3, pp. 4318–4324, Sep. 2000, doi: 10.1103/PhysRevE.62.4318.

[52]   J. Prinz, C. Heck, L. Ellerik, V. Merk, and I. Bald, "DNA origami based Au–Ag-core–shell nanoparticle dimers with single-molecule SERS sensitivity," *Nanoscale*, vol. 8, no. 10, pp. 5612–5620, 2016, doi: 10.1039/C5NR08674D.

[53]   J.-A. Huang *et al.*, "SERS discrimination of single DNA bases in single oligonucleotides by electro-plasmonic trapping," *Nat Commun*, vol. 10, no. 1, p. 5321, Nov. 2019, doi: 10.1038/s41467-019-13242-x.

[54]   F. Le *et al.*, "Metallic Nanoparticle Arrays: A Common Substrate for Both Surface-Enhanced Raman Scattering and Surface-Enhanced Infrared Absorption," *ACS Nano*, vol. 2, no. 4, pp. 707–718, Apr. 2008, doi: 10.1021/nn800047e.

[55]   S. Simoncelli *et al.*, "Quantitative Single-Molecule Surface-Enhanced Raman Scattering by Optothermal Tuning of DNA Origami-Assembled Plasmonic Nanoantennas," *ACS Nano*, vol. 10, no. 11, pp. 9809–9815, Nov. 2016, doi: 10.1021/acsnano.6b05276.

[56]   S. Schlücker, Ed., *Surface Enhanced Raman Spectroscopy*. Wiley, 2010. doi: 10.1002/9783527632756.

[57]   J.-F. Li *et al.*, "Extraordinary Enhancement of Raman Scattering from Pyridine on Single Crystal Au and Pt Electrodes by Shell-Isolated Au Nanoparticles," *J Am Chem Soc*, vol. 133, no. 40, pp. 15922–15925, Oct. 2011, doi: 10.1021/ja2074533.

[58]   J. Quan, Y. Zhu, J. Zhang, J. Li, and N. Wang, "High-performance surface-enhanced Raman scattering substrate prepared by self-assembling of silver nanoparticles into the nanogaps of silver nanoislands," *Appl Opt*, vol. 56, no. 20, p. 5751, Jul. 2017, doi: 10.1364/AO.56.005751.

[59]   Y. Li, H. Zhao, A. Raza, S. Clemmen, and R. Baets, "Surface-Enhanced Raman Spectroscopy Based on Plasmonic Slot Waveguides With Free-Space Oblique Illumination," *IEEE J Quantum Electron*, vol. 56, no. 1, pp. 1–8, Feb. 2020, doi: 10.1109/JQE.2019.2946839.

[60]   G. Rong, A. Najmaie, J. E. Sipe, and S. M. Weiss, "Nanoscale porous silicon waveguide for label-free DNA sensing," *Biosens Bioelectron*, vol. 23, no. 10, pp. 1572–1576, May 2008, doi: 10.1016/j.bios.2008.01.017.

[61]   D. A. Long, *The Raman Effect*. Wiley, 2002. doi: 10.1002/0470845767.

[62]   K. G. E, "Der Smekal-Raman-Effekt," *Nature*, vol. 128, no. 3242, pp. 1026–1026, Dec. 1931, doi: 10.1038/1281026c0.

[63]   C. V. RAMAN and K. S. KRISHNAN, "The Negative Absorption of Radiation," *Nature*, vol. 122, no. 3062, pp. 12–13, Jul. 1928, doi: 10.1038/122012b0.

[64]   M. Fleischmann, P. J. Hendra, and A. J. McQuillan, "Raman spectra of pyridine adsorbed at a silver electrode," *Chem Phys Lett*, vol. 26, no. 2, pp. 163–166, May 1974, doi: 10.1016/0009-2614(74)85388-1.

[65]   A. D. Rakić, A. B. Djurišić, J. M. Elazar, and M. L. Majewski, "Optical properties of metallic films for vertical-cavity optoelectronic devices," *Appl Opt*, vol. 37, no. 22, p. 5271, Aug. 1998, doi: 10.1364/AO.37.005271.

[66]   M. A. Green, "Self-consistent optical parameters of intrinsic silicon at 300K including temperature coefficients," *Solar Energy Materials and Solar Cells*, vol. 92, no. 11, pp. 1305–1310, Nov. 2008, doi: 10.1016/j.solmat.2008.06.009.

[67]   I. H. Malitson, "Interspecimen Comparison of the Refractive Index of Fused Silica*,†," *J Opt Soc Am*, vol. 55, no. 10, p. 1205, Oct. 1965, doi: 10.1364/JOSA.55.001205.

[68]   P. C. Lee and D. Meisel, "Adsorption and surface-enhanced Raman of dyes on silver and gold sols," *J Phys Chem*, vol. 86, no. 17, pp. 3391–3395, Aug. 1982, doi: 10.1021/j100214a025.

[69]   S. Lee, S. C. Eom, J. S. Chang, C. Huh, G. Y. Sung, and J. H. Shin, "Label-free optical biosensing using a horizontal air-slot SiN_x microdisk resonator," *Opt Express*, vol. 18, no. 20, p. 20638, Sep. 2010, doi: 10.1364/OE.18.020638.

[70]   T. Qiu, W. Zhang, X. Lang, Y. Zhou, T. Cui, and P. K. Chu, "Controlled Assembly of Highly Raman-Enhancing Silver Nanocap Arrays Templated by Porous Anodic Alumina Membranes," *Small*, vol. 5, no. 20, pp. 2333–2337, Oct. 2009, doi: 10.1002/smll.200900577.